CHARACTERIZATION OF MODIFIED ITO ANODE SURFACES WITH 4-[(3-METHYLPHENYL)(PHENYL) AMINO]BENZOIC ACID FOR OLED APPLICATIONS

A Thesis submitted to
the Graduate School of Engineering and Sciences of
İzmir Institute of Technology
in Partial Fulfillment of the Requirements for the Degree of

MASTER OF SCIENCE

in Physics

by

Nesli YAĞMURCUKARDEŞ

July 2011
İZMİR

We approve the thesis of **Nesli YAĞMURCUKARDEŞ**

_____

Assoc. Prof. Dr. Salih OKUR
Supervisor

_____

Assist. Prof. Dr. Şerafettin DEMİÇ
Committee Member

_____

Assoc. Prof. Dr. Mehmet Salih DİNLEYİCİ
Committee Member

6 July 2011

_____

Prof. Dr. Nejat BULUT
Head of the Department of Physics

_____

Prof. Dr. Durmuş Ali DEMİR
Dean of the Graduate School of
Engineering and Sciences

ACKNOWLEDGEMENTS

Firstly, I would like to thank my supervisor, Dr. Salih OKUR for his encouragement and support during my master thesis education. I also would like to thank Dr. Şerafettin DEMİÇ and his coworkers for their contribution to this thesis.

I am also thankful to all my friends in İYTE but especially Atike İNCE and Hale SERT as they made department of physics a wonderful working environment for me.

Moreover, my special thanks go to my lab friends Hasan AYDIN, Ali Kemal HAVARE and Mavişe ŞEKER because of their friendship and support whenever I need.

Mehmet YAĞMURCUKARDEŞ, my husband is another person I would like to thank while we overcome all difficulties together.

Last but not least, I want to thank to my family; my father, Memiş TEKGÜZEL, my mother, Nesil TEKGÜZEL as they have always supported and encouraged me…

This research was supported by TUBITAK with 108T718 project number.

ABSTRACT

CHARACTERIZATION OF MODIFIED ITO ANODE SURFACES WITH 4-[(3-METHYLPHENYL)(PHENYL)AMINO]BENZOIC ACID FOR OLED APPLICATIONS

This thesis focuses on to improve OLED characteristics of fabricated devices by modifying the ITO (anode) surface using novel carboxylic acid based molecule 4-[(3-methylphenyl)(phenyl)amino]benzoic acid (MPPBA). In this study, commercial ITO substrates were used as anodes. To modify the ITO surface, etched ITO substrates were kept in 1mM MPPBA-ethanol solution. As a hole transport layer (HTL), N,N′-bis(3-methylphenyl)-N,N′-diphenylbenzidine (TPD) or N,N′-Di-[(1-naphthyl)-N,N′-diphenyl]-1,1′-biphenyl)-4,4′-diamine (NPB) small molecules were deposited using an organic evaporator system under the vacuum of 10^{-6} Torr. Finally, as a cathode contact layer, aluminum thin film of 120 nm was deposited on top of the fabricated organic thin film layers. The final structure of the devices was obtained as ITO /SAM (2nm) /HTL (50nm) /Al (120nm). The current-voltage characteristics of devices of unmodified bare ITO and MPPBA modified ITO substrates were analyzed by using the space charge limited current approach and Thermionic Schottky Emission Models. Additionally, surface characterizations of the SAM modified thin films were carried out using Quartz Crystal Microbalance (QCM), Atomic Force Microscopy (AFM), Kelvin Probe Force Microscopy (KPFM), X-ray Photoelectron Spectroscopy (XPS), Cyclic Voltammetry (CV) and Ultraviolet-visible Absorption Spectroscopy (UV-Vis) techniques. The obtained results reveal that the modification of the ITO surface with MPPBA molecules reduces the barrier height difference between the Fermi level of the anode and HOMO level of the HTL. Hence the hole injection increases while the turn-on voltage decreases. As a result of this process OLED characteristics were improved by using the MPPBA SAM molecules.

ÖZET

OLED UYGULAMALARINA YÖNELİK 4-[(3-METİLFENİL)(FENİL)AMİNO]BENZOİK ASİT İLE MODİFİYE EDİLMİŞ İTO ANOT YÜZEYLERİNİN KARAKTERİZASYONU

Bu tez, yeni sentezlenmiş karboksilik asit temelli kendiliğinden organize tek katman 4-[(3-metilfenil)(fenil)amino]benzoik asit (MPPBA) molekülü ile ITO yüzeyini modifiye ederek üretilen OLED ürünlerinin özelliklerini iyileştirmek üzerine odaklanmıştır. Bu çalışmada, temin edilen ITO altlıklar kısa devre oluşumunu engellemek için bir kenarlarından asitle kaldırılarak anot katmanı olarak kullanıldı. Yüzey özelliklerini değiştirmek için, ITO'lar 1mM' lık etanol çözücülü MPPBA çözeltisi içinde belli sure tutuldu. Elektron boşluğu iletim tabakası (HTL) olarak N,N′-bis(3-metilfenil)-N,N′-difenilbenzidin TPD (ya da N,N′-Di-[(1-naftil)-N,N′-difenil]-1,1′-bifenil)-4,4′-diamin NPB) küçük molekülleri organik buharlaştırma sistemi ile yüksek vakum altında modifiye edilmiş ITO üzerine kaplandı. Katot tabakası olarak da alüminyum elektrotlar metal buharlaştırma sistemi ile yine yüksek vakum altında kaplandı. Oluşturulan OLED'lerin son yapıları ITO/KOT (2nm) /HTL (50nm) /Al (120nm) şeklindedir. Yalın ve MPPBA molekülleriyle modifiye edilmiş ITO altlıklar kullanılarak üretilen OLED aletlerin akım-voltaj karakteristikleri karşılaştırmalı olarak analiz edildi. Bunlara ek olarak, Kendiliğinden Organize Tek Katman (KOT) moleküllerle modifiye edilmiş ince filmlerin yüzey karakterizasyonları Kuvars Kristalli Mikro Terazi (QCM), Atomik Kuvvet Mikroskobu (AFM), Kelvin Milli Kuvvet Mikroskobu (KPFM), X-ışını Fotoelektron Spektroskopisi (XPS), Dönüşümlü Voltametre (CV) ve Ultraviyole-görünür Bölge Işık Absorpsiyon Spektrofotometresi (UV-Vis) teknikleri kullanılarak analiz edildi. Elde edilen sonuçlar KOT molekülerinin varlığını doğrulamaktadır. ITO yüzeyinin MPPBA molekülleri ile modifiye edilmesi anot Fermi düzeyi ile elektron boşluğu iletim tabakası arasındaki bariyer yüksekliğini azaltmakta ve bu sebeple elektron boşluğu iletimini arttırırken çalışma voltajını düşürmektedir. Sonuç olarak, MPPBA KOT molekülleri kullanılarak OLED özellikleri iyileştirilmiştir.

To my Family

TABLE OF CONTENTS

LIST OF FIGURES

Figure **Page**

LIST OF TABLES

Table **Page**

CHAPTER 1

INTRODUCTION

1.1. Overview

Organic optoelectronics has been an attractive field of research for almost two decades. A novel electronic technology has been dedicated to organic electronics. Conventional polymers, small molecules, plastics are now useful materials due to low voltage operation enabling application properties for portable electronics. The discovery and the development of conducting polymers by Alan Heeger, Alan MacDiarmid and Hideki Shirakawa led to today's device applications as active and passive electronics and optoelectronics devices such as diodes, transistors, lasers, solar cells and photodiodes.

The current display technologies such as Liquid Crystal Displays (LCD) and Cathode Ray Tubes (CRTs) are underrated as OLEDs are flat panel displays with high resolution using less energy. The advantages also include good self-luminance efficiency without the use of backlight, wide viewing angle, high image content, low temperature process and promise of full color. At the moment, passive monochrome and active-matrix full color displays are commercially available.

The materials used in OLED fabrication have significant role in device performance. Therefore, studies focused on the development and the improvement of molecular materials. In addition, the charge injection and transport mechanisms have great importance on operating voltage and luminance efficiency. In order to improve the hole and electron injection, additional active thin layer was inserted. In order to understand the OLED characteristics, there are several studies and developments in this field.

In the near future, displays with various sizes, resolutions and purposes will be found in all aspects of our daily lives. Billboards will be changed to dynamic posters, flashy displays; wall paintings will be transformed to digital scenery and photographs. Displays will be produced in many different shapes, forms and actually transparent.

1.2. Research Objectives

The objectives of this thesis are to reduce the barrier of hole injection and to improve adhesion characteristic at the anode-organic film interface by the use of benzoic acid derivative compound which have the ability to form self-assembled monolayers (SAMs). SAM modified organic light-emitting devices (OLED) were fabricated in the structure of multiple layer device. The current-voltage relations and the electroluminescence of SAM modified OLEDs were characterized and compared with unmodified devices. In addition, to investigate the surface properties, Quartz Crystal Microbalance (QCM), Atomic Force Microscopy (AFM), Kelvin Probe Force Microscopy (KPFM), X-ray Photoelectron Spectroscopy (XPS), Cyclic Voltammetry (CV) and Ultraviolet-visible Spectroscopy (UV-Vis) characterization techniques were used.

1.3. Outline of Thesis

There are six chapters in this thesis. In chapter two, the nature of the OLED, device theory, material and device structure are explained. In chapter three, SAM phenomenon, history of SAM applications, formation process and characterization techniques have been discussed briefly. In chapter four, the device fabrication process is presented. The surface characterization and the electrical characterization results of the organic diodes are shown in chapter five, including its discussion. Finally, chapter six constitutes the conclusion of this study.

CHAPTER 2

ORGANIC LIGHT EMITTING DIODES

Organic light- emitting diodes (OLEDs) as a novel device technology for flat panel displays have received a great attention in the research community for the last two decades. OLEDs consist of a thin fluorescent organic film sandwiched between two electrodes (a transparent conducting anode and a metallic cathode). When external bias voltage is applied to the conductive electrodes, charge carriers get injected into the organic layer and recombination takes place in the bulk. As a result of this recombination, visible, infrared and ultra-violet radiation can be produced.

Until now, OLED displays are used in the panel of a mobile phone, digital camera, car audio, MP3 player and other portable small electronic applications. They are unconventional and operate at low voltages, of the order of 3 - 5 V. Experimentally OLEDs are already more efficient than incandescent lamps. It is expected that OLED technologies will be able to take over earlier display industries after the fabrication of flat panel displays with large scales are realized.

2.1. Advantages of OLEDs

Compared to other display technologies, OLEDs have many advantages. For example, OLEDs have low operating voltage with high brightness. White OLEDs' brightness can be up to 150,000 cd/m^2. There is no need of backlight or filters as OLEDs can emit light themselves. Therefore, OLEDs are lightweight devices with thin displays like the newest prototypes of SONY displays measuring only 0.3 mm. There is a wide range of organic materials to produce the fundamental colors (red, blue and green). OLEDs are compatible with plastic substrates paving the way for flexible color display technologies. Unlike liquid-crystal displays (LCDs), OLEDs have wide viewing angle as high as 160 degrees. In addition, electroluminescence decay time of an OLED is smaller than 1 μs.

Although OLED display technologies have many advantages, they have main disadvantage such as the degradation of the materials by oxygen and water molecules (Sugiyama, et al. 2000). As a result of this issue, operational lifetimes of OLEDs are limited. However, by encapsulation, OLEDs lifetimes are now comparable with other standard LEDs commercial products.

2.2. History of Electroluminescence and OLED Technology

Light emission occurs from an OLED device when external bias is applied (Electroluminescence (EL)). In the early 1960s, Pope et al. (Pope, et al. 1963) discovered organic electroluminescence from anthracene crystals. When high amount of bias (V) was applied to these crystals with the thickness of μm to mm, light emission occurred. As such voltages are not practical for most applications, up to 1980s therefore the experimental results were postponed. Although Vincett et al. (Vincett, et al. 1982) obtained EL from vacuum-deposited anthracene by applying voltages of only 30 V in 1982, these voltages were still not appropriate for applications.

The fundamental breakthrough was achieved in late 1980s, when C. W. Tang and S. A. Van Slyke (Tang, et al. 1987) from Eastman Kodak demonstrated highly efficient light emitting diodes by using organic small conjugated molecules as a multilayer thin film. In the basic structure of the device N,N′-bis(3-methylphenyl)-N,N′-diphenyl-4,4’ diamine (TPD) and tris(8-hydroxyquinoline) aluminum (Alq_3) small molecular weight organic materials were used as hole transport layer and electron transport layer, respectively. Under less than 10 V bias, more than 1000 cd/m^2 brightness and 1% external quantum efficiency (photons and electrons) were achieved. Also, as a result of thin film structure (overall thickness ~100 nm), operating voltage reduced and luminous efficiency increased significantly.

Later in 1990, Burroughs et al. introduced the first polymer based light emitting diodes using poly(phenylenevinylene) (PPV) (Burroughes, et al. 1990). By spin coating method, PPV thin film coated between two electrodes. When voltage was applied between these electrodes, a yellow-green light was produced. In polymer based light emitting diodes (PLED), quantum efficiency was only 0.05% as they do not have heterojunction.

In general, in small molecular OLEDs and PLEDs, light emission is produced as a result of fluorescent emission of singlet excitons. The carrier recombination can produce singlet and triplet excitons in the ratio of 1:3. Although the singlet excitons decay radiatively producing EL, triplet excitons decay non-radiatively. Therefore, maximum value of EL efficiency is limited 25% by spin statistics. M. A. Baldo et al. demonstrated that by introduction of phosphorescent dopants into OLED devices, the energy from all the triplet states could be harnessed as phosphorescent light (Baldo, et al. 1998). Therefore, the theoretical limit of molecular EL efficiency can reach up to 100%. In the recent experiments, green and red emitting phosphorescent OLEDs have nearly 100% internal quantum efficiencies and 19% external quantum efficiencies.

The power efficiencies of OLED devices in different colors have been increased and white OLEDs reach the efficiencies that are close to fluorescent lamps. It is doubtful that OLED technologies will be able to take over the other display industry in a little while.

2.3. Organic Semiconductors and Organic Light Emitting Diodes

The main difference between organic semiconductor and inorganic semiconductor is that organic semiconductors contain carbon-based molecules that interact through dipole-dipole forces. Almost all organic materials are insulators with wide bandgaps and low conductivity (Abkowitz, et al. 1968, Almeleh, et al. 1966, McGinnes, et al. 1974, Shirakawa, et al. 1977). However, in recent years, studies showed that in organic-thin film devices, charge carrier mobilities exceeding comparable values with mobilities in amorphous silicon (Haddock, et al. 2005, Kelley, et al. 2004, Nelson, et al. 1998).

Organic semiconductors can also emit light in the visible region, as they have band gaps in the range of 1.5 to 3.5 eV. They have vast potential to transform electronic devices and save energy. In organic semiconductors, processing can be done at low temperatures whereas in inorganic semiconductors high temperature is required.

To describe the chemical bonding mechanism between the atoms in organic compounds, orbitals are used. The orbitals are the wave functions, that can be defined by solving Schrödinger Equation and they describe the region where one or two electrons can be found for an atom. In carbon, there are four valence orbitals that are

responsible for the formation of covalent bonds (2s, $2p_x$, $2p_y$, $2P_z$). The hybrid orbitals are assumed to be the new orbitals that originated with the superposition of the s-p orbitals. There are three kinds of hybrid orbitals (sp^1, sp^2, sp^3 where subscripts denote the number of p-orbitals) (Haldi 2008). The illustration of the 2s-, 2p- and the hybrid orbitals are shown in Figure 2.1.

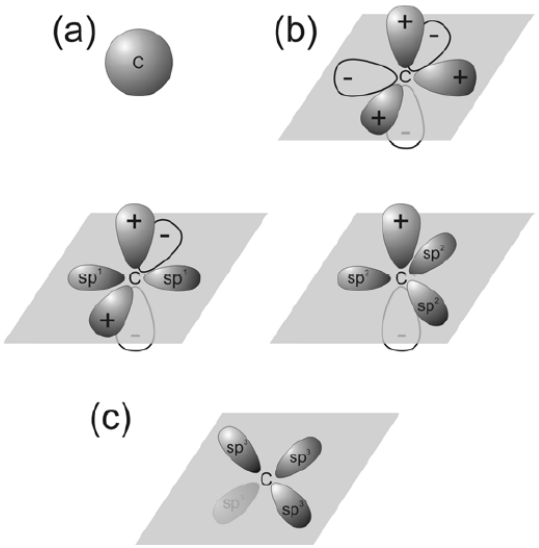

Figure 2.1. Illustration of the (a) 2s-,(b) 2p- and (c) the hybrid orbitals for a carbon atom (Source: (Oxtoby, et al. 2003)).

For the covalent single bond (σ bond) formation, the hybrid orbitals are overlapped. However the double and the triple bonds which consist of one sigma bond and one or two pi bonds, occur in systems with sp^2 or sp hybridization, respectively.

The bonding energy is smaller in π-bonds than in σ-bonds as the spatial overlap between the hybrid orbitals in σ-bonds is large, whereas the overlap of p-orbitals in π-bonds is rather small. As a result of delocalization of electrons in p-orbitals due to the weaker coupling, more polarization of electrons can be expected. In the conjugated systems, the electron delocalization can be achieved over an even longer range of distance than just two atoms since along the chain p-orbitals keep overlapping.

In a system with several atoms and electrons the Schrödinger equation becomes very complicated. Therefore, by neglecting certain terms of Hamiltonian, eigenfunctions and eigenvalues of the Hamiltonian can be approximated. The linear combination of

atomic orbitals-molecular orbitals (LCAO-MO) is one of these approximations for molecular orbitals. Since the electrons in σ-bonds are harder to remove than electrons in π-bonds, their contributions can be neglected (Pope, et al. 1999). Therefore, only π-molecular orbitals will be focused.

The π-molecular orbital wavefunction ψ_π can be defined in the first approximation as linear combinations of the atomic p-orbitals with wavefunction Φ_l :

$$\psi_\pi = \sum_{l=1}^{N} a_l \Phi_l \qquad (2.1)$$

where N is the number of carbon atoms in the molecule, a_l are linear coefficients, and the sum goes over all carbon atoms (Pope et al. 1999). For N carbon atoms, orthogonal N molecular orbitals in the given hermiticity of Hamiltonian can be defined. According to Pauli-Exclusion Principle, in the ground state of a molecule, two electrons with opposite spin fill the molecular orbitals with the lowest energies. The filled molecular orbital of the highest energy is then called the highest occupied molecular orbital (HOMO), whereas the molecular orbital with electron free next higher energy is called the lowest unoccupied molecular orbital (LUMO). The potential difference between HOMO and LUMO is called band gap that is determined by chemical structure of a material and the delocalization of the π electrons. The electron affinity of the molecule is correlated with the LUMO level. The HOMO level can be derived from the ionization potential, as shown in Figure 2.2.

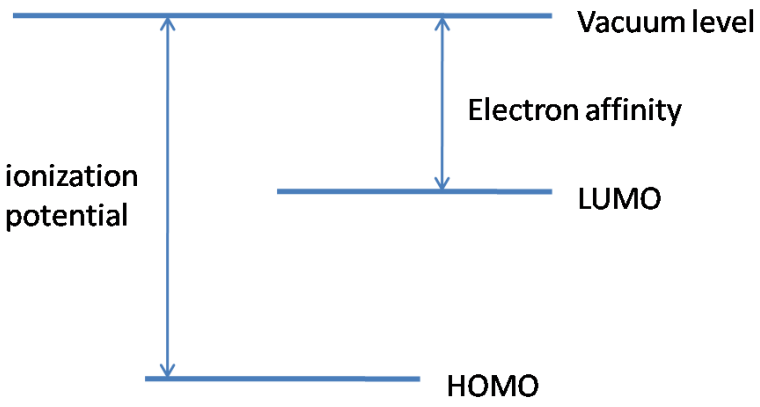

Figure 2.2. The potential difference between the HOMO and LUMO levels.

As the organic molecules of molecular solids are within close distance to each other, molecular orbitals of different molecules overlap. Therefore, a system with two molecules cannot be considered like two separate molecules, but because of the interactions between the molecules the energy of the molecular orbitals splits. As the number of the molecules that are interacting increases, the splitting energies cause a bandlike structure that is compatible with valence band and conduction band in inorganic semiconductors.

2.4. Basic OLED Device Structure

The main difference between LCD and OLED display is that OLED can emit light by themselves. Therefore, the materials for OLED must have the capability to inject charge from electrode, transport charge and finally emit fluorescence efficiently. In addition to determining the color, emitting layer materials also influence the efficiency of the devices. There are abundant organic materials to improve the device performance and to emit different colored devices.

According to their molecular weight, the materials used for OLED fabrication can be categorized into two classes; small molecules and polymers. Although organic small molecules contain only a few carbon atoms, polymers consist of a long chain of repeated units that are connected with covalent bonds.

Small molecular compounds can be deposited using thermal evaporation method under high vacuum. To improve the charge injection and recombination and thus the efficiency of the device, small molecules are fabricated as multi-layered structure. Some common small molecules used in OLED devices shown in Figure 2.3.

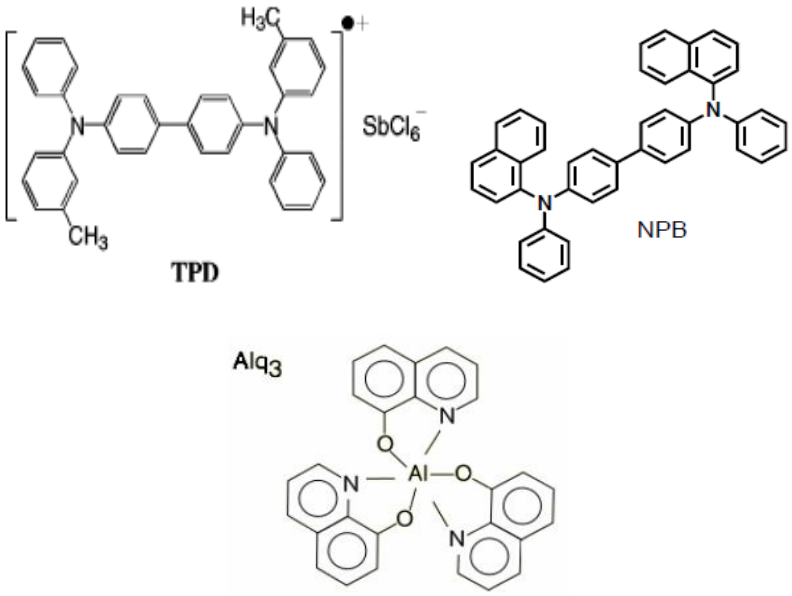

Figure 2.3. Small molecules used in OLED fabrication.

Polymers, shown in Figure 2.4., as they are solution-coatable, can be deposited using spin coating, dip coating or ink-jet printing methods. Due to the delocalized π-molecular orbitals along the polymeric chain, polymers have a property of semiconductors. Poly(*p*-phenylene-vinylene) (PPV) is the most used polymer in OLED fabrication and its derivatives have good performance in light emitting efficiency.

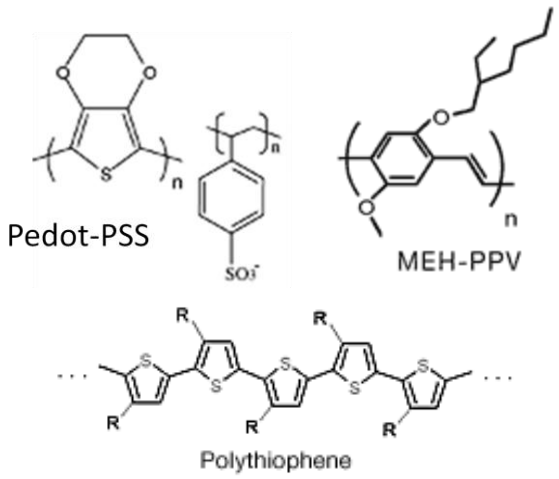

Figure 2.4. Some Polymers used in OLED devices.

2.5. OLED Device Operation

Small molecular OLEDs are typically fabricated on transparent conducting anode coated glass or flexible substrates. Due to its high work function and high transparency (90%) to visible light, most OLEDs use ITO as the anode (Wang, et al. 1996). The most extensively used technique for ITO deposition is sputtering. Thermal evaporation is the closely other used technique. Used deposition technique affects the quality and reproducibility of the film, homogeneity over a wide cross-section, ease and cost of use are the factors. The direct optical bandgap values of ITO films have been reported as in the range of 3.5 to 4.06 eV (Balasubramanian, et al. 1989, Fan, et al. 1977, Haitjema, et al. 1991, Higuch, et al. 1994, Sreenivas, et al. 1985, Szczyrbowski, et al. 1983). This wide bandgap semiconductor property of ITO films gives the high optical transmittance, T_r. The transparency and conductance is directly related with the film thickness and composition ratio of two components. The resistivity of a 200nm thick ITO is about 10^{-3} Ω.cm with mobility (μ) near to 10 cm^2/Vs. Also the reported refractive index value for ITO is 1.96 (Szczyrbowski et al. 1983). For the efficient hole injection, high work function (Φ_0) is needed as the HOMO level energies of the organic materials are typically 5-6 eV. According to applied surface treatment, the work function of ITO varies between 4.1 and 5.1 eV (Hosokawa, et al. 1995, Li, et al. 1997b, Milliron, et al. 2000, Nüesch, et al. 2000). Ultraviolet photoelectron spectroscopy (UPS) and X-ray photoelectron spectroscopy (XPS) studies have shown that surface treatment cause a generated dipole layer and modified electronic structure is therefore changed Φ_0 (He, et al. 2001, Hosokawa et al. 1995, Ishii, et al. 1999, Milliron et al. 2000, Nüesch et al. 2000, Sugiyama et al. 2000). For the reduction of the energy barrier height for hole injection, the vacuum level of ITO/organic interface is changed by the surface dipole layer (Ishii et al. 1999).

As a cathode layer, materials must have properties such as high conductivity, low work function to promote electron injection from Fermi level of the cathode to the LUMO level of organic material, good stability and film-forming. Ca ($\Phi_0 \sim 3$ eV), Mg ($\Phi_0 \sim 3.7$ eV) and Al ($\Phi_0 \sim 4.3$ eV), are the low work function materials that are used as cathode layer. As the low work function metals react with oxygen and water molecules easily, additional insulating layer such as LiF, CsF or AlO_x can be inserted to protect device from degradation and thus, reduce the barrier for electron injection (Aziz, et al.

1998, Brown, et al. 2001, Brown, et al. 1999, Brütting, et al. 2001, Burrows, et al. 2000, Jabbour, et al. 1998, Li, et al. 1997a, Piromreun, et al. 2000, Suzuki 1996, Turak, et al. 2002).

The basic device structure of multilayered OLED, as shown in Figure 2.5., consists of an anode, a cathode, a hole transport layer (HTL) and an electron transport layer (ETL).

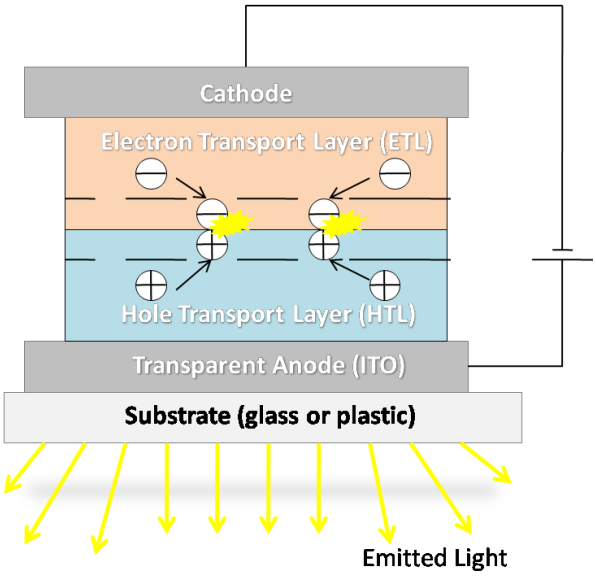

Figure 2.5. Basic structure of an OLED.

When the applied bias V_{app} is less than the built in voltage V_{bi}, most of the current is generated by free carriers of organic layer or leakage current therefore the injected current is small and negligible. At high applied forward voltage to the electrodes, electrons from cathode are injected into the LUMO level of the ETL and holes injected from the anode into the adjacent HTL. If the density of the electrons and holes are sufficiently high, the distance becomes closer and carriers travel toward the junction of the ETL and HTL where they recombine and emit light. Since the number of electrons injected is not equal to the number of holes, there is a charge imbalance which minimizes the efficiency of the device (Shinar 2004).

Working phenomenon of OLEDs is similar to that of an inorganic light emitting diode as the emission of light takes place at the interface of p-type and n-type semiconductor materials. In OLEDs light emission takes place near the interface of the

electron transport and hole transport layer. Injection of charge carriers from the metal electrodes into the organic layers, transport of charge carriers in the organic layers and recombination of charge carriers at the organic interfaces and formation of excitons are the important processes that are involved in OLEDs for the light emission (Scott, et al. 2000). These processes are discussed in literature to understand the mechanism of light emission in OLEDs.

2.5.1. Charge Injection and Transport

Under the conditions of a low electric field (<10^4 V/cm), all of the organic molecular materials used for OLED devices electrically behave as an insulator. As the vacuum sublimed organic films have the resistivity in the order of 10^{15} Ω-cm, without chemical doping no net charge carriers can be present in purified organic materials intrinsically. However, very high current density up to 1A/cm^2 in OLED can be obtained in operation. For the explanation of the high current densities new mechanisms were introduced: carrier injection at electrode/organic interface, space charge limited current (SCLC) and trap charge limited current (TCLC). Carrier injection at an electrode/organic interface and SCLC, large current density is provided. As mentioned before, electronic structure of OLED based on the individual molecules located at HOMO and LUMO levels of organic thin film. To form narrow conduction and valence bands, each molecule interacts with Van der Walls forces. The intrinsic carrier densities of organic semiconductors based on impurities and irregular structures of thin films are very low (~ 10^3-10^5/cm^3). Also, charge mobility in organic semiconductors is smaller than that in inorganic materials ($\mu_{organic}$~ 10^{-3}-10^{-7} cm^2/V-s, $\mu_{inorganic}$~ 1-$10^3$$cm^2$/V-s. Carriers are injected into organic layer via Schottky thermal injection and Fowler-Nordheim tunneling injection.

2.5.1.1. Schottky Injection and Fowler-Nordheim Tunneling

When the energy barrier is too high at the organic/electrode interface to generate any high current density, through the localized levels, Schottky thermal injection is induced by structural defects or unexpected impurities. When a contact between the

electrode and the organic layer is established, due to Coulomb attraction between the injected electrons and left holes in the metal, the image force potential is formed. This image potential lowers the energy of the interface states and makes them energetically available for the electron hopping from the metal Fermi surface. Unfortunately, with increasing distance from the interface decreases the image force potential and thus bulk states deep in organic layer remain energetically unavailable for charge hopping. As a result of applied external electric field the energy of the available states in the bulk lowers and thus hopping into bulk states away from the interface becomes possible (Singh 2009).

In the Fowler-Nordheim tunneling injection, hopping into the energetically available state in the bulk occur with the penetration of electrons located on the metal Fermi state through the thin triangular energy barrier. The two injection mechanisms are illustrated below in Figure 2.6. (a) the Schottky carrier injection and (b) Fowler-Nordheim Tunneling.

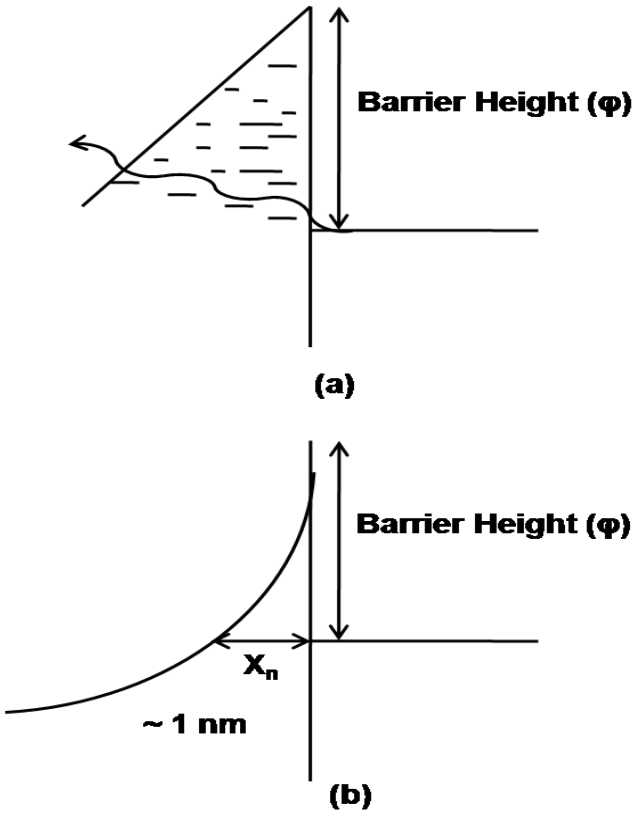

Figure 2.6. Two injection mechanisms at the organic/metal interface (a) Schottky carrier injection (b) Fowler-Nordheim tunneling.

In Schottky injection mechanism when adequate thermal energy needed to cross the barrier height is acquired, electrons from the metal electrode can be injected. The process can be described by the equation (Scott 2003)

$$J = \left(\frac{4\pi qmk}{h^3}\right) T^2 exp\left(\frac{-q\Phi_{Bn}}{kT}\right)\left[exp\left(\frac{qV}{kT}\right) - 1\right] \quad (2.2)$$

where q is the electron charge, m is the effective mass of the electron or hole, k is the Boltzmann's constant, h is the Planck's constant, T is the temperature, Φ_{Bn} is the barrier height and V is the applied voltage.

The current-voltage characteristics for q(V-Rs) > kT values of the diodes can be analyzed by the relation (Rhoderick, et al. 1988, Sze 1981);

$$I = I_0 exp\left(\frac{q(V - IR_s)}{nkT}\right)\left[1 - exp\left(-\frac{q(V - IR_s}{kT}\right)\right] \quad (2.3)$$

where is the I_0 saturation current and expressed as:

$$I_0 = AA^* T^2 exp\left(-\frac{q\emptyset_B}{kT}\right) \quad (2.4)$$

where R_s is the series resistance, q is the electron charge; V is the applied voltage; A^* is the effective Richardson constant; A is the effective contact area; T is the absolute temperature; k is the Boltzmann constant; n is the ideality factor; $\emptyset_B$ is the barrier height. The saturation current obtained from the linear portion intercept of log I at zero voltage.

The ideality factor and barrier height values of the four diodes were calculated from the slope of the linear region and y-axis intercept of the forward bias ln(I)-V curve. The obtained ideality factors that higher than unity indicates that diodes show non-ideal behavior because of the interface layer and series resistance. This significant series resistance effect can be analyzed by Cheung's functions (Cheung, et al. 1986):

$$\frac{dV}{d\ ln(I)} = n\frac{kT}{q} + IR_s \tag{2.5}$$

and a H(I)function can be defined as follows

$$H(I) = V - n\frac{kT}{q} ln\left(\frac{I_0}{AA^*T^2}\right) = IR_s + n\phi_B \tag{2.6}$$

For the Fowler-Nordheim tunneling injection, the current flow can be described by the following equation (Scott 2003):

$$J = \left(\frac{q^3V^2m_0}{8\pi h\Phi_{Bn}m^*}\right) exp\left(\frac{-4(2m^*)^{0.5}{\Phi_{Bn}}^{1.5}}{3hqV}\right) \tag{2.7}$$

where J is the current density, V is the voltage, h is the Planck's constant, m_0 is the mass of the free electron, q is the charge of the electron, m^* is the effective mass.

The charge injection process in OLEDs is described as a combination of these two injection mechanisms. It is described by J.C. Scott as a thermally assisted tunneling injection from the delocalized states of the metal to the localized organic layer (Scott 2003). The I-V characteristics of the OLEDs are due to these charge injection effects.

2.5.1.2. Space Charge Limited Current

If the applied electric field is less than 10^4 V/cm, the number of the charge carriers injected into the organic layer is less than the intrinsic charge carriers present in the organic layer and thus the current flow is governed by Ohm's law. Charge accumulations that were caused by charge injection into low mobility organic materials, partially screen out by the applied electric field. With the high external electric field (>10^5 V/cm), due to low carrier mobility, near the electrode/organic interface the injected current density is higher than the intrinsic charge density therefore the internal electric is enhanced by the space charges (Singh 2009). This type of current regime is called as space charge limited current (SCLC) and given by the Mott-Gurney equation (Mott, et al. 1940)

$$J = \frac{9\varepsilon\varepsilon_0\mu V^2}{8L^3} \tag{2.8}$$

where ε is the relative dielectric constant, ε_0 is the dielectric constant and L is the sample thickness and μ is the field independent charge carrier mobility. In the absence of traps or a single shallow trap level, current-voltage curves predicted by this model are supralinear. In OLEDs, the transport and the injection properties are determined by inter site hopping from delocalized states in the metal to localized states in the organic layer. The transition rate depends on the energy difference and distance between one site to another. Narrow bands around the HOMO and LUMO levels are formed by the energy states that are involved in the hopping transport of holes and electrons. The intermolecular interactions and level of disorder determine the widths of these bands. To improve the conduction in device where strong injection is achieved from both electrodes, the SCLC type mechanisms are needed. When an external electric field is applied, the holes are injected from anode into the HTL and drift or hope across it. Due to low hole mobility in the electron transport layer ETL, holes decelerate at the internal interface. According to Haichaun Mu, the same mechanism is also valid for electrons as they cross organic/organic interface, which leads to substantial charge accumulation at the interface (Mu 2011). The dependence of mobilities on electric field is best described by the Poole-Frenkel type of behavior given by the following equation (Blom, et al. 1998):

$$\mu = \mu_0 exp\left(\frac{-\Delta}{kT}\right) exp\left(\gamma\sqrt{E}\right) \tag{2.9}$$

where Δ is the activation energy, μ_0 is the temperature independent prefactor, k is the Boltzmann's constant and T is the temperature and E is the applied electric field to the terminals of the device. In the above equation, μ is directly proportional to $\sqrt{E}$ which points out the electric field dependence on mobility.

2.5.1.3. Trap Charge Limited Current

Besides being localized to individual molecules, charges can also accumulate in traps, typically at organic layer interfaces or at defects within the film. Due to the strong injection, the local increase in the quasi-Fermi level may lead to charge immobilization in the deeper states of the disorder induced distribution of HOMO and LUMO levels. In the presence of the traps, when forward bias is increased, the electron quasi-Fermi level arises towards the LUMO with increasing injected electron density. If the traps are distributed in energy, they will gradually fill with increasing field and the current will increase faster than quadratic in SCLC until traps are filled (Singh 2009). This model is called trap charge limited current (TCLC), in which a high power dependence of current on voltage is observed. The trap density of the states is well described using an exponential distribution of traps using the equation;

$$N_t(E) = \frac{N_t}{kT_t} exp\left(\frac{E - E_{LUMO}}{kT_t}\right) \tag{2.10}$$

where N_t is the total trap density, k is the Boltzmann's constant and T_t is the characteristic temperature of the exponential trap distribution (T_t=E_t / k, where E_t is the characteristic trap energy). Therefore, below the quasi-Fermi level in the high injection currents, the filling of traps controlled by the density and energy distribution of the traps. The current density is also described by the equation;

$$J_{TCL} = \frac{V^{m+1}}{d^{2m+1}} \tag{2.11}$$

where $m = T_t/T$.

2.5.1.4. The Role of Interfaces for Charge Injection

There are two main reasons for electronic level misalignments at the interfaces which lead to the contact-limited injection regime: One of them is the mismatch of work

functions of electrode and electron affinity of the material in the device as shown in Figure 2.7. Another one is the presence of additional barriers between organic layers.

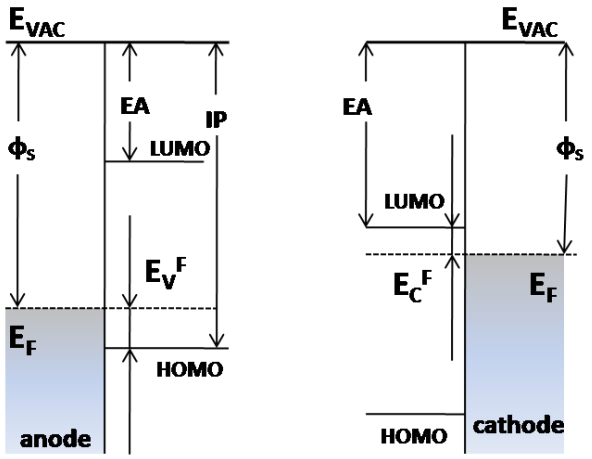

Figure 2.7. The schematic picture showing the energy level alignment at the interface of an electrode and organic layer. In these cases vacuum level alignment is assumed.

In both cases presented in Figure 2.7., vacuum level is assumed as the reference. The work function Φ of the anode and the cathode is the position of Fermi level to vacuum level. Photoelectron spectroscopy is used as to characterize technique to obtain work function and threshold ionization potential of a molecule and thus the hole injection barrier can be estimated (Singh 2009).

The assumption of common vacuum level is not easy when inorganic electrode and organic materials are involved. In literature, it is investigated that the interfacial dipole is formed due to the formation of chemical bonds or charge transfer, and manifests itself as a vacuum level offset (denoted as Δ) (Blochwitz, et al. 2001, Chkoda, et al. 2000, Crispin, et al. 2002, Giebeler, et al. 1999, Ishii, et al. 2000, Ishii et al. 1999, Kera, et al. 2004, Mäkinen, et al. 2001, Osikowicz, et al. 2004, Peisert, et al. 2004, Salaneck, et al. 1996). Such offset influence on the magnitude of the barrier is shown in Figure 2.8.

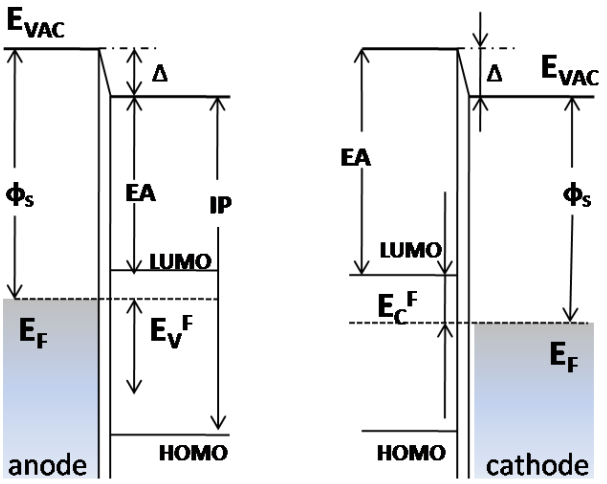

Figure 2.8. Schematic picture showing the energy level alignment at the interface of an electrode and organic layer. In these cases vacuum level shift is present, which increases injection barriers.

When the work function of the substrate (Φ_s) equals to the ionization potential (IP) or to the electron affinity (EA) of the organic material, as a result of vacuum level shift there is still a barrier at the interfaces. The existence of this barrier at the interface influences the device characteristics. The large magnitude of barrier height causes smaller injection current at a given voltage and to achieve the desired intensity of light higher applied voltage is required.

The studies are still focused on the understanding and controlling the energy level alignment at the interfaces. ITO is the most used electrode at anode in OLEDs. As it is investigated in the study of Chkoda et al., although it has high work function, it has lower ionization potential than most of the HTL materials (Chkoda, et al. 2000). Besides studying on HTL materials, in order to provide the best match, also by modifying the ITO surface, the work function can be significantly increased (Besbes, et al. 2003, Ganzorig, et al. 2001, Hatton, et al. 2001, Ho, et al. 1998, Sugiyama, et al. 2000, Sun, et al. 2003, Wu, et al. 1997). The interfacial dipole is formed, when the work function exceeds the energy of integer charge transfer state (ICTS). While hole injection barriers remain constant, the magnitude of the dipole increases linearly with the work function of the substrate.

2.5.2. Langevin Recombination

The light emission from an OLED device fundamentally is generated by recombination occurred between injected hole and electron that forms various excited states such as singlet excitons, triplet excitons and charge transfer excitons. When the electric field is applied to the terminals of the OLED, both holes and electrons are injected into organic layer and two carriers start interacting. The recombination of statically independent oppositely charged carriers were first studied by Paul Langevin in 1903 (Langevin 1903). The desired condition for recombination is that the distance between the hole and the electron must be less than the Coulomb capture or Onsager radius, r_c. Onsager radius is the distance, where the Coulomb attractive potential energy equals to thermal dissociation energy (Zou, et al. 2001),

$$r_c = \frac{q^2}{4\pi\varepsilon kT} \tag{2.12}$$

As $\varepsilon \sim 3\varepsilon_0$ for most organic materials, at room temperature typical columbic capture radius is ~17 nm (Swenberg, et al. 1999). The bimolecular recombination current in the Langevin model is given by

$$R = \gamma n_e p_e = {}^{e(\mu_n \mu_p)}/_{\varepsilon n_e p_e} \tag{2.13}$$

where μ_n, μ_p are the mobilities of negative and positive charegs and n_e , p_e are the densities of the charge carriers and γ is the Langevin recombination coefficient.

2.5.2.1. Singlet and Triplet Excited States

In quantum mechanics, when one electron is excited from an occupied state into an unoccupied state it leaves a hole. A hole represents just a missing electron, it can be represented by similar wavefunctions with electron. According to Pauli Principle in a system with two particles of spin 1/2, eigenstates of the Hamiltonian must be antisymmetric with respect to the exchange of particles (Griffiths 2005). As long as the

spatial wavefunction has the opposite parity, the spin wavefunction can be either symmetric or antisymmetric since wave functions can be written as the product of the spatial and the spin wavefunctions. For the electron, the spin part of the wavefunction can be represented by $|\uparrow\rangle$ or $|\downarrow\rangle$ where arrows indicate the direction of the spin. Therefore, the four possible spin wavefunctions can be differentiated between one antisymmetric (singlet) state S_n:

$$\Psi_{spin} = \frac{1}{\sqrt{2}}(|\uparrow\rangle\,|\downarrow\rangle - |\downarrow\rangle\,|\uparrow\rangle) \tag{2.14}$$

and three antisymmetric (triplet) states T_n:

$$\Psi_{spin} = \frac{1}{\sqrt{2}}(|\uparrow\rangle\,|\downarrow\rangle + |\downarrow\rangle\,|\uparrow\rangle) \tag{2.15}$$

$$\Psi_{spin} = |\uparrow\rangle\,|\uparrow\rangle \tag{2.16}$$

$$\Psi_{spin} = |\downarrow\rangle\,|\downarrow\rangle \tag{2.17}$$

Emission of light results in the transition of singlet excitons from a single state to the ground state fast and efficiently. This is a fast and efficient radiative decay because it does not involve in spin. Transition of triplet excitons from the triple state to the ground state that involves spin flip. As a result of long transition time energy of excitons is lost in the form of phonons. Figure 2.9. shows the four possible exciton formations with one singlet formation and three triplet formations.

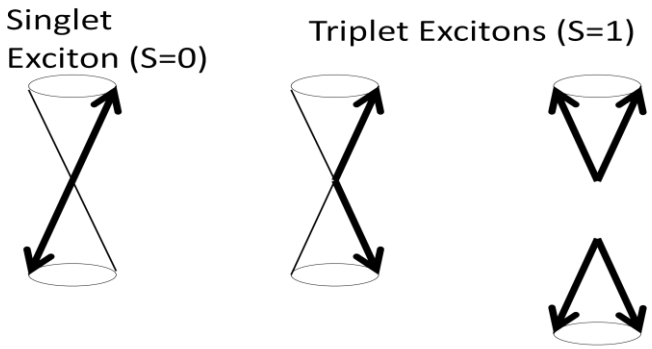

Figure 2.9. Diagram showing possible singlet and triplet excitons formation.

Formation of singlet and triplet excitons is governed by the spin orientations and phase of these orientations. The singlet exciton has a total spin angular momentum (S=0) and the triplet exciton has the total spin angular momentum (S=1).

2.5.2.2. Light Emission

After the generation of excited electronic state, the time interval until a molecule relaxes back to the ground state in radiative or non-radiative process is the given lifetime of this molecule. The probability of radiative relaxation (*P)* from state Ψ_i to state Ψ_j is proportional to the square of the transition dipole moment

$$P \propto \langle \Psi_i | M | \Psi_j \rangle^2 = \left| \int \Psi_i M \Psi_j \, d\,\tau \right|^2 \tag{2.18}$$

where M is the dipole moment operator and the integration over $d\tau$ covers the whole space of all 3*N* coordinates with the number of electrons *N*. The dipole moment operator M can be expressed by

$$M = \sum_i e r_i \tag{2.19}$$

where e is the electron charge and r_i is the distance of the i th electron from the origin of a coordinate system that is fixed to a molecule. Since the dipole moment operator

does not affect the spin part of the wavefunction of a state, only similar spin symmetry transitions result in transition dipole moment that is different from zero. Having absorbed energy and reached one of the higher levels of an excited state, molecule rapidly loses its excess amount of energy by collisions and falls to the lowest singlet excited state (S_1). Light emission is generated with the return of electron to the various levels of the ground singlet state (S_0). The resulting radiation from such transitions is called fluorescence.

Phosphorescence emission is the photon emission caused by the transition of the molecule from lowest triplet excited state to (T_1) to the ground state (S_0). In addition to the phosphorescence, both singlet and triplet character of the excited states in spin-orbit coupling is also possible for transitions between the lowest excited singlet state S_1 and the lowest triplet excited state T_1, the so-called intersystem crossing (ISC). According to Hund's rule the energy of T_1 is generally lower than the energy of S_1. Therefore, it is more useful for an excited singlet state to relax to the ground state through intersystem crossing to the triplet state that is phosphorescent emission instead of a fluorescent relaxation (Haldi 2008). A Jablonski diagram of the radiative and non-radiative transitions is shown in Figure 2.10.

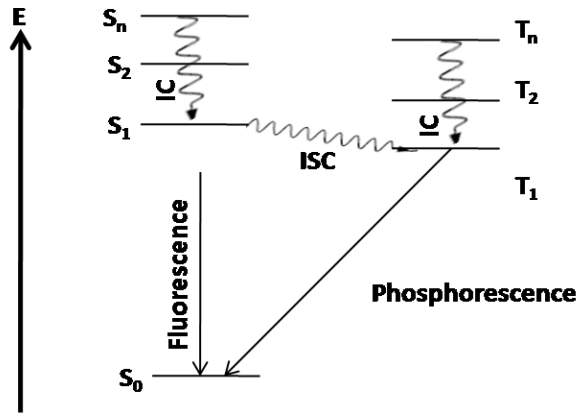

Figure 2.10. Jablonski diagram of electronic singlet and triplet states and possible transitions between these states.

In the figure, solid arrows represent radiative transitions, curvy lines show non-radiative transition from higher excited states to the lowest excited state (internal

conversions, IC) and nonradiative transition from the lowest singlet to the lowest triple state (intersystem crossing, ISC).

2.5.3. OLED Efficiency and Light Outcoupling

2.5.3.1. Efficiency

The most often reported performance quality of the OLED is its external quantum efficiency (EQE). EQE is defined as the number of photons released from the device per number of injected hole-electron pairs. The product of the internal quantum efficiency η_{int} (number of photons generated inside the device per number of injected hole-electron pairs) times the outcoupling efficiency (η_{ph}) gives the external quantum efficiency (η_{ext}) (Adachi, et al. 2001):

$$\eta_{ext} = \eta_{int}\,\eta_{ph} \tag{2.20}$$

where the internal quantum efficiency is dependent on the device architecture and the material properties of the device:

$$\eta_{int} = \gamma\eta_{ex}\,\Phi_p \tag{2.21}$$

where γ is the electron-hole charge-balance or Langevin recombination factor, η_{ex} is the efficiency of the formation of excited electronic states that lead to radiative transitions, and Φ_p is the photoluminescence quantum yield.

The photoluminescence quantum yield (Φ_p) is a material constant that is described by the number of radiative transitions per the number of total transitions from the excited states to the ground state in a material. η_{ex} is also dependent on the material that is given by the nature of the emission. As it is mentioned before, in fluorescent devices radiative transitions occur only from the singlet excited state; therefore, η_{ex} can only reach 25% upper limit since only one out of the four excited states is a singlet state in small molecules (Baldo, et al. 1999). On the other hand, in polymers with longer

chain length attribute to a faster decay of higher excited states in compounds and thus η_{ex} can exceed the limit of singlet excited states up to 60% (Beljonne, et al. 2004, Meulenkamp, et al. 2004).

In phosphorescent devices, all three triplet excited states participate in the light emission. With the relaxation of high energy singlet excited state into the triplet state through intersystem crossing, η_{ex} with 100% can be achieved (Adachi et al. 2001).

2.5.3.2. Light Outcoupling

General structure of OLEDs consists of ITO coated glass substrate that acts as a transparent and conductive electrode, organic layer deposited and finally metal cathode. As the light is extracted through the glass substrate, such devices are usually referred to as bottom-emitting OLEDs as it is shown in Figure 2.11. However, this device architecture is not very efficient in coupling out the emitted light through the substrate and the into the viewer's eye.

An estimated maximum light output of the bottom-emission geometry can be calculated using simple ray theory assuming that the cathode acts as a perfect mirror. The amount of light energy transmitted from a medium 1 with refractive index n_1 into a medium 2 with refractive index n_2 normalized by light energy incident on the interface between medium 1 and 2 is given by (He, et al. 2004, Kim, et al. 2000):

$$\eta_{ph} = 1 - \sqrt{1 - \left(\frac{n_2}{n_1}\right)^2} \approx 0.5 \left(\frac{n_2}{n_1}\right)^2 \tag{2.22}$$

As long as there is no local minimum of the refractive index within the multilayer structure, this equation holds even for multilayer structures (Gu, et al. 1997). In literature, there have been studies on improving the outcoupling efficiency. Most of the researchers focus on treating the emitting surface of the glass substrate to avoid internal total reflection between glass and air (Krummacher, et al. 2006, Madigan, et al. 2000). Additionally, to avoid waveguiding effects from ITO to glass interface is modified (Agrawal, et al. 2007, Tsutsui, et al. 2001). However, basic bottom-emitting OLEDs have the same intensity independent of the observer's angle (Lambertian

emitter), improvements mostly occur mostly in the direction perpendicular to the glass substrate which is typically not Lambertian (Agrawal et al. 2007).

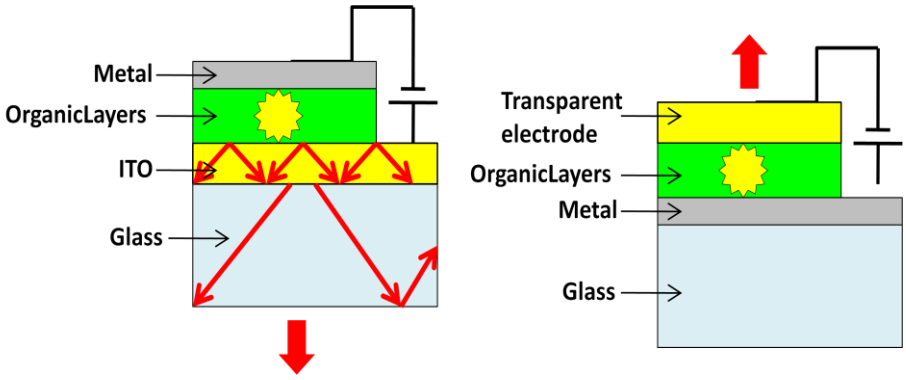

Figure 2.11. Bottom-emitting (left) and top-emitting (right) OLEDs. Arrows in the bottom-emitting OLED represent light that is waveguided in the ITO or in the glass.

Alternatively, top-emitting OLEDs have been studied to avoid wave guiding effects in the ITO layer and the glass substrates (Dobbertin, et al. 2003, Riel, et al. 2003). While the top electrode is transparent, top-emitting OLEDs are fabricated on metal coated substrate that fully reflect the light. However, as a result of surface Plasmon-polariton modes that occur at metal surfaces, the external quantum efficiency can only reach about 20 to 25% (Huang, et al. 2006, Smith, et al. 2004).

CHAPTER 3

SELF-ASSEMBLED MONOLAYERS

The formation of monolayers by the adsorption of an active surfactant molecules on surfaces is one of the examples of general self-assembly phenomena. To increase the fundamental understanding of self-organization, structure-property relationships and interfacial phenomena, SAMs offer unique opportunities (Ulman 1996). SAMs are well-defined and accessible ideal systems in many fields. They provide invaluable substrates in bioanalytical, organometallic, physical organic, bioorganic and electrochemistry (Bishop, et al. 1996, Dubois, et al. 1992). The most common monolayers are formed with organosilicon derivatives, alkane thiols, dialkylsulphides, alcohols, amines and carboxylic acids on different substrates. Therefore, a variety of surfaces with specific interactions can be produced with fine chemical control (Ulman, et al. 1991).

3.1. History of SAMs

Self-assembly monolayer has been studied greatly because of their potential applications in wettability, modification, bicompatiblity and corrosion resistance of substrate surface over the past two decades. However, the researches in this field really began much earlier. The preparation of a monomolecular layer by adsorption of a surfactant onto a clean metal surface (self-assembly) was first published in 1946 by Zisman (Bigelow, et al. 1946). The importance of SAMs was understood with a novel electronic device concept from the mid 1970's. At that time, that is early development of integrated circuit technology, the study of Aviram and Ratner brought out an idea of using molecules to carry out tasks such as energy, storage and charge transfer which are normally reserved for solid state electronic devices. In 1974, they made a molecular rectifier that consisted of donor and acceptor π bonded systems separated by a σ bonded tunneling bridge (Aviram, et al. 1974). Exhibiting a nonlinear rectifying behavior, under an applied electric field current wouldn't allow to bypass equally well in one direction as in the other. This molecular rectifier device remained theoretical concept for the next

twenty years while over the next quarter century improvements in processing techniques created higher density, small feature sized and faster silicon-based transistors.

In today's photo-electronic and electronic fabrications, SAMs have been used as bridging layers to assemble nano-particles onto the ITO surface for enhancing incident photon energy to current conversion efficiency of a solar cell (Shipway, et al. 2000, Subramanian, et al. 2001). Modification of ITO surface using SAMs were found to increase the adhesion between inorganic ITO and organic hole-transport layer and thus reduce the pinholes in the final OLED device (Carrard, et al. 1999, Lee, et al. 2002).

3.2. Types of SAMs

There are several different kinds of SAMs. One class is constituted from carboxylic acids on aluminium oxide (Allara, et al. 1985, Ogawa, et al. 1985), silica (An, et al. 2007), silver (Schlotter, et al. 1986) and ITO (Cerruti, et al. 2007). Long alkane chains terminating in a –COOH group are the amphiphiles and the surfaces become hydrohobic upon the monolayer formation. The other class of SAMs are alkylsilane derivatives, $RSiX_3$, R_2SiX_2 or R_3SiX where X is chlorine or alkoxy and R is a long alkyl chain with or without a functionality. Substrates on which these monolayers have been successfully prepared including silicon oxide (Sagiv 1980, Wasserman, et al. 1989), aluminium oxide (Gun, et al. 1984, Tillman, et al. 1988), quartz (Brandriss, et al. 1993, Mathauer, et al. 1993), glass (Gun et al. 1984), mica (Carson, et al. 1989, Schwartz, et al. 1992), zinc selenide (Gun et al. 1984), germanium oxide (Gun, et al. 1986) and gold (Finklea, et al. 1986, Sabatani, et al. 1987). During a surface consisting of hydroxyl groups such as SiO_2, SnO_2 or TiO_2 is exposed to a solution of these molecules for a few minutes, surface hydroxyl groups react with Si-Cl bonds and chain of Si-O-Si bonds forms at the surface leading to a compact monolayer. One of the more recent additions to material classes is alkane thiol, alkylsulphide and dialkyldisulphide monolayers on gold, silver and cupper. An alkanethiolate monolayer is formed by the chemisorption of the sulphur atom on the surface . Nowadays, almost all functionalities have been made on the monolayer. Figure 3.1. shows the schematic representation of SAM and alkanethiol molecule.

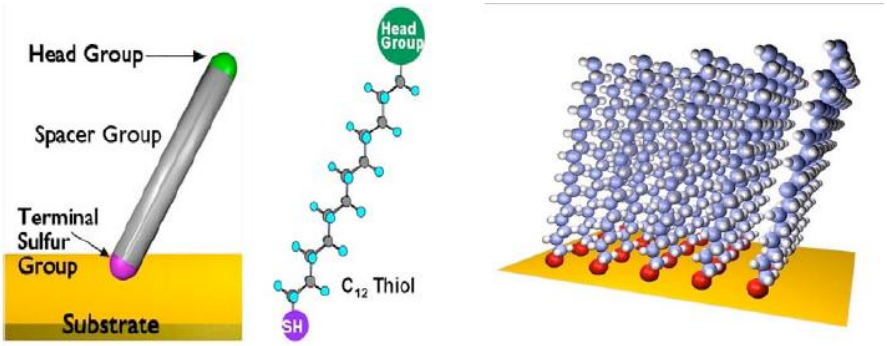

Figure 3.1. Schematic representation of SAM and alkanethiol molecule (Source:(Asemblon 2005)).

3.3. SAM Formation

As mentioned before, SAMs are well-oriented molecular structures formed by the adsorption of an active surfactant on a substrate surface. As a result of intramolecular, intermolecular and interfacial forces, ordered 2D and 3D polymolecular structures can be obtained. Substrate selection and preparation is very important issues for reproducibility and atomic level flatness as they are needed for the base of support upon which the monolayer forms. Atoms and molecules are bounded to surface in two ways; physisorption that is corresponding to physical adsorption and chemisorptions that is corresponding to chemical adsorption.

Physisorption is the adsorption of a thin layer of molecules to a surface without the formation of a chemical bond. The binding is resulted from hard core repulsions and the interplay of weak attractive forces such as Van der Waals and electrostatic forces which exist over long ranges. Physisorption is a reversible process and the adhesion involved can also take place in multilayer. On the other hand, chemisorption is the adsorption of molecules to a surface through the formation of a chemical bond. Depending on the covalent bonds between active surfactant molecules and surface, the type of the interaction is strong. Also the enthalpy of the chemisorptions process is higher than that of physisorption.

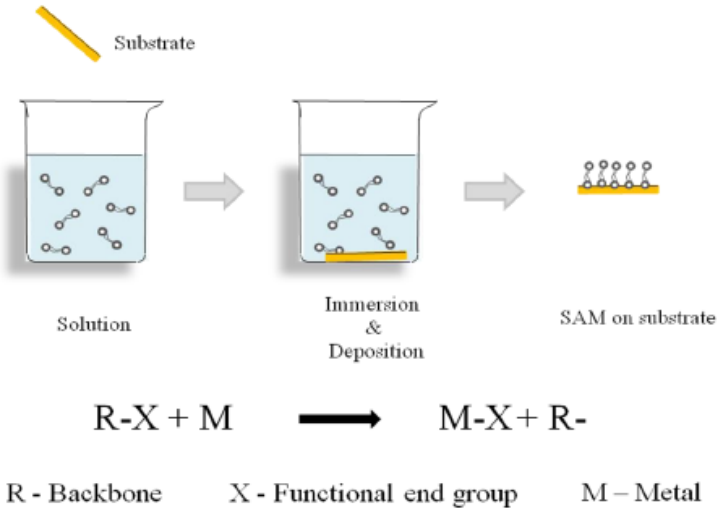

Figure 3.2. A schematic representation of SAM formation by immersing a substrate into a solution containing a surface-active material consisting of backbone R and functional group X. The end group reacts chemically with the metal and the material, spontaneously forming a 2D assembly. (Source: (Thiruvengadam 2002)).

SAMs are formed spontaneously upon the immersion of a substrate into a solution containing an active surfactant molecule in organic solvent (Figure 3.2.). These molecules consist of three parts as follows:

1. A surface active head group enhances chemisorption to the substrate and binds the molecule to the substrate surface strongly. The bonding can be covalent (e.g. Si-O-Si on oxidized surfaces), covalent and slightly polar (e.g. Au-S for alkanethiols on gold), and ionic. Molecules try to anchor to every available binding site on the surface due to substrate-head group interaction and tend to pack in one beside the other.
2. Chain or backbone takes place in the packaging density of the molecules. When the distance between the adjacent molecules is very small, short-range dispersive Van der Waals forces become effective. Thus, due to these interactions molecules tend to reorganize.
3. A specific tail group constitutes the other surface of the film and modifies the bulk surface properties. Figure 3.3.shows the chemisorption reaction of a surfactant molecule on a substrate.

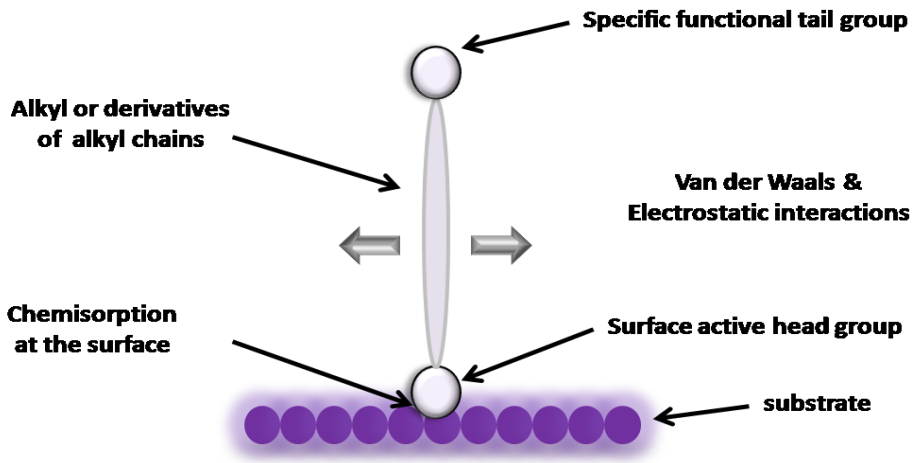

Figure 3.3. A schematic diagram showing chemisorptions reaction of a surfactant on a substrate.

The presence of a monolayer can affect the acidity and basicity of the surface (Kane, et al. 1998, White, et al. 1998). Ionization of the monolayer leads to an accumulation of charge across the surface. The formation of a double-layer changes the pH in the neighboring of the monolayerfrom that of the bulk solution. In general acids become less acidic and bases become less basic.

Sterics or bulky groups play an important role in the reactivity of monolayers. Strongly adherent monolayers can prevent cis-trans photoisomerism of azobenzene molecules. Photoisomerism in the stilbene molecule is considered as a prototype of the general rearrangement reactions induced by absorption of light. When spacer molecules become coherent into the monolayer surface, photoisomerism is observed (Evans, et al. 1998, Gelbart, et al. 1969).

3.4. SAM Characterization Techniques

3.4.1. Quartz Crystal Microbalance (QCM) Technique

Because of their relatively low cost and their ability to accurately and sensitively measure mass changes in real time quartz crystal microbalances (QCMs) are mostly used tools in vacuum deposition processes. Use of QCMs become more extensive with

the development of oscillator control circuitry capable of maintaining stable oscillation in crystals under heavy viscous liquid and non-rigid film loading. Increasing sophisticated theoretical treatments of oscillators are also very useful for QCM measurements in liquid. Early work of Sauerbrey based on the simple relation between the frequency shift (Δf) of the quartz crystal resonator and changes of its mass per unti surface area (Δm) (Sauerbrey 1959):

$$\Delta f = -\frac{2{f_0}^2 \Delta m}{A\sqrt{\mu\rho}} \tag{3.1}$$

where μ and ρ are the shear modulus and the density of quartz (2.95×10^{11} dyne/cm^2 and 2.65 g/cm^3, respectively), f_0 is the fundamental oscillation frequency (resonance frequency) of the dry crystal and Δm is the mass of the material absorbed on the surface per unit/area. Constants like thickness, the density and the shear modulus of the quartz and the physical parameters of the adjacent media, such as density or viscosity of the liquid, can influence the oscillation frequency. As there can be a difference between running buffer and sample, it is important to separate each frequency variation signal (Tlili, et al. 2004).

When a clean gold substrate is immersed in an SAM solution, net chemisorption reaction is occurred. The Langmuir adsorption isotherm model was derived initially for physisorption reactions, not chemisorptions, but the bond strength of the SAM-ITO coated gold substrate bond is small enough that this condition is not violated seriously. This model assumes that adsorption is limited to one monolayer that the all surface sites are equivalent. Although there are defects on gold the gold surface, the resultant modulation of surface site energies is small enough so that Langmuir approximation holds.

Assuming Langmuir adsorption kinetics, the rate of formation of the monolayers can be expressed by;

$$\frac{d\theta}{dt} = k_a(1-\theta)C - k_d\theta \tag{3.2}$$

where θ is a unitless quantity which expresses the fraction of a monolayer formed, C is the molecule concentration in the solution, and k_a and k_d are the rate constants for the adsorption and desorption processes, respectively. The difference between the resonance frequency of the uncoated QCM and the oscillation frequency measured as the monolayer forms is directly proportional to the fraction of the surface that has been covered, θ.

Integration of equation 2.20 leads to:

$$\theta(t) = \frac{C}{C + \frac{k_d}{k_a}}\left(1 - e^{-(k_a C + k_d)t}\right) \tag{3.3}$$

Setting:

$$k_{obs} = k_a C + k_d \tag{3.4}$$

and

$$k' = \frac{C}{C + \frac{k_a}{k_d}} \tag{3.5}$$

results in the equation:

$$\theta(t) = k'(1 - e^{k_{obs}\, t}) \tag{3.6}$$

If the fractional coverage θ is measured as a function of time t, k_{obs} and k' can be determined by fitting experimental data to equation 2.24. Also a plot of k_{obs} versus C yields a line with slope k_a and y-intercept of k_d (equation 2.22).

The equilibrium constant for this reaction K_{eq} is equal to the ratio of k_a/k_d and the free energy of adsorption ΔG_{ads} at a given temperature is given by:

$$\Delta G_{ads} = -RTlnK_{eq} \tag{3.7}$$

Since:

$$\Delta G_{ads} = \Delta H_{ads} - T\Delta S_{ads} \quad (3.8)$$

both ΔH_{ads} and ΔS_{ads} can be determined by carrying out the experiment over a range of temperatures. Slope of the plot of ΔG_{ads} vs. T gives the $-\Delta S_{ads}$ and y-intercept gives ΔH_{ads}.

3.4.2. Atomic Force Microscopy (AFM)

The Atomic Force Microscopy (AFM) is a very high-resolution form of scanning probe microscope that demonstrates resolution of fractions in nanometer scale. Using AFM technique, thin and thick film coatings, ceramics, composites, glass, synthetic and biological membranes, metals, polymer and semiconductors can be investigated. It is also being applied to studies such as erosion, drafting, dip pen writing, nano-structure fabrication, indenting and lithography. AFM was not only used in image extraction, but also used in force measurements at the nano-Newton scale.

With the invention of scanning probe microscopy (SPM) in 1982 by Gerd Binning and Heinrich Rohrer, it is possible to generate real-space images of surfaces with a resolution on the nanometer scale. Four years later in 1986, Binning and Rohrer were awarded the Nobel Prize in Physics for their invention of a new type of microscope, the atomic force microscope (AFM), which is capable of investigating surfaces of insulating materials on an atomic scale (Binning, et al. 1986).

In the near past of AFM, it has proven itself to be as versatile as it is essential to nanoscale materials characterizations. For example, in 1987, Marti et al. imaged highly oriented pyrolytic graphite (HOPG) and cleaved sodium chloride surfaces covered with paraffin oil (Marti, et al. 1987). This study illustrated the capability of AFM for studying either conducting or nonconducting surfaces or even liquid covered surfaces. Albrecht and his coworkers demonstrated the capability of the AFM to image the surface of an electrically insulating solid in air with low –noise atomic resolution (Albrecht, et al. 1987). A novel optical approach to AFM was achieved by Meyer et al. in which a sensitive and simple optical method was introduced for detecting deflection

of the cantilever and after than AFM was based on sensing forces between a sharp stylus and the surface of interest (Meyer, et al. 1988). The effect of Van der Waals interaction between sharp probes and the flat sample surfaces was investigated by Hartmann (Hartmann 1991) and the calculation of the attractive Van der Waals forces that were expected between tips and samples were made by Goodman et al. (Goodman, et al. 1991).

In 1991, Weisenhorn et al. studied the imaging lipid Langmuir-Blodgett (LB) films with different surface charges and DNA with molecular resolution (Weisenhorn, et al. 1991). Since the increased applied force could scrape off the two films, the molecular arrangement of the lipids in the LB films agreed with known 3D crystal data to within only 20% accuracy. Within a decade of the discovery of AFM there was considerable amount of interest in the electronic properties of single molecules wired into electronic circuits. Until then, there have been a lot of studies including alky and benzyl thiol SAMs on Au, Pt and Ag substrates (Chen, et al. 2001, Cui, et al. 2002, Engelkes, et al. 2004, Wold, et al. 2001).

AFM investigates the surface of a sample using a sharp tip with a terminal radius often less than 100 Å. The tip is located at the free end of an approximately 100 μm long cantilever. A laser beam is focused on the back side of the cantilever, right above the tip, and reflected beam detected by a position-sensitive photodetector. The representation of the basic principle of AFM is shown in Figure 3.4. Any changes in the cantilever position are caused to the laser position change in the photodetector. A mechanical amplification is produced by the ratio of the path length between the cantilever and the detector to the length of the cantilever itself. Thus, the system can also detect the sub-Angstrom vertical deflections of the cantilever tip. The measured cantilever movements are used to generate a map of surface topography by software.

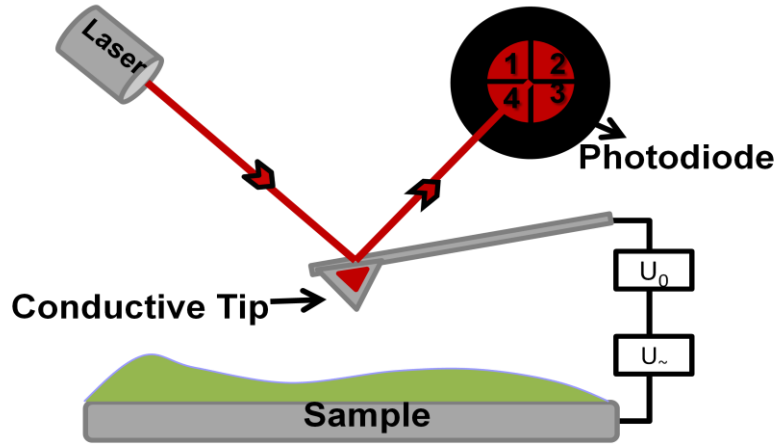

Figure 3.4. Representation of basic principle of AFM and photodiode sections.

To prevent any collisions of tip to the surface, a feedback mechanism is employed to adjust the tip-to-sample distance and to maintain a constant force between the tip and the sample. Mechanical forces are the strongest forces between the tip and the sample that occur when the atoms on the tip physically interact with the atoms on a surface. However, there are other forces classified as long range forces, such as Van der Waals forces, electrostatic and capillary forces, and short range forces, such as repulsive forces, covalent bonds, metallic bonding and friction, that have impact on an AFM images.

The contributions of the forces that are on the basis of the Lennard-Jones potential can be expressed as:

$$\varepsilon(r) = -4\varepsilon_0 \left[\left(\frac{\sigma}{r}\right)^6 - \left(\frac{\sigma}{r}\right)^{12} \right] \tag{3.9}$$

where ε_0 is the potential energy at the minimum, σ is the effective molecular diameter and r is the interatomic distance. The force, which is the negative gradient of the energy plotted against the distance, is shown in Figure 3.5. The two distance regimes, the contact regime and non-contact regime are highlighted. In contact regime, the distance between the cantilever and the surface is only few Angstroms, and the interatomic force is repulsive. In the non-contact regime, the distance between the tip and the surface is tens to hundreds of Angstroms and the interatomic force is attractive largely due to Van der Waals interactions.

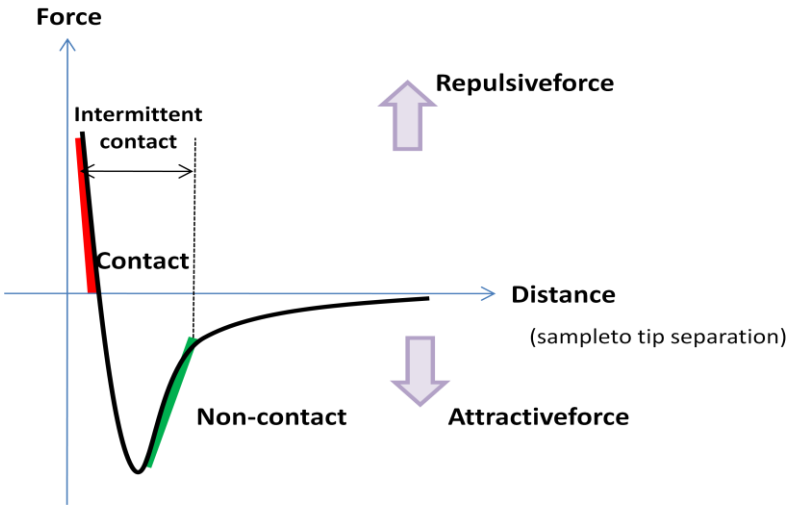

Figure 3.5. Interatomic force vs. distance curve.

Besides using it to image variety materials such as layered materials, ionic crystals, organic molecules, and biological sensors, AFM has been used to image the surfaces of graphite and mica as well as organic molecules forming LB films and biological samples like DNA. In addition, to use in the formation of nanoscale junctions, an AFM tip can be coated with conducting materials. These heterostructures or tunneling junctions can be used in the electron transport mechanism studies in two terminal electronic devices.

3.4.3. Kelvin Probe Force Microscopy (KPFM)

The Kelvin Probe Force Microscopy (KPFM) was invented in 1991 (Nonnenmacher, et al. 1991). It was derived from existing atomic force microscopy and measures the work function in conducting materials or the surface potential in nonconducting materials on nanometer scales. KPFM can provide an analysis of electrochemically etched surfaces, surface analysis of semiconductors, charge distribution analysis on the surfaces and also surface potential measurements in lipid membranes. KPFM is the combination of AFM and macroscopic Kelvin method that it uses the principles of the Kelvin method but it can be achieved by AFM with a nanoscale lateral distribution. The Kelvin method has been attributed to Lord Kelvin for a century. The Kelvin method measures the work function, work required to remove the

valance electron from an atom, in metals and the surface potential in nonmetals to within 0.0001V. Suppose that, two metals have two different Fermi levels (the energy of the highest occupied quantum state in a system of fermions). Then, the work function is the difference between the Fermi level and the highest possible Fermi level of the system. If the external contact is made between these metals, electron transfer is occurred to equalize their Fermi levels. This electron flow creates the contact potential difference (CPD) between the two surfaces, where they are oppositely and equally charged. If the bias voltage is applied, the flow of the electrons can be stopped. The Kelvin Method works by applying an external potential to balance CPD. The applied external voltage amount is equal to the work function or surface potentials of the sample.

The Kelvin Probe Microscopy is the combination of Kelvin Method and AFM. It has added features compared to AFM. Firstly, a signal generator applies an AC voltage that electrical signal is equivalent to the natural resonance frequency of the cantilever. However, as it does not in tapping AFM, the setup does not cause resonance of cantilever. When there is a potential difference between the AC voltage in the cantilever and DC voltage in the surface that is when surface potential or work function occurs, the vibration of the cantilever starts. The bias voltage is AC because this signal will allow the cantilever to resonate when there is a difference in potentials between a sample and a tip. Additionally, a null circuit in the KPFM system adjusts the AC voltage to minimize tip vibration allowing the operator to know the DC surface potential or work function in the sample. The AC voltage applied to tip is recorded as the image is being collected. The schematic diagram of KPFM is shown in Figure 3.6.

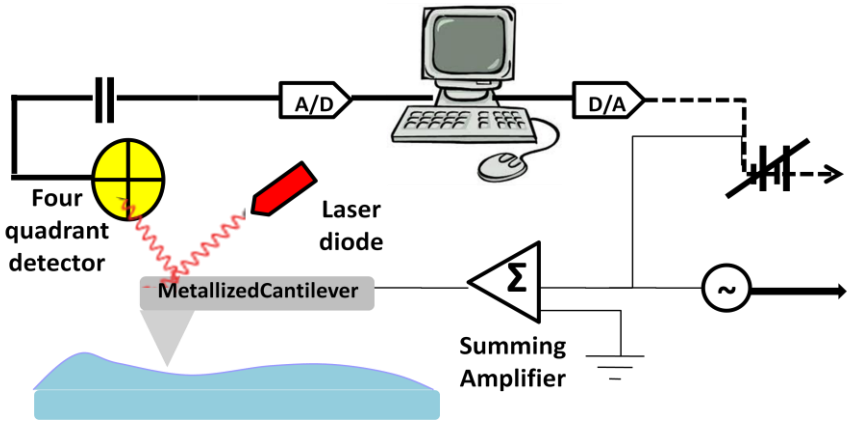

Figure 3.6. Measurement Circuit of the tip-sample interaction in KPFM.

During the operation a constant voltage U_0 and variable voltage $U_{\sim} = U_1 \sin(wt)$ are applied to the conductive tip. Thus, charges on the conductive sample creates potential distribution $\varphi(x, y)$. Then the applied net voltage between the conductive tip and the sample will be expressed as:

$$U = U_0 + U_1 \sin(wt) - \Delta\varphi(x, y) \tag{3.10}$$

The electrostatic force between the tip and the sample is the negative derivative of the applied voltage:

$$F = -\frac{1}{2}[U_0 - \varphi(x, y) + U_1 sinwt]^2 . \frac{\partial C}{\partial Z} \tag{3.11}$$

where U is the net applied voltage, C is the capacitance, and derivative is taken with respect to Z component. When equation (2.29) is rearranged, according to the harmonic frequency, three components occurred. A constant component:

$$F_{(w=0)} = -\frac{1}{2}\left\{[U_0 - \varphi(x, y)]^2 + \frac{1}{2}{U_1}^2\right\}\frac{\partial C}{\partial Z} \tag{3.12}$$

the component at frequency w:

$$F_{(w)} = -\{[U_0 - \varphi(x, y)]U_1 \sin(wt)\}\frac{\partial C}{\partial Z} \tag{3.13}$$

the component at frequency at $2w$:

$$F_{(2w)} = \left\{\frac{1}{4}{U_1}^2 \cos(2wt)\right\}\frac{\partial C}{\partial Z} \tag{3.14}$$

The constant component at first harmonic frequency (w) is the base of KPFM. When $F_{(w)}$ equals to the zero, applied DC voltage equals to the surface potential of the sample.

The major advantage of the KPFM is that it allows us to obtain surface potential maps on a small scale. The limits of resolution are currently similar to AFM, ~ 1 nm laterally and 0.1 mV. It must also be noted that, KPFM has inability to operate in biologically relevant conditions such as aqueous solutions.

3.4.4. X-ray Photoelectron Spectroscopy (XPS)

X-ray Photoelectron Spectroscopy (XPS) is a surface sensitive analytic tool that studies the empirical formula, chemical state and electronic state of the elements that exist within the material. XPS is based on the photoelectric effect, involving a photo-ionization process of inner shell electrons emitted from a surface excited by X-rays. Since the energy is conserved during the ionization process, as the kinetic energy (E_k) of emitted photoelectrons is measured, the binding energy (E_B) of the atomic orbital from which the electron originates can be given by:

$$E_B = h\nu - E_K - \Phi \tag{3.15}$$

where $h\nu$ is the energy of X-ray, and Φ is the work function of the spectrometer. The schematic setup of a typical XPS experiment is illustrated in Figure 3.7. X-rays are produced from an anode by bombardment of hot electrons that are created by a filament. Al (1486.6 eV) and Mg (1253.6 eV) are the most widely used anodes. The XPS technique is highly surface specific due to short range of the photoelectrons that are excited from the solid. The binding energy (BE) of these emitted photoelectrons can be determined using any appropriate electron energy analyzer and detector that give a spectrum with a series of photoelectron peaks. To determine the composition of the material's surface, the binding energy of the peaks can be used. Although XPS can provide chemical bonding information as well, it is not sensitive to hydrogen or helium as their binding energy is in the range of MeV.

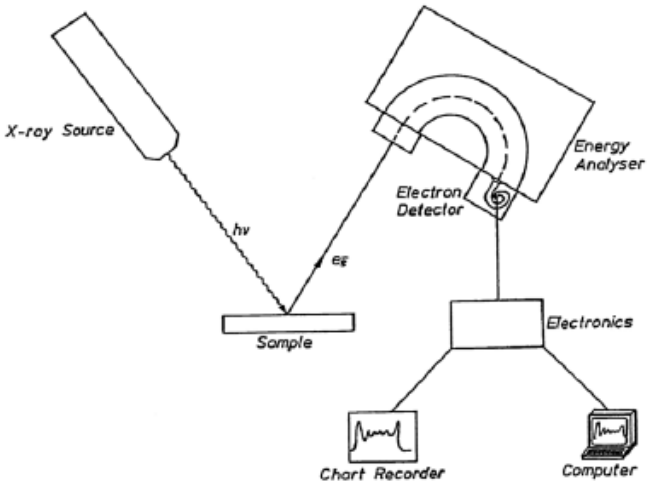

Figure 3.7. Schematic diagram of XPS system
(Source: (Feng 2008)).

XPS has been used extensively in thiol SAM characterization. Whether they are bound to surface, Hacker et al. determined the chemical environment of sulphur atoms using XPS (Hacker, et al. 2004). In the study of nanoscopic molecular junction incorporating a series of rigid thiol-terminated norbornylogs characterization made by Beebe et al. , sulphur exists in three different states: bound (BE~161.8 eV), unbound (BE~163.5 eV), and oxidized (BE~167.8 eV) (Beebe, et al. 2005). Additionally, measurements of self-assembled porphyrin monolayers' electronic spectrum showed a characteristic change with a signature in XPS (Li, et al. 1993). Also, Cavalleri and coworkers investigated the electronic states of L-cysteine (Cys) absorbed on gold as thiolate (Cavalleri, et al. 2004).

3.4.5. Cyclic Voltammetry (CV)

Cyclic Voltammetry (CV) has been widely used for the characterization of SAMs of simple thiol or MPc SAMs on gold electrodes. CV is a powerful used technique to study the electrochemistry on a surface. It can investigate the charge transfer process at the interface that is influenced by the nature of the electrode surface. With the comparison of the voltammogram SAM modified gold and unmodified substrate; it is possible to study the effect of the SAM in aqueous solutions (Finklea 1996, Kaifer, et al. 1999). SAMs are known to exhibit a blocking behavior towards a

number of Faradaic processes that can be easily exploited by using CV. Hence, by inhibiting the metal deposition on gold surface, SAMs can be blocked redox couples (Finklea 1996, Finklea 2000, Kaifer et al. 1999). In the study of Chidsey et al. this blocking behavior of SAMs is expressed by the dependency on the terminal functional groups (Chidsey, et al. 1990).

The Cyclic Voltammetry technique involves an applied external triangular voltage to the electrochemical cell, sweeping through a potential range and reversing the direction of the sweep in a cyclic fashion. The waveform excitation signal of Cyclic Voltammetry is shown in Figure 3.8. The resulting current (*I*) is obtained as a function of applied potential (*E*) to give the *I*-*E* curve which in this type of experiment is called a cyclic voltammogram.

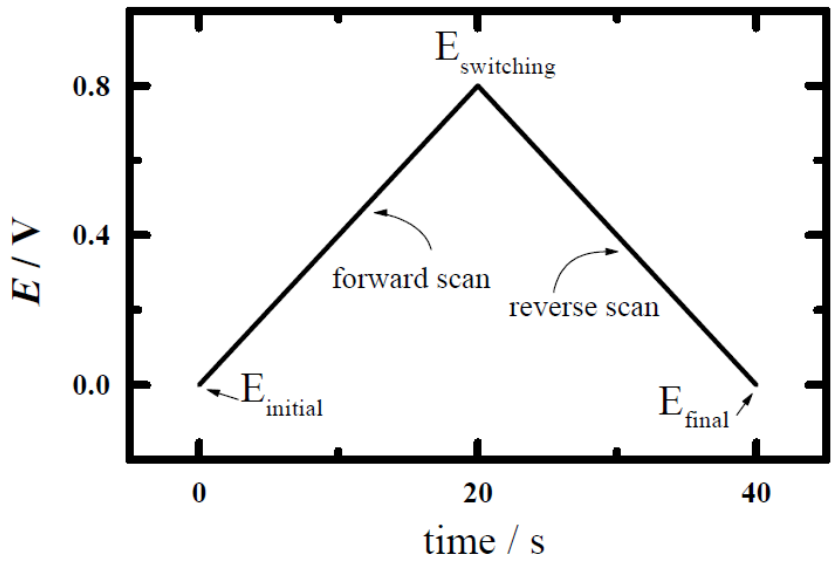

Figure 3.8. The Waveform Excitation Signal for Cyclic Voltammetry (Source: (Snook 2000)).

The system includes three electrodes: a working electrode, reference electrode and a counter electrode. The current flows between the working electrode and the counter electrode. It is important to ensure that no current will flow through the reference. The potential is controlled relative to the reference electrode which is placed as close to the working electrode as possible to reduce ohmic potential drop.

For the estimation of the surface coverage of the SAMs on gold surface, CV experiments can be used. In addition, after the surface concentration estimation, the

orientation of the organic film on gold electrode can be estimated. There are several methods which are used to calculate surface coverage of thin films such as the oxidative or reductive desorption method. The electrochemical desorption of thiol from gold results in either oxidative or reductive peak. The surface coverage of the SAM can be calculated using a theoretical relation:

$$\Gamma_{SAM} = \frac{Q}{nFA} \tag{3.16}$$

where Q is the charge under desorption peak, n is the number of electrons involved in the desorption of thiol, F is the Faraday constant (C mol^{-1}) and A is the geometric surface area of the gold electrode.

As a SAM characterization method, CV has many advantages based on its popularity and simplicity. Additionally, it can give very important information such as, integrity of SAMs, capacitive properties of SAMs, surface coverage and estimation of the orientation of the monolayer formed on gold surface. CV measurements provide the evidence of the modification of the surface and confirm the presence of the monolayer on electrode.

3.4.6. Ultraviolet-visible Absorption Spectroscopy (UV-Vis)

The onset of optical transitions across the fundamental band gap of the material leads to the adsorption process. Interband absorption is the excitations of the electrons between the bands of a solid by making optical transitions that are dictated by selection rules. In Figure 3.9. the Interband optical absorption process is illustrated.

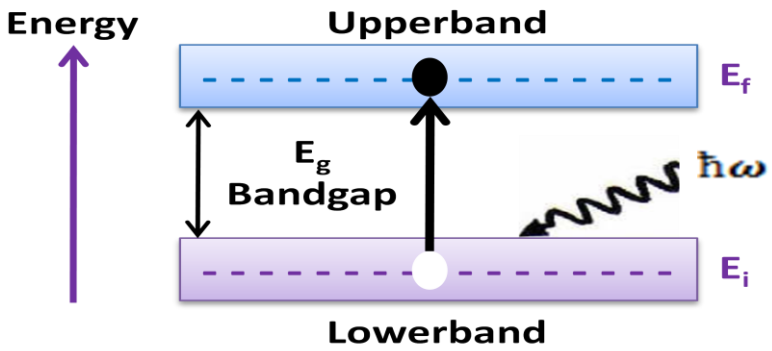

Figure 3.9. Interband optical absorption process.

An absorption spectrophotometer is an instrument that measures the amount of optical absorption, as a function of wavelength, in material. Spectrophotometer includes four components: (1) a light source which is usually a tungsten filament or gas-discharge lamp, (2) a monochromator; the broadband light that comes from the light source is used as input to the monochromator; tunable and highly monochromatic light is used as output. (3) a sample chamber is used to hold the sample under investigation and (4) a detector which measures the amount of light that passes through the sample. Typical detectors are either solid-state photodiodes, such as silicon or germanium, or photomultiplier tubes. The basic setup for measuring the absorption or transmission of light through a sample is shown in Figure 3.10. Incident light with the intensity of I_0 loses intensity upon passing through a sample with a thickness of t. The measured intensity after passing through the sample is I.

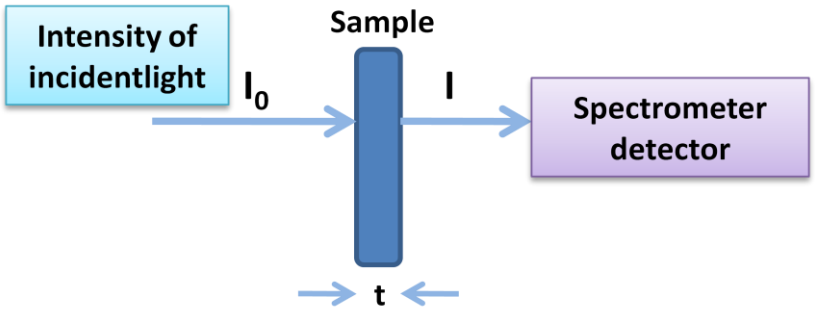

Figure 3.10. The basic setup for measuring the absorption or transmission of light through a sample.

When light of some wavelength λ with intensity I_0 is incident through the sample, due to absorption within the sample and reflection at the surfaces of the sample and the sample holder as well, the intensity of the light is reduced to a value I. Obtained I_0 and I can be used to determine the transmission of the sample at that wavelength.

Absorbance (A) is a dimensionless quantity which can be defined as the base-ten logarithm of transmission with the relation:

$$(T)A = -log_{10}T \tag{3.17}$$

Another quantity of interest is the absorption coefficient (α) which is given by Beer's Law:

$$I = I_0 e^{-\alpha t} \tag{3.18}$$

where t is the thickness in cm and α is in cm^{-1}. Absorption spectrometers measure the intensity of the transmitted light as a function of wavelength and compare it to the reference intensity at the same wavelength (Mark 2001). The schematic of double beam UV-Visible spectrometer is shown in Figure 3.11.

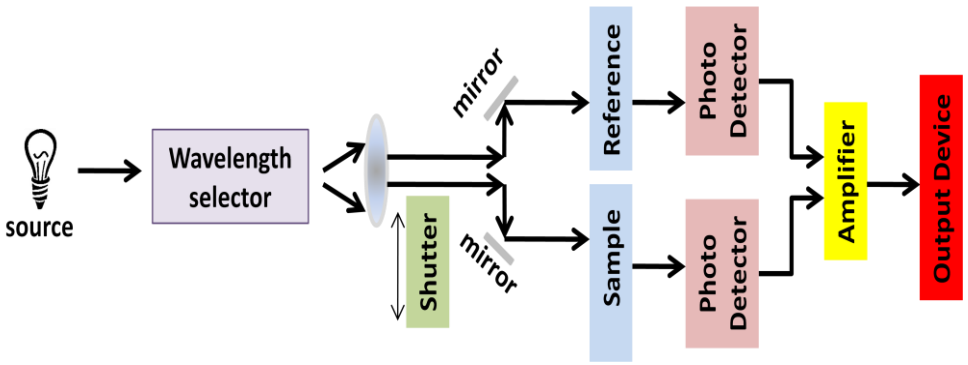

Figure 3.11. The schematic of double beam UV-Visible spectrometer.

3.5. SAM Applications

Self-assembled monolayers have many applications in different research areas such as organic chemistry, molecular electronics, biosensors, etc. A nonlinear optical material is the one in which interaction of light produces a new light at different frequency or phase. In addition to electron transfer through molecular assemblies, charge transfer excitation between the adjacent molecules is possible with the use of SAMs. As the molecules are anchored to the surface strongly, surfaces with desired chemical properties can be made and this application leads to the development of surfaces for sensor applications and specific catalytic processes. Due to a small change in mass would change the resonance frequency, molecular films have been used in piezoelectric devices. Therefore, such devices can be used as a gravimeter to determine the change in mass. Additionally, use of the monolayers as dielectric materials of molecular dimensions has challenging applications. When there is a dielectric layer in between the metal plates in air or vacuum, capacitance of the capacitor is greater. SAMs are used in the fabrication of devices such as metal-insulator semiconductor (MIS), metal-insulator-metal (MIM), superconductor-insulator-superconductor (SIS or Josephson junction) junctions and electroluminescence cells. In optical switching and photovoltaics, conduction through monolayers has interesting applications. On the mechanical front, SAMs can be used to reduce friction on solid surfaces such as in magnetic disks. Applications are also include the development of molecularly thin metal/oxide layers at surfaces. The 3D monolayers can be used as bulk materials. A polymeric metal clusters bounded by SAMs, are used in lasers, conducting coatings, catalysts, etc. In near future, new applications will be released with the growing chemistry and physics of these class materials.

CHAPTER 4

EXPERIMENTAL DETAILS

4.1. Chemical Compounds and Materials

ITO coated glass slides (from Sigma Aldrich) with a surface resistivity of 15-25 Ω/sq were used as the substrates. The chemicals used in cleaning process are acetone (CH_3COCH_3 - 99.8%, purchased from Merck), ethanol (C_2H_6O –99.8 %, purchased from Sigma Aldrich), and 2-propanol (CH_3CH (OH) CH_3 – 99.8%, purchased from Merck).

For thin film and device preparation, high purity materials were used. As active material, tris-(8-hydroxyquinoline) aluminum (Alq_3) with 99.995 % metal basis was purchased from Aldrich. Alq_3 is mostly used as emissive layer material in OLEDs. As hole transport layer materials, commercial *N,N′*-bis(3-methylphenyl)-*N,N′*-diphenylbenzidine (TPD – with 99% sublimed grade) and *N,N′-D*i-[(1-naphthyl)-*N,N′*-diphenyl]-1,1′-biphenyl)-4,4′-diamine (NPB – with 99% sublimed grade from Aldrich) have been used. In Figure 4.1. Chemical structure of Alq_3, TPD and NPB are shown.

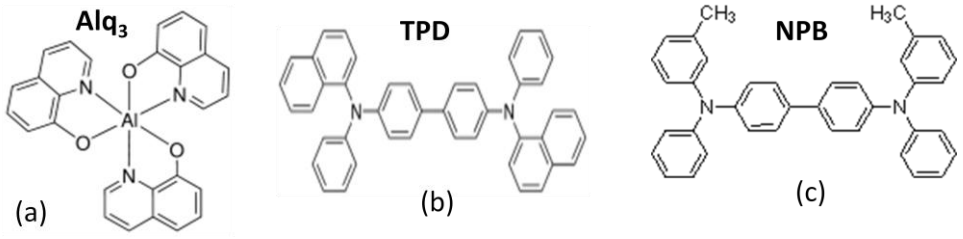

Figure 4.1. Chemical structures of (a) Alq_3, (b) TPD and (c) NPB.

In the fabrication of OLED devices, Al metal with a purity of 99% was used as cathode contact material.

In order to modify the ITO anode surface and to facilitate the hole injection, 4-[(3-methylphenyl)(phenyl)amino]benzoic acid (MPPBA) were synthesized by Dr. Şerafettin Demiç and his coworkers at Institute of Solar Energy in Ege University.

Into a solution of (3-methylphenyl)phenylamine (1.18 g, 6.44 mmol) and ethyl 4-iodobenzoate (1.97 g, 7 mmol) in acetamide (20 ml), K_2CO_3 (3.08 g, 22 mmol) and CuI (1.3 g, 7 mmol) were added in the given sequence. Then, while keeping the solution under a vigorous mixing, it was heated in oil bath to reach at 50 ^oC temperature. Once the temperature was reached, 18-Crown-6 (49 mg, 0.28 mmol) were added. Thereafter the temperature of oil bath was raised progressively until to reach 150 ^oC and the solution was stirred for 36 hours. At the end, the cooled solution was quenched by deionized water (50 ml) and concentrated under vacuum. The residue was purified by column chromatography (chloroform/hexane, 3:1) to produce ethyl 4-[(3-methylphenyl) phenylamino]benzoate (400 mg). To the solution of ethyl 4-[(3-methylphenyl)phenylamino]benzoate (370 mg, 1.14 mmol) dissolved in a mixture of THF (7 ml) and methanol (7 ml), an aqueous solution of NaOH (2 N, 15 ml) was added and the mixture was stirred at room temperature for 24 hours. Then the solution was concentrated under vacuum and the obtained crude material was directly used in the next step without purification. To obtain MPPBA, an aqueous solution of formic acid (0.1M, 7.8 ml) was added drop by drop to the solution of sodium 4-[(3-methylphenyl)phenylamino]benzoate dissolved in water (10 ml). Schematic representation of synthesis process of MPPBA molecule and its molecular structure is shown in Figure 4.2.

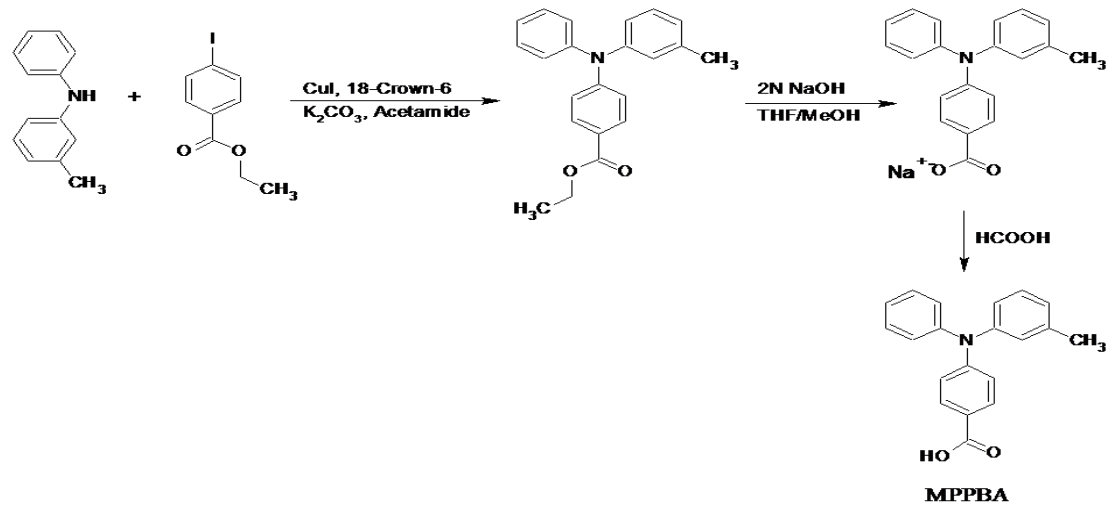

Figure 4.2. Schematic diagram of the synthesize process of MPPBA molecule.

The carboxylic acid based SAM molecules are anchored to ITO surface chemically to improve the surface properties. As seen from Figure 4.2., molecular structure of MPPBA contains methyl group on one of its phenyl groups. This group is useful in making more organized and well-ordered structure.

4.2. Sample Preparation

4.2.1. ITO Coated Glass Substrate Preparation

The ITO coated glass slides were etched using zinc powder and 20% HCl acid solution. This etching procedure leads to a noise free and uniform film surfaces and also prevents electrical shorting in the final device. Etched ITO substrates were placed in ultrasonic cleaner and purified in highly pure deionized water, acetone, ethanol, 2-propanol and again deionized water respectively for 15 minutes in each. After drying in N_2 stream, to clean the substrate surfaces from volatile species and organic molecules, oxygen plasma cleaning was treated for 15 minutes. In the system, plasma cleaning can be carried out using 14% O_2 and 86% Ar gas mixture. In Figure 4.3., a scheme of plasma cleaning and a picture of plasma etching in our system are shown.

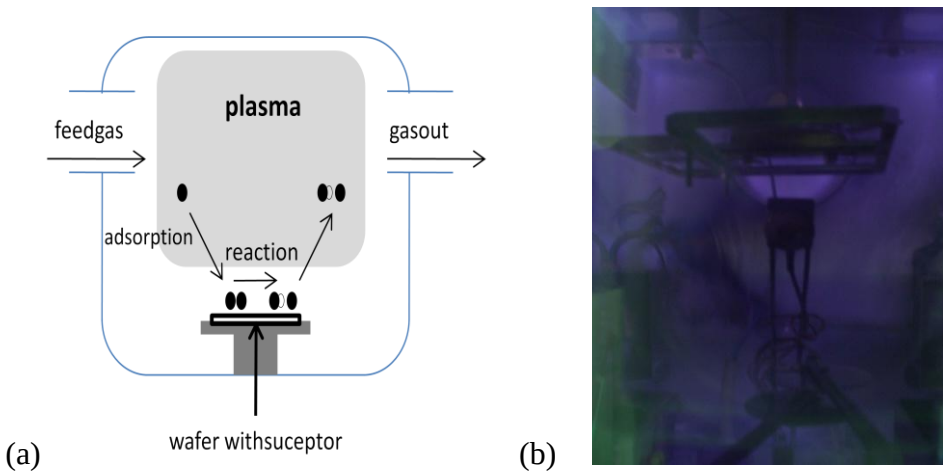

Figure 4.3. (a) A scheme of the plasma cleaning process and (b) a picture taken during plasma cleaning process in our system.

4.2.2. SAM Formation

Cleaned ITO substrates were immediately dipped into 1mM ethanol solution of MPPBA SAM molecule. Substrates were kept in this solution at room temperature for 48 hours. A chemical bounding was constituted on the hydroxyl-rich ITO surface from the carboxylic acid head group of MPPBA molecules. The substrates were then rinsed with ethanol to remove the residual MPPBA molecules from the ITO surface and finally SAM modified ITO glass substrates were dried in a stream of N_2 gas. The SAM formation process is illustrated in Figure 4.4.

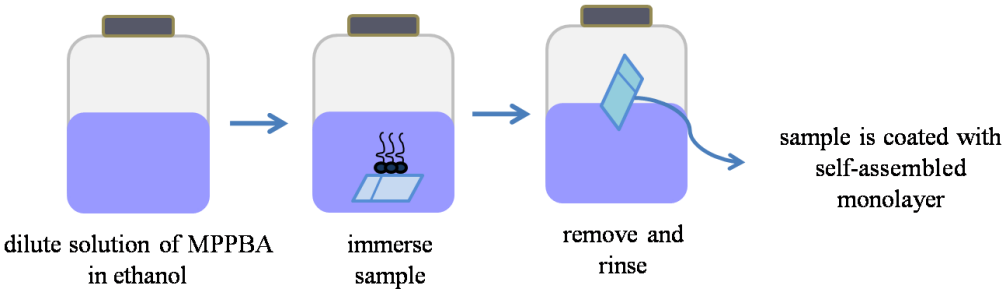

Figure 4.4. The self-assembly process

4.2.3. Deposition of Organic Layers

SAM modified ITO substrates were placed in organic evaporation system. TPD or NPB organic HTL materials deposited under high vacuum (~ 10^{-6} Torr). Similarly, as an ETL material Alq_3 is deposited under high vacuum. Layers with 50 nm (for HTL) and 40 nm (ETL) thickness were evaporated with low deposition rate (~ 0.5 Å/s). Organic evaporation system used in the deposition of organic layers is shown in Figure 4.5.

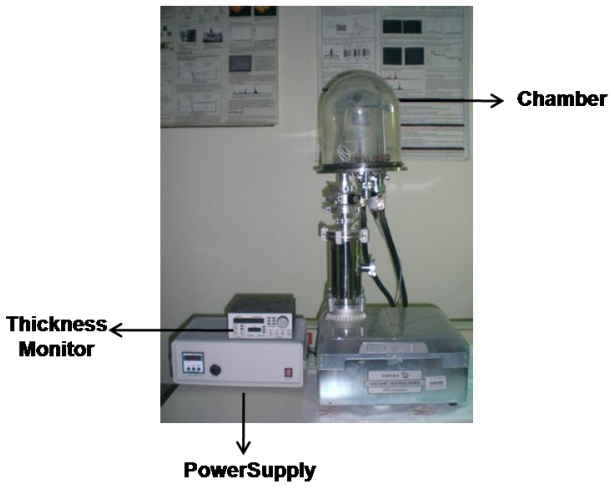

Figure 4.5. Evaporation system for deposition of organic layers.

4.2.4. Deposition of Cathode Layer

High purity Al (99%) was thermally evaporated to form the top contact cathode layer with a thickness of 120 nm at a pressure of 4×10^{-6} Torr and a deposition rate of 3 Å/s in evaporation system used during metal deposition. The photos taken from outside and inside of the metal evaporation system are shown in Figure 4.6.

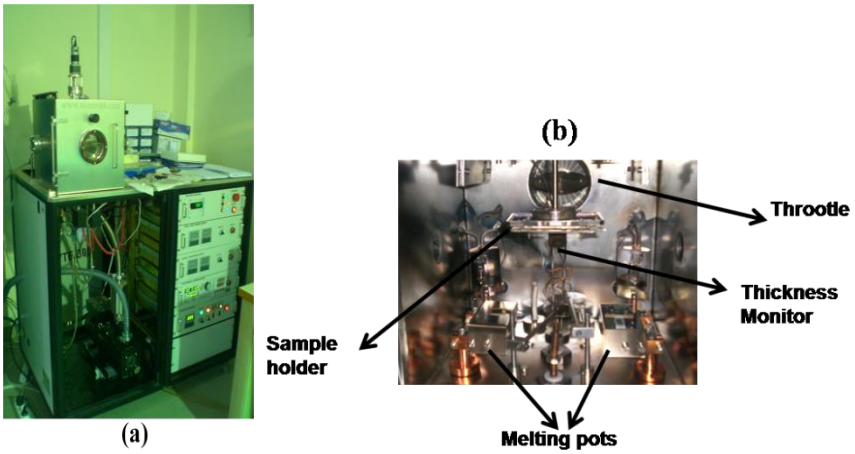

Figure 4.6. (a) Outside and (b) inside of metal evaporation system.

The mask used in Al evaporation and the top view of the final device is illustrated in Figure 4.7.

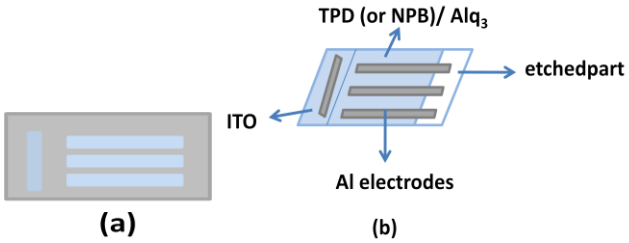

Figure 4.7. (a) The mask used in Al cathode deposition and (b) top view of the final device structure.

4.3. Characterization

4.3.1. Adsorption Kinetics of SAM Molecules

To indicate the adsorption kinetics of MPPBA molecules, delta frequency change caused by the formation of SAM on ITO coated gold quartz crystal was measured using Inficon Research Quartz Crystal Microbalance (RQCM). 5 MHz Ti/Au polished quartz crystals were purchased from Inficon.

Two types of measurements were recorded; with static solutions and with fluidic solutions. During the experiments prepared with static SAM solutions, 1 mM ethanolic MPPBA solution with 0.3 ml volume dropped over the ITO coated QCM crystal with the help of an injector and delta frequency change was recorded. To prevent any environmental effect, top of the QCM cell closed. In the fluidic experiments, 1mM MPPBA solution with the ratio of 0.2 μl/minute flowed through the silicon tubes with the help of peristaltic pump and the frequency change was recorded. The used QCM and peristaltic pump system is shown in Figure 4.8.

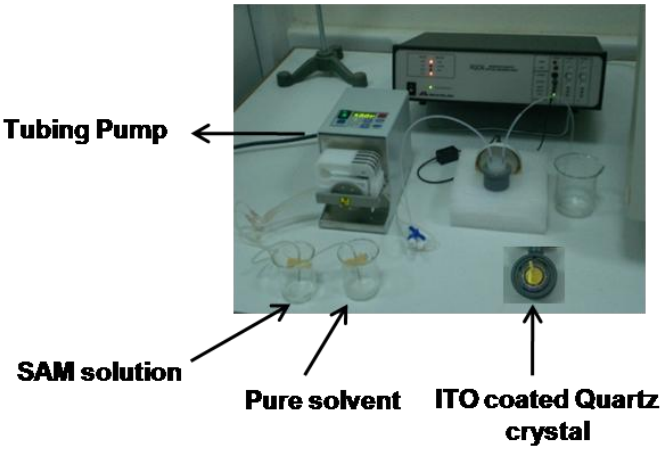

Figure 4.8. The Quartz Crystal Microbalance and peristaltic pump system.

4.3.2. AFM Surface Characterization (Topography and KPFM)

The surface morphology of the thin films was characterized by Solver Pro AFM from NTMDT (Russia). The topography and the phase contrast images of the samples were taken using NSG10 silicon tip with 30±5 μm cantilever width and typical 240 kHz resonant frequency. KPFM mode of the AFM with TiN conducting cantilevers were used to measure the change in the surface potential and work function before and after modification of ITO surface. The AFM system was placed on a vibration-free table to prevent environmental vibrations. Optic camera was used to project the image to the computer screen and therefore the tip position was determined accurately on the sample. AFM experimental setup is shown in Figure 4.9.

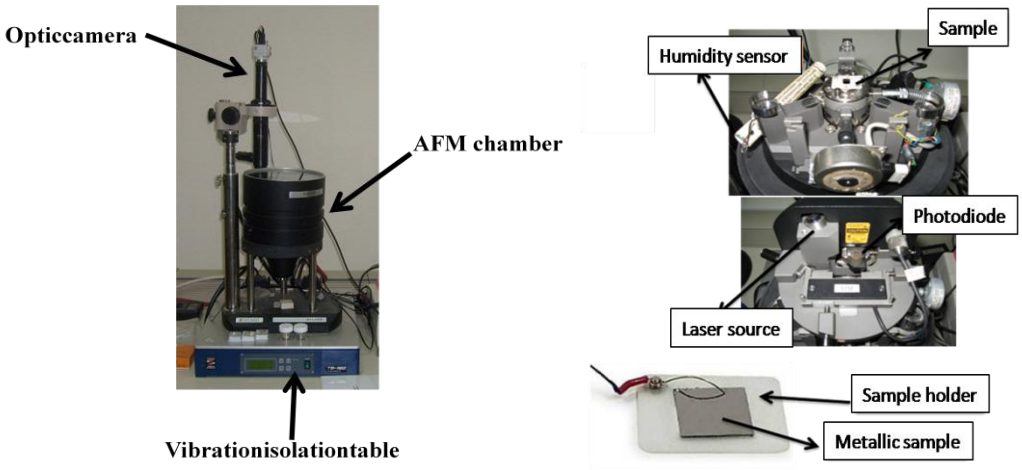

Figure 4.9. AFM and KPFM system.

To measure contact potential difference of the fabricated thin films, Solver P47H atomic force microscope (NT-MTD) (Moscow, Russia) operating in semicontact mode in air at room temperature was used. The tip side of the chip was Pt coated NSG01 silicon cantilevers (purchased from NT-MTD) with a 35nm nm tip curvature radius. The resonance frequency of the tips was between 120 and 190 kHz. The scan rate was kept constant at 1.01 Hertz during the operation. Two pass techniques were used in KPFM experiments. In the first pass, topography image was obtained using standard semicontact mode. And in the second pass, the probe was retracted from the surface in the taken topography and the surface potential image of the substrate was obtained.

4.3.3. X-Ray Photoelectron Spectroscopy (XPS)

XPS is also known as Electron Spectroscopy Chemical Analysis (ESCA). It is a very sensitive technique used for the chemical structure analysis of different surfaces. As mentioned before XPS is based on photoelectric effect. When X-ray is sent to film surface, the energy of core level electrons located at the orbitals rises up to the ionization energy level. Electron that is reached to ionization energy is called as photoelectron. With the calculation of the kinetic energy of photoelectrons that are detected by photoelectron spectroscopy, binding energy of the removed electrons from the surface can be obtained. Therefore, by using this technique elements found in a 1 to 10nm thick layer can be determined. For XPS technique Ultra high vacuum ($< 10^{-9}$ Torr) system is needed.

For XPS analysis of MPPBA molecules, Microphysics Lab XPS system in University of Illinois at Chicago (UIC) was used. The used XPS system is shown in Figure 4.10.

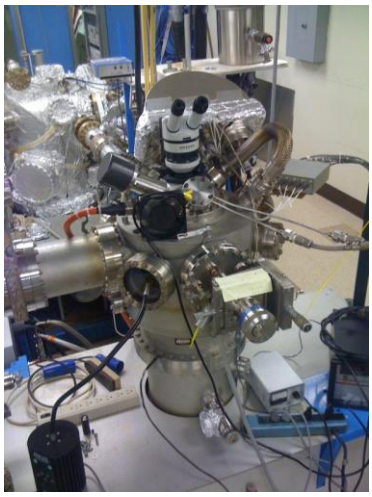

Figure 4.10. UI C Microphysics Lab XPS system.

4.3.4. Cyclic Voltammetry (CV)

As synthesized dyes, cyclic voltammograms of MPPBA molecules in solution and coated on ITO were obtained. As a working electrode Pt ring, as an auxiliary electrode PT wires and as a reference electrode Ag/AgCl were used. The scanning rate was 200 mV/s. Ferrocene (Fc) was the internal standard. CV measurements were recorded by CH660B model potentiostat from CH. Platinum wire (Pt), glassy carbon (GCE) and Ag/AgCl electrodes were used as counter electrode (CE), working electrode (WE) and reference electrode (RE), respectively. As supporting electrolyte 0.1 $MTBAPF_6$ in acetonitrile solution was used. Sweep rate was kept constant at 0.2 V/s. As internal reference ferrocene/ferrocenium couple was used.

4.3.5. Electrical Characterization (I-V)

The current – voltage characteristics of fabricated OLED devices were determined by using Keithley 236 Source Measure Unit. For investigating the electrical rectification characteristics, Keithley 2420 Source Meter, as shown in Figure 4.11., was used. For the transportation of the obtained data to the computer, GPIB data transfer cable was used.

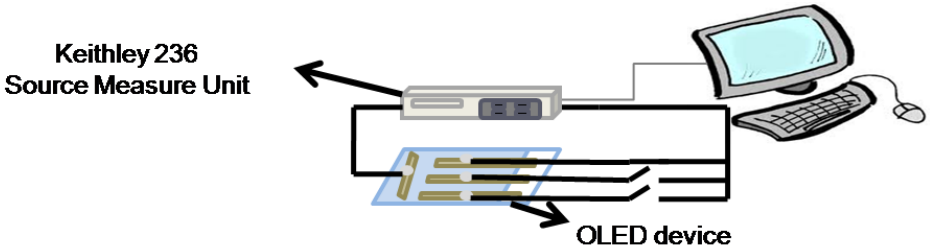

Figure 4.11. The Current-Voltage Measurement Setup.

CHAPTER 5

RESULTS AND DISCUSSION

5.1. Surface Characterization Results

5.1.1. Quartz Crystal Microbalance (QCM) Results

To investigate the SAM formation with quartz crystal microbalance (QCM) technique, during our experiments, dynamic and static SAM solutions were used. From the delta frequency change, the mass of the anchored MPPBA molecules are obtained. Two different types of experiment setups were used to evaluate SAM formation. One of them was carried on using MPPBA solution in flow and the other one was performed with the stand by MPPBA solution.

In Figure 5.1., the delta frequency change obtained with the fluidic MPPBA solution flow is shown. With MPPBA monolayer formation, significant negative frequency change in the negative interval is obtained.

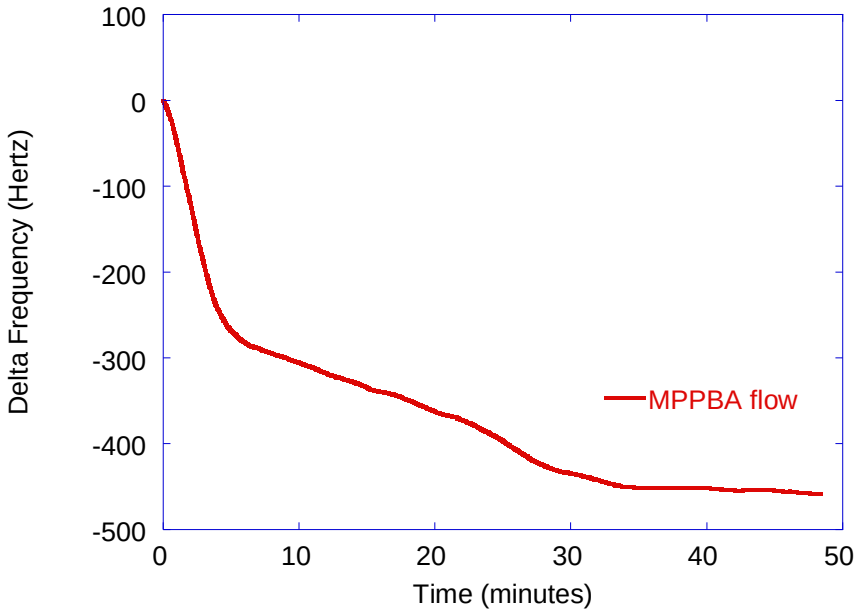

Figure 5.1. Delta frequency vs. time plot of fluidic MPPBA solution.

From the Sauerbrey relation, delta frequency change was used to obtain total mass change due to MPPBA monolayer. The calculated mass change versus time plot is shown in Figure 5.2. The mass values of the formed monolayer molecules increases up to 8 μgm/cm^2 in 35 minutes and then get stable. These results enforce the SAM formation on the ITO coated gold QCM crystal.

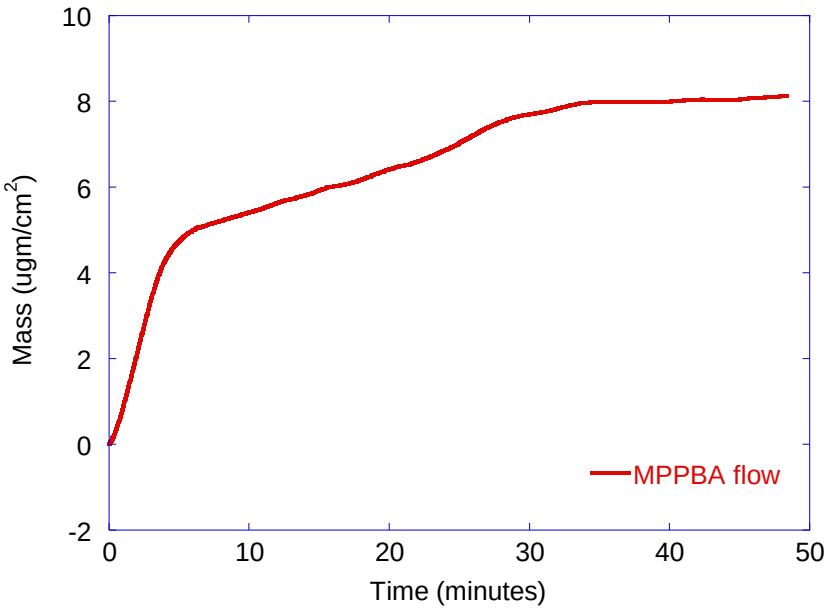

Figure 5.2. Mass change vs. time plot with the formation of SAM monolayer.

In normal conditions, for the completion of SAM formation on ITO surfaces, 48 hour is the ideal waiting time. However, in QCM experiments, especially in stand by solution experiments, after one hour later frequency signal breaks down because of the leakage. Therefore, we carried out the experiments until the signal breaks down. However, in the obtained delta frequency data, after the injection of the solution, no significant frequency change is observed that represents the SAM formation.

In Figure 5.3., the delta frequency change that is obtained by the static MPPBA SAM solution injection is shown. With the solution injection delta frequency decreases up to -400 Hertz rapidly and then crystal temporizes the environment and gets stable at -345 Hertz. The delta frequency stays constant for 40 minutes.

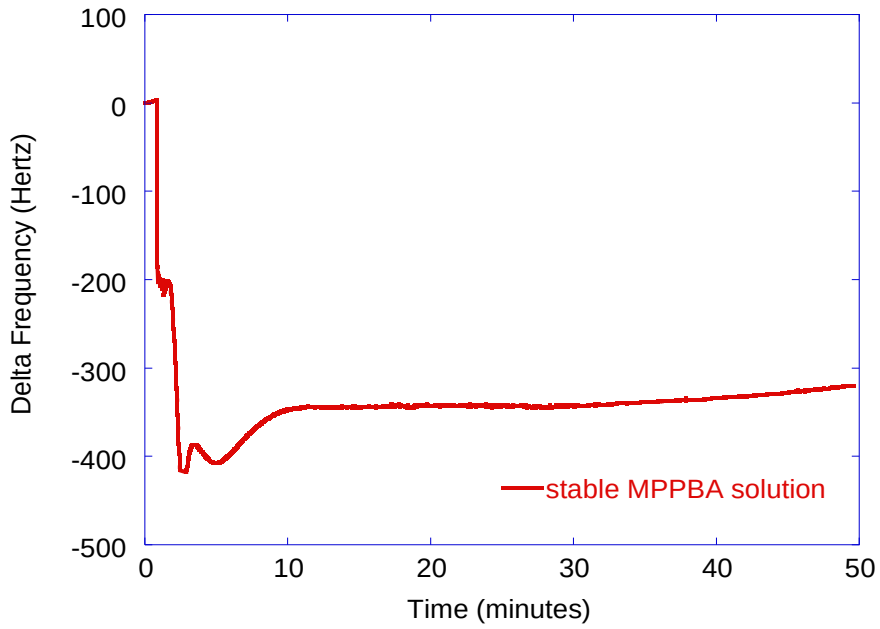

Figure 5.3. Delta frequency vs. time plot of static MPPBA solution.

The obtained mass change versus time graph is shown in Figure 5.4. The mass change gets stable at 6μgm/cm^2.

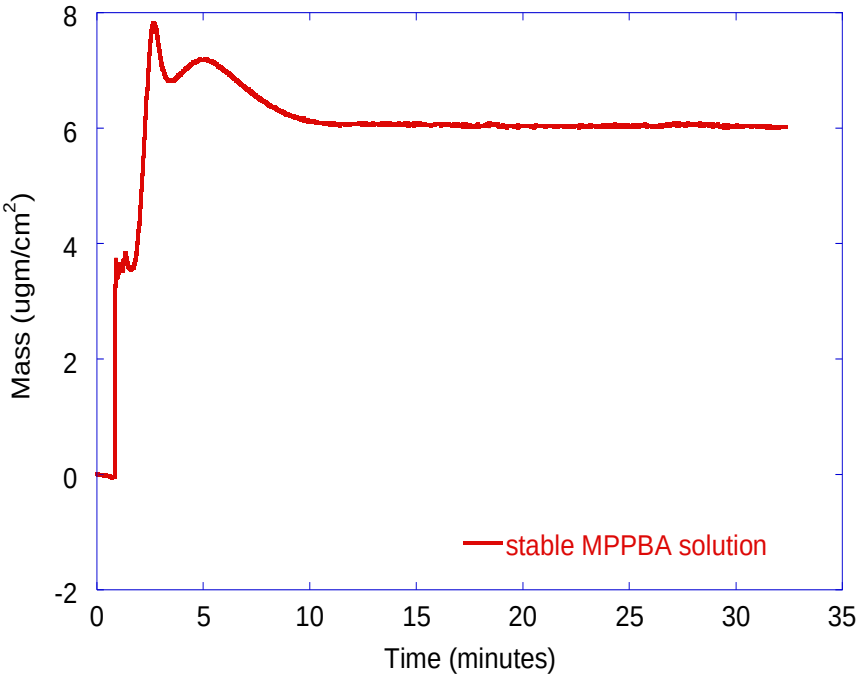

Figure 5.4. Mass change vs. time plot of stand by MPPBA SAM solution.

5.1.2. Atomic Force Microscopy (AFM) Results for Thin Films

For the surface investigation of surface morphology of the thin films, AFM images were recorded. To distinguish the surface morphology differences caused by SAM formation and HTL material deposition all AFM images for roughness analysis were taken for 4x4 μm^2 and 2x2 μm^2 scan areas.

Figure 5.5. shows the obtained surface topography and phase contrast images of bare ITO surfaces. As seen from the topography image ITO has rough surface. The measured surface roughness (rms) was found as 3.71 nm.

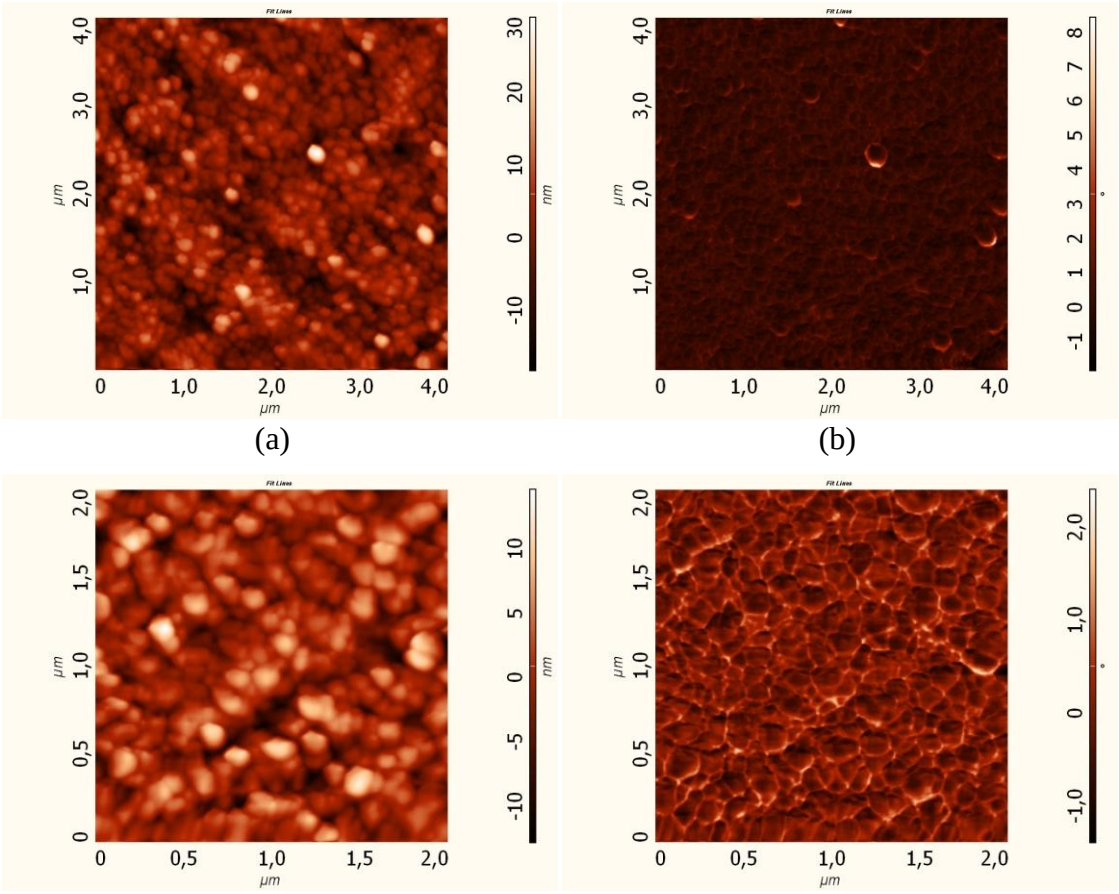

Figure 5.5. (a) Surface topography and (b) phase contrast image of bare ITO surface.

The surface topography and phase contrast images of MPPBA SAM modified ITO surfaces are shown in Figure 5.6. Island like structures can be seen with the SAM

formation and surface properties of the ITO surface has changed. The average roughness was measured as 3.41nm.

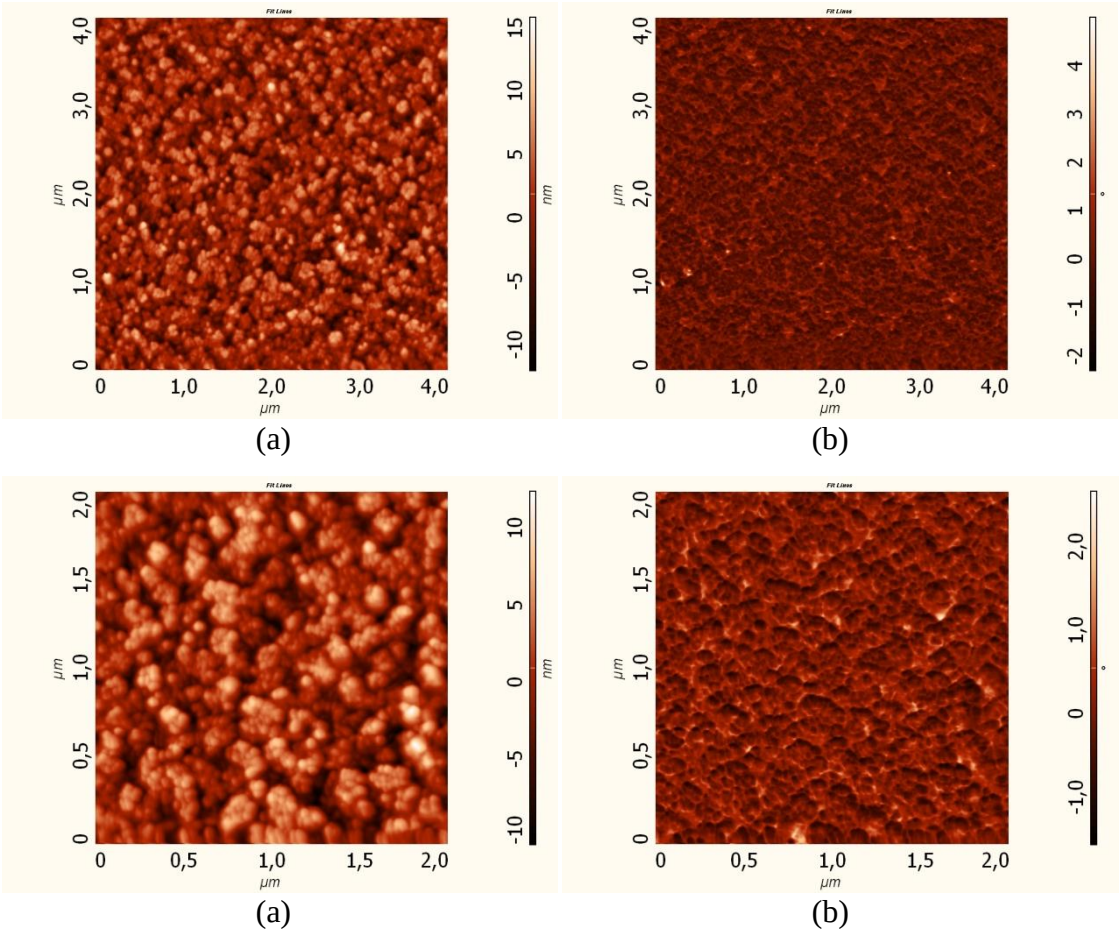

Figure 5.6. (a) Surface topography and (b) phase contrast image of MPPBA modified ITO surface.

In Figure 5.7., the surface topography and phase contrast images of TPD coated ITO surface are shown with 2 nm and 4 nm scan area. The ITO surface structure changed with the TPD deposition. The surface roughness was measured as 1.282 nm.

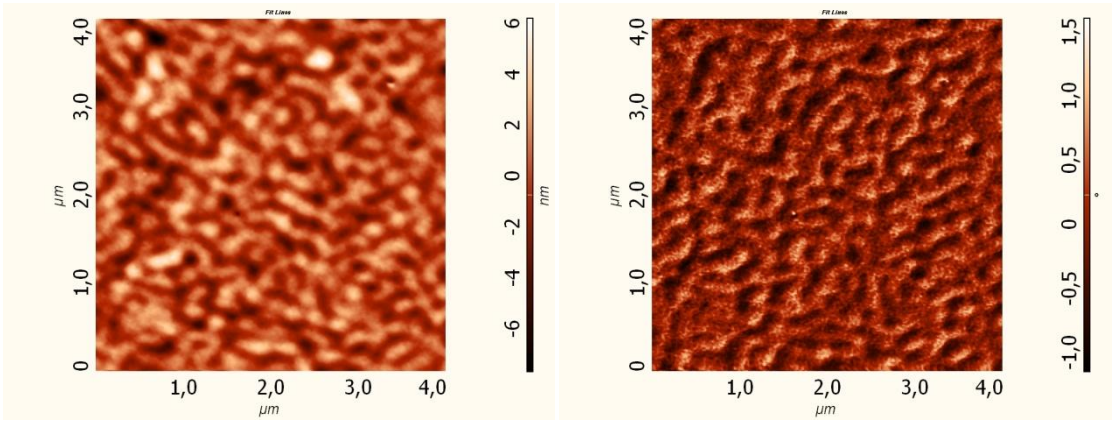

(a) (b)

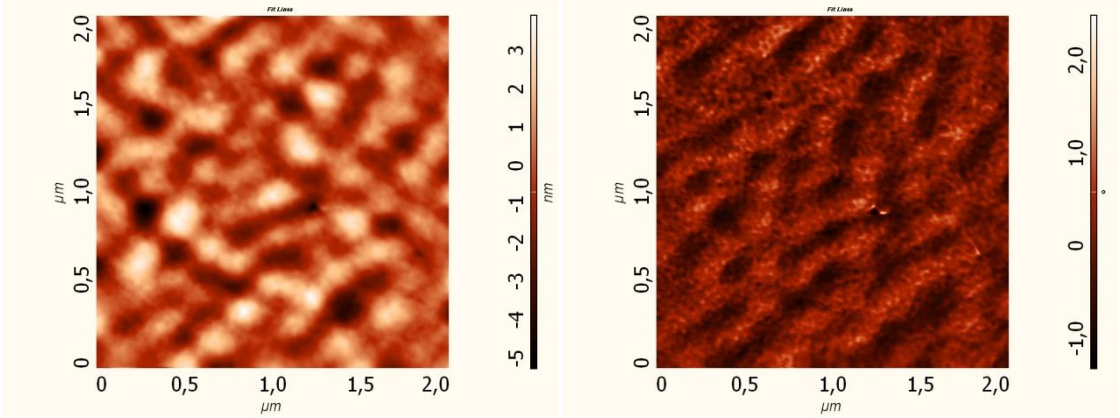

(a) (b)

Figure 5.7. (a) Surface topography and (b) phase contrast image of TPD coated ITO surface.

Figure 5.8. represents the surface topography and phase contrast images of TPD deposited on MPPBA modified ITO surface. The topography image looks like TPD coated ITO surface but small molecule structures are clear. The roughness of the surface is measured as 1.01 nm.

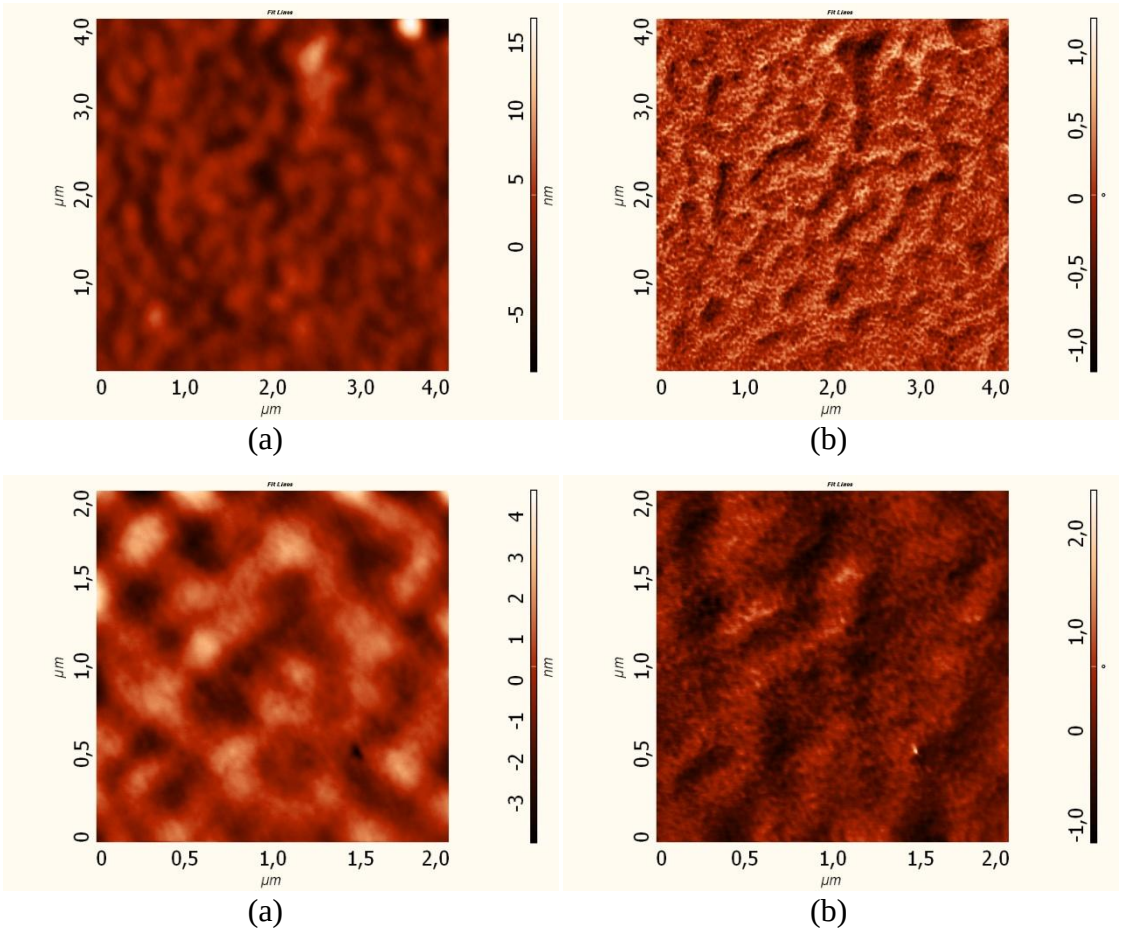

Figure 5.8. (a) Surface topography and (b) phase contrast image of MPPBA modified/TPD coated ITO surface.

The surface topography and the phase contrast images of NPB coated ITO surface are shown in Figure 5.9. The surface roughness is obtained as 2.22 nm. Therefore, NPB coated films have more rough structure than TPD coated films.

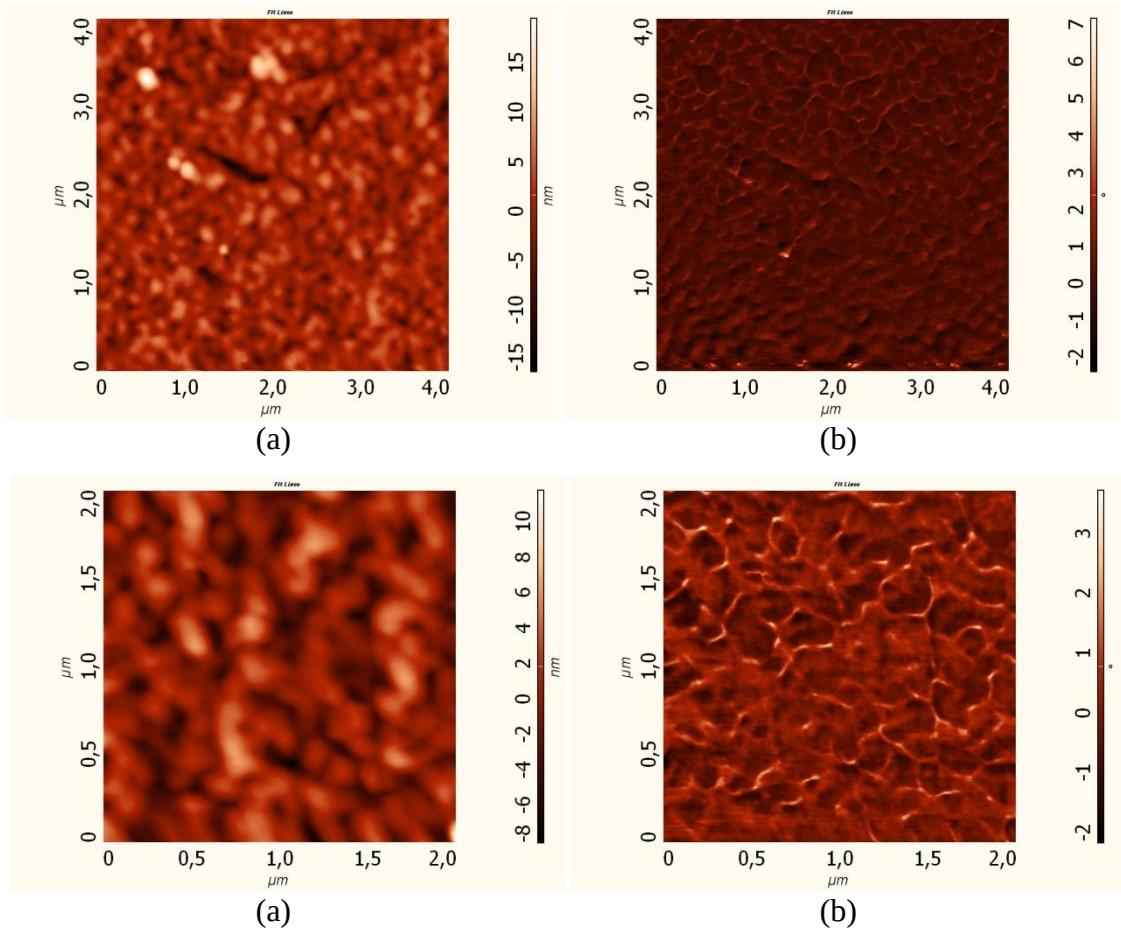

Figure 5.9. (a) Surface topography and (b) phase contrast image of NPB coated ITO surface.

Figure 5.10 shows the surface topography and phase contrast images of NPB coated on MPPBA modified ITO surface. The roughness of the films was measured as 1.92 nm.

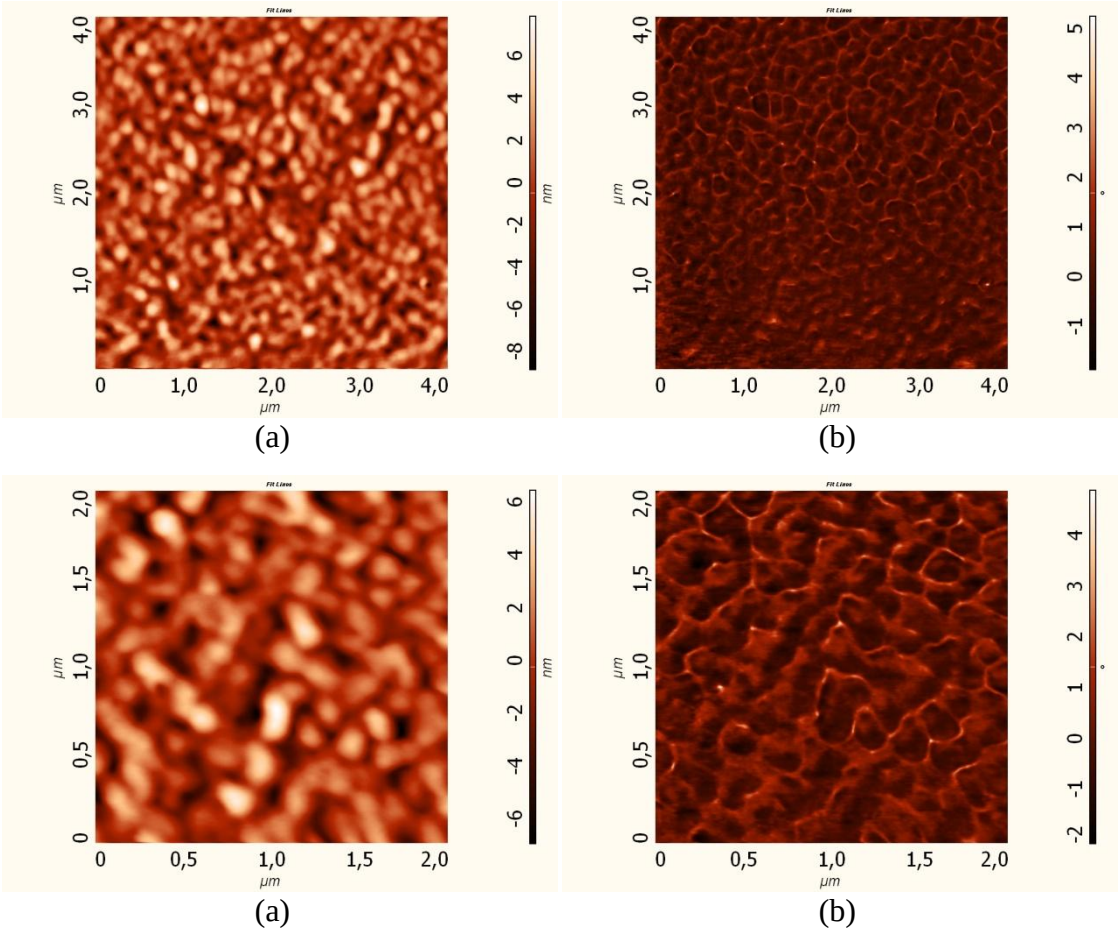

Figure 5.10. (a) Surface topography and (b) phase contrast image of MPPBA modified/NPB coated ITO surface.

Table 5.1. summarizes the measured surface roughness values of the fabricated thin films.

Table 5.1. Roughness values of fabricated thin films.

Thin Films	**Roughness (rms)**
Bare ITO	3.71 nm
ITO/MPPBA	3.41 nm
ITO/TPD	1.28 nm
ITO/MPPBA/TPD	1.01 nm
ITO/NPB	2.22 nm
ITO/MPPBA/NPB	1.92 nm

Bare ITO has rougher surface with surface roughness of 3.71 nm. With the MPPBA SAM modification, the roughness of the ITO surface decreases to 3.41 nm. TPD and NPB coated substrates have smoother surfaces with surface roughness of 1.28 nm and 2.22 nm, respectively. The final ITO/MPPBA/NPB and ITO/MPPBA/TPD devices' rms values decreased significantly. This might be related with the molecular size of the NPB molecules larger than TPD molecules, so that the rms values of NPB coated films are larger than TPD coated films.

5.1.3. Kelvin Probe Force Microscopy (KPFM) Results for Thin Films

KPFM technique was used to investigate the surface potential difference values of bare ITO; MPPBA modified ITO, TPD and NPB coated on MPPBA modified ITO surfaces.

In Figure 5.11., the surface topography and surface potential difference images of bare ITO surface are shown. The surface potential difference of bare ITO surface is measured as 0.066 V.

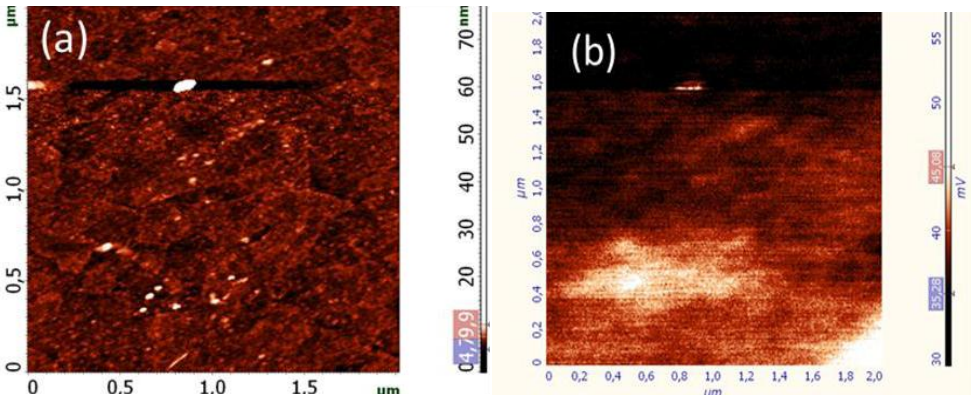

Figure 5.11. (a) Surface topography (b) Kelvin Probe Surface potential images of bare ITO surface.

The surface topography and surface potential difference images of MPPBA modified ITO surface is shown in Figure 5.12. The contact potential difference of the surface was measured as 0.286 Volt.

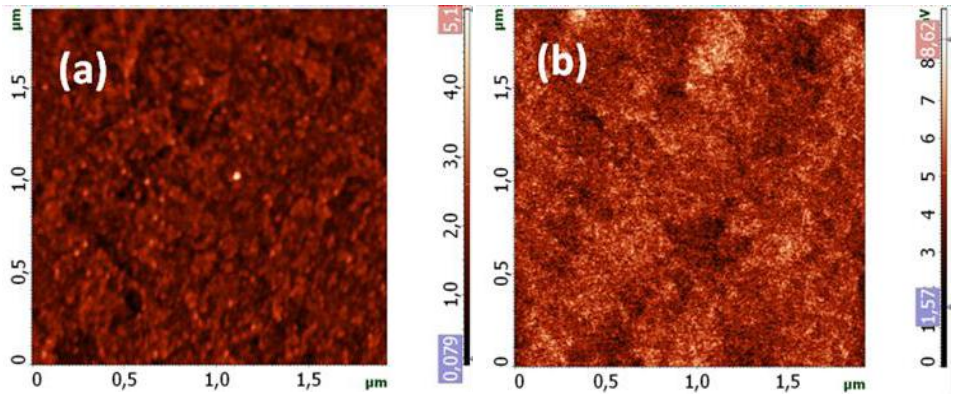

Figure 5.12. (a) Surface topography (b) Kelvin Probe Surface potential images of MPPBA modified ITO surface.

Figure 5.13. represents the surface topography and contact potential difference images of TPD coated over MPPBA modified ITO surface. The contact surface potential difference of the surface measured as 1.444 V.

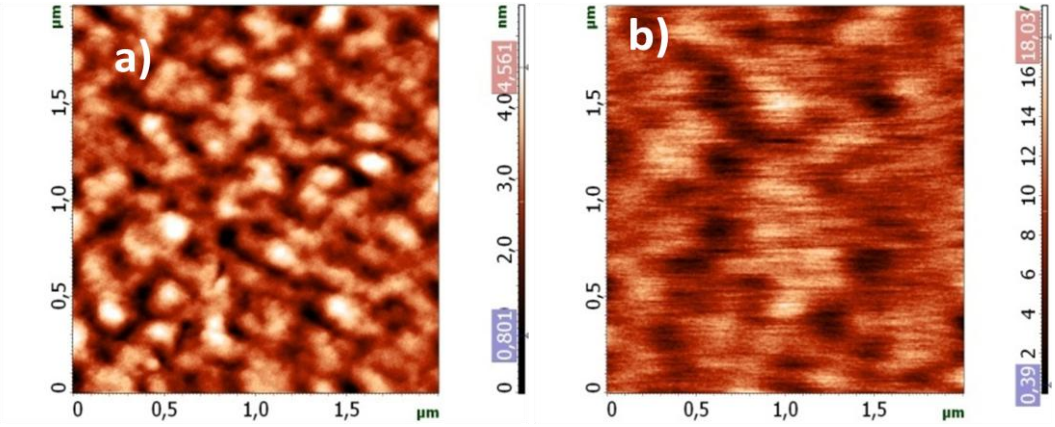

Figure 5.13. (a) Surface topography and (b) Kelvin Probe Surface potential images of MPPBA modified/TPD coated ITO surface.

Figure 5.14. shows the surface topography and contact potential difference images of NPB coated over MPPBA modified ITO surface.

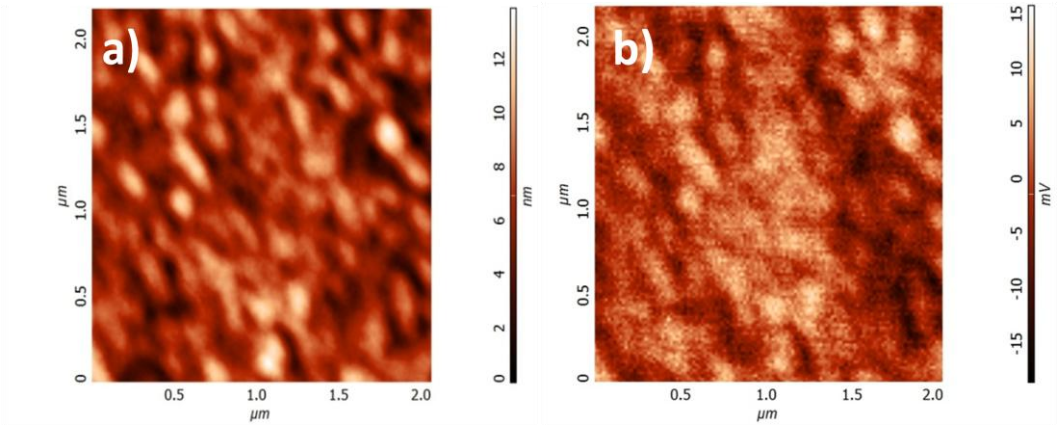

Figure 5.14. (a) Surface topography and (b) Kelvin Probe Surface potential images of MPPBA modified/NPB coated ITO surface.

The Kelvin Probe Surface potential current versus Bias Voltage plots of bare ITO and MPPBA modified ITO surfaces are shown in Figure 5.15. From the graph it is clear that SAM modification increases the surface potential and therefore improves the surface properties.

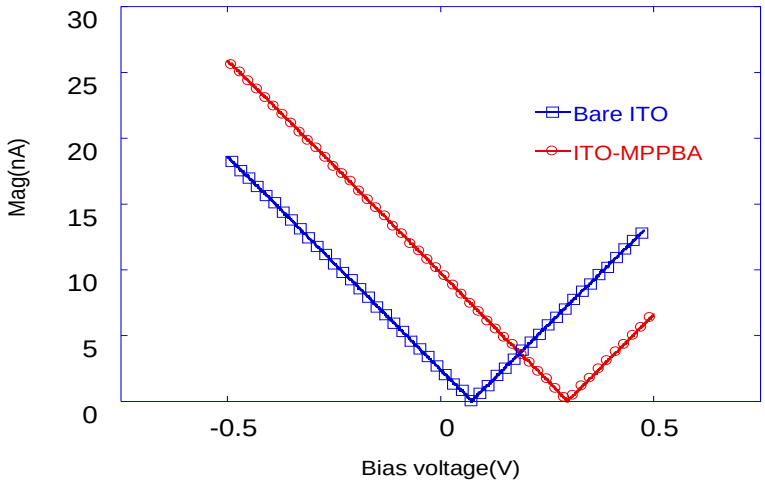

Figure 5.15. Kelvin Probe Surface Potential Current-Voltage Plot.

Surface potential and measured rms values of fabricated thin films are summarized in Table 5.2.

Table 5.2. Kelvin Probe Surface Potential values measured by KPFM Technique.

	Surface Potential (V)
Bare ITO	0.066
MPPBA modified ITO	0.286
MPPBA/TPD coated ITO	1.444

The results obtained by KPFM technique show the surface potential values are changed from 0.066 V to 0.286 V after the modification of ITO surface with MPPBA SAM molecules. These changes confirm the monolayer formation on ITO surface. Additionally, an increase in the surface contact potential also indicates the increase in the work function of the surface. Therefore, with the SAM modification, Fermi level of the ITO surface approaches to the HOMO level of the organic layer and thus the carrier injection improved with the decreasing threshold voltage.

5.1.4. X-ray Photoelectron Spectroscopy (XPS) Results

Investigation of the chemical structure of COOH-terminated MPPBA SAM molecules on the ITO substrate was made using X-ray photoelectron spectroscopy (XPS). Figure 5.16. shows an XPS survey spectrum of SAM-modified ITO surface after the modification process. The peaks, In $3d_{5/2}$, Sn $3d_{5/2}$, O 1s, N 1s and C 1s are seen in the spectra with binding energies 443.6, 485.6, 530.7, 398.4, and 284 eV, respectively. Indium (In) and stannum (Sn) peaks confirm the existence of the MPPBA molecules.

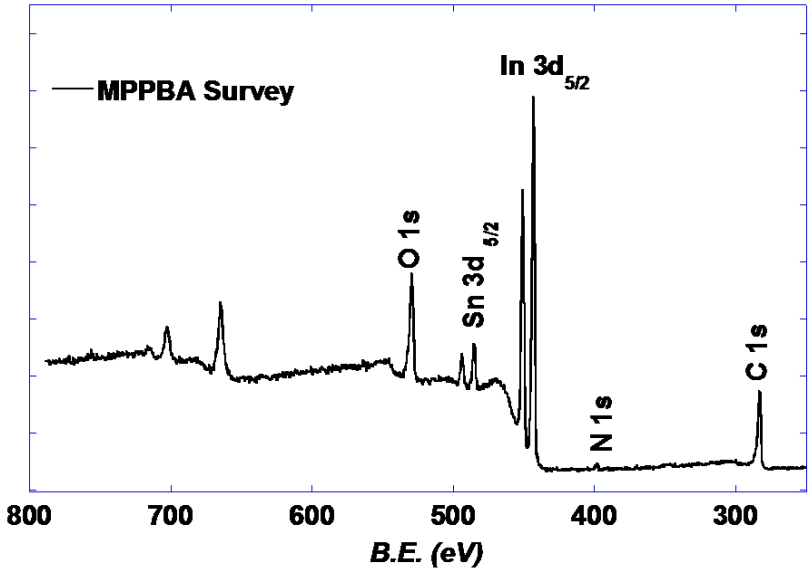

Figure 5.16. XPS survey spectrum of MPPBA modified ITO surface.

High resolution spectra of C 1s peak is shown in Figure 5.17. The C peak was fit with a background and mixed singlet peak. The peaks at positions 288.3, 285.6 and 284.6 eV are assigned to O–C=O, C−N or C−O and C−C, respectively. The peak at 288.3 eV indicates the covalent bonding of O–C=O. This bonding formed between COOH-terminated MPPBA molecule and hydroxyl groups of the ITO surface. Additionally, this peak is attributed to carbon of carboxyl group in the formulated molecule. In order to explain the origin of the peaks in C 1s spectra, one should consider the C 1s spectra in organic compounds. Similar chemical shifts can be found for C 1s in a wide range of organic compound models (Clark, et al. 1976, Moussaif, et al. 2000).

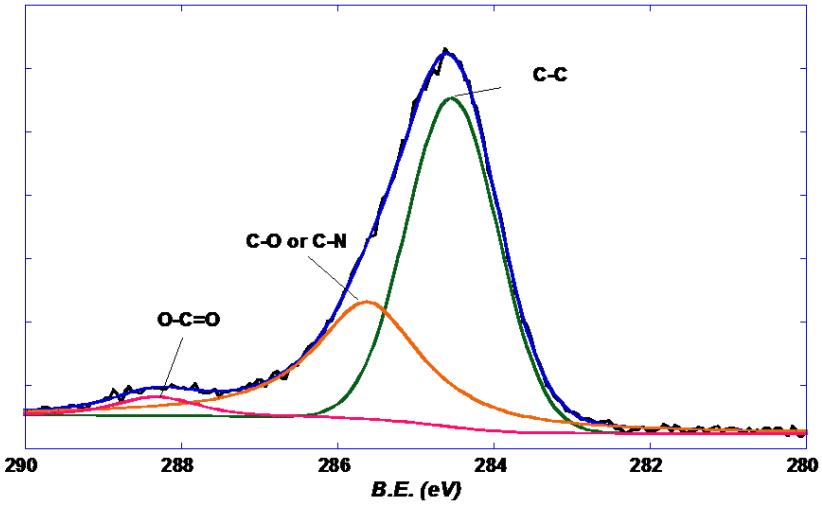

Figure 5.17. XPS C 1s spectrum of MPPBA.

A fitted Oxygen 1s spectrum is shown in Figure 5.17. Peaks at 529.9, 531.1 and 533.6 eV are assigned to O^{2-}, carbonyl group (C=O), and (C–O) or (Sn–O), respectively (Binkauskiene, et al. 2010, Montagne, et al. 2008, Zeng, et al. 2002). Low binding energy O 1s component at 529.9 eV is attributed to oxygen in the form of oxide, O^{2-} on ITO (Binkauskiene et al. 2010, Yan, et al. 2000). Carbonyl group (C=O) was found to be the strongest peak.

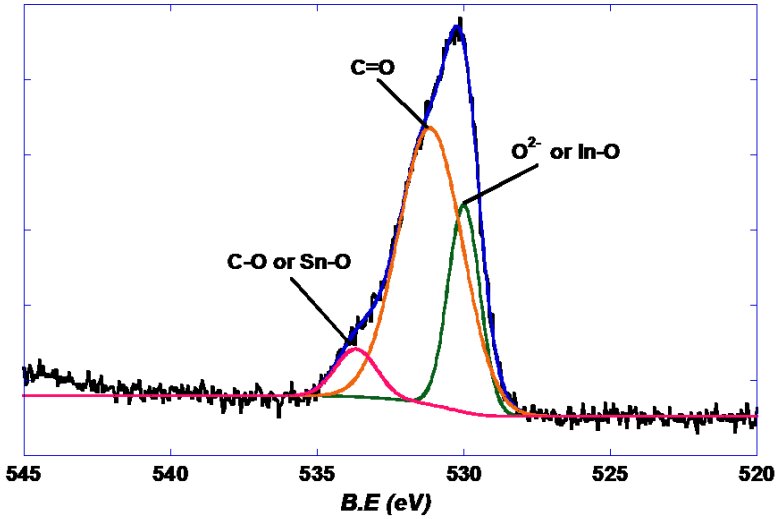

Figure 5.18. XPS O 1s spectrum of MPPBA.

5.1.5. Cyclic Voltammetry (CV) Results

Electrochemistry of MPPBA coated on ITO was studied by Cyclic Voltammetry (CV). MPPBA molecules showed one reversible oxidation peak at 1.26 V in solution. On the other hand, on ITO surface the oxidation peak was obtained at 1.15 V. This slight shift toward more negative potential region can be attributed to the carbonyl group that anchored to ITO surface. Electron affinity of carbonyl group decreases by this binding and leads to decrease in oxidation potential compared to solution phase. However, oxidation peak on ITO surface was observed to be quassi-reversible most probably due to the formation unstable oxidized species of monolayer on ITO surface.

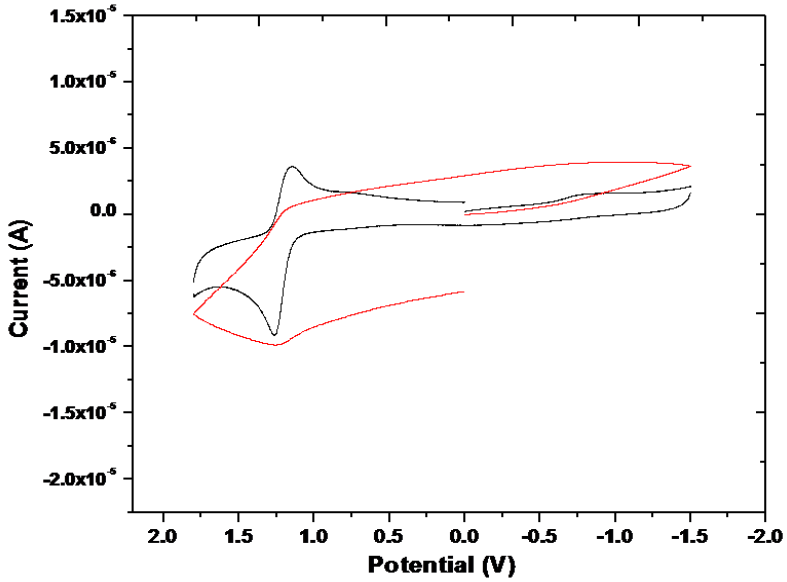

Figure 5.19. Cyclic voltammograms of the MPPBA (in solution) and MPPBA coated on ITO surface.

It must be noticed that HOMO level of MPPBA was calculated from the onset oxidation potential that is determined from the intersection of two tangents drawn from rising oxidation current and background current in the cyclic voltammogram. The onset of the oxidation was calculated to be 1.1 V in solution, while it was 0.99 V on ITO surface. While HOMO level of MPPBA in solution was calculated as -5.51 eV, the HOMO level of MPPBA on ITO surface was calculated as -5.4 eV. This situation may be attributed to decrease in surface potential of ITO with the SAM formation.

5.1.6. Ultraviolet-Visible Spectroscopy (UV-Vis) Results

Analiytic Jena S 600 UV spectrophotometer was used to investigate the photo physical and photochemical properties of synthesized MPPBA molecules. In Figure 5.20. the UV spectrum of MPPBA coated ITO surface is shown. Between 350-550 nm, there is a distinct absorption peak that represents the chemical structure of the MPPBA molecule.

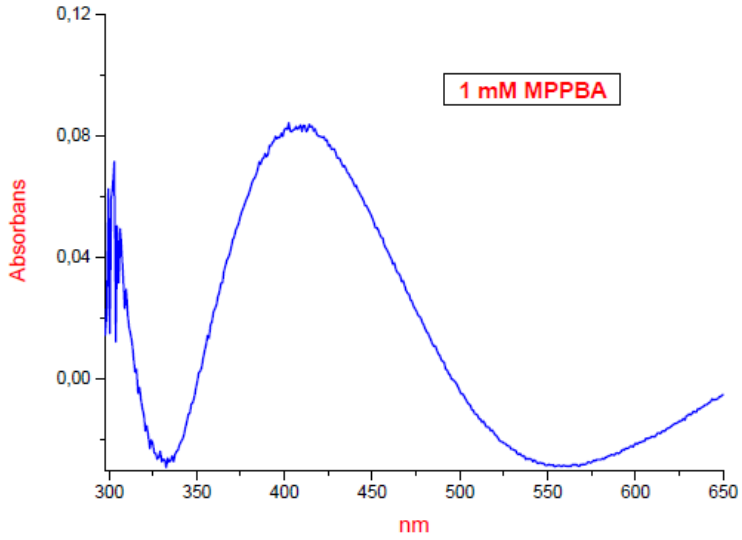

Figure 5.20. UV spectrum of MPPBA coated ITO substrate.

5.2. Electrical Characterization Results of Organic Diodes

5.2.1. Electrical Rectification Characteristics

5.2.1.1. Schottky Thermal Injection Results

Schottky characteristics of the devices were investigated to calculate barrier height after the surface modification with SAM molecules and HTL materials. As the work function and barrier height values of the fabricated devices are close to each other, plots are obtained symmetric at negative and positive applied voltage intervals.

I-V characteristics of fabricated ITO/MPPBA/Al, ITO/MPPBA/NPB/Al and ITO/NPB/Al are shown in Figure 5.21. SAM modification reduces the difference between the bare ITO and NPB coated ITO in current-voltage plots.

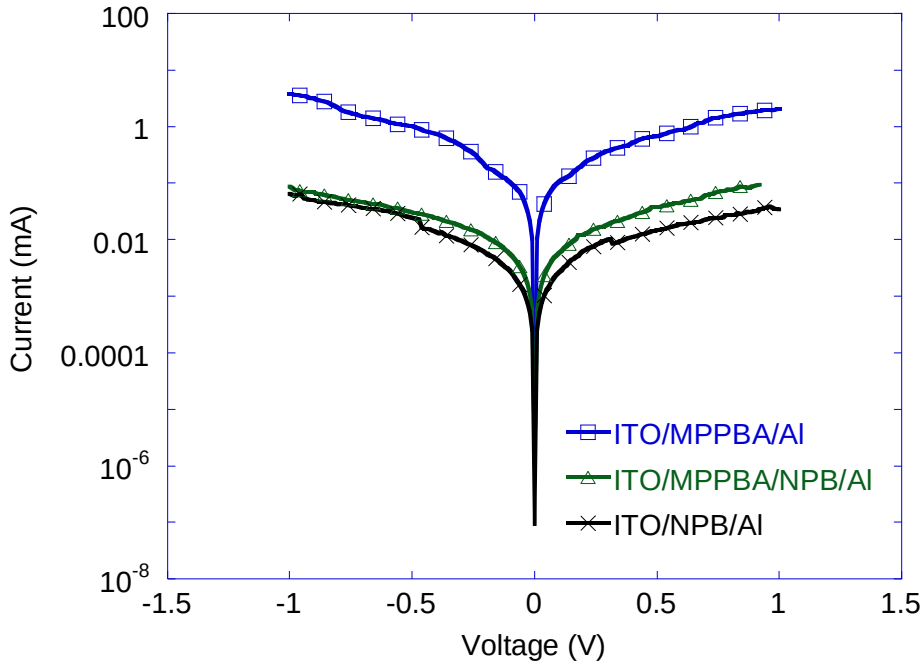

Figure 5.21. I-V characteristics of fabricated ITO/MPPBA/Al, ITO/MPPBA/NPB/Al and ITO/NPB/Al devices.

The calculated ideality factor and barrier height values using Cheung relation is presented in Table 5.3. The ideality factor results vary at different devices. There can be some practical problems when measuring ideality factors. For example, at low voltages the shunt resistance (R_s) dominates the device performance and causes a large peak. It is usually not possible in practice to correct for the effects of R_S. Additionally, the ideality factor comes from the differential of a signal that is very prone to noise. On the other hand, barrier height values indicate that value of the bare ITO is low and the barrier height of NPB coated ITO is high. With the MPPBA modification, the barrier heights of the devices get closer. Therefore, the injection of the holes into organic NPB hole transport layer becomes easier and thus the device performance is improved.

Table 5.3. Calculated ideality factor and barrier height values of devices with NPB organic layer.

	ideality factor (n)	**barrier height (Φ_B) (eV)**
ITO/MPPBA/NPB/Al	2.28	0.503
ITO/NPB/Al	0.41	0.618

The Schottky characteristics of fabricated ITO/MPPBA/TPD/Al and ITO/TPD/Al are shown in Figure 5.22. The surface modification made with MPPBA SAM molecules reduces the conduction difference between ITO/AL and ITO/TPD/Al devices.

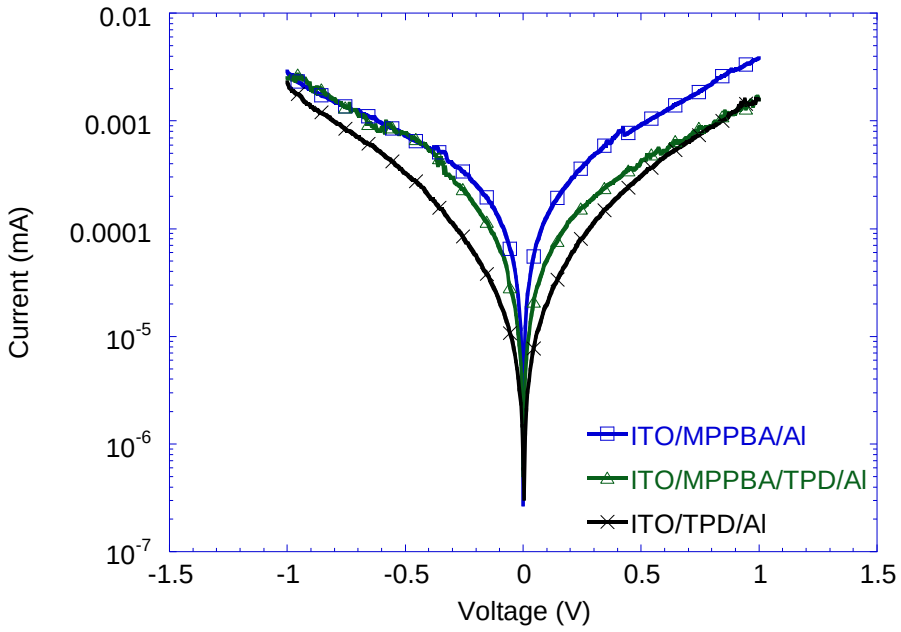

Figure 5.22. I-V characteristics of fabricated ITO/MPPBA/Al, ITO/MPPBA/TPD/Al and ITO/TPD/Al devices.

The calculated ideality factor and barrier height values from I-V plot are shown in Table 5.4. The barrier height between the ITO/Al and ITO/TPD/Al is minimized with the MPPBA SAM modification. Like the devices prepared with SAM and NPB, the transportation of the holes into organic TPD hole transport layer becomes easier and thus the device efficiency increased.

Table 5.4. Calculated ideality factor and barrier height values of devices with TPD organic layer.

	ideality factor (n)	**barrier height (Φ_B) (eV)**
ITO/MPPBA/TPD/Al	4.64	0.508
ITO/TPD/Al	4.36	0.513

To investigate the variations caused by MPPBA molecules in different structures, MPPBA modified n and p-type silicon substrates were used. In Figure 5.23. the current-voltage relation of bare n-type silicon and MPPBA modified n-type silicon is shown. In the reverse bias region, the conduction of the bare n-type silicon is better than SAM modified one. On the other hand, under forward bias, the conduction in MPPBA modified silicon is more efficient than the bare silicon. This observation indicates that the use of SAM molecules can improve the surface properties of the substrate. There is a little shift from the zero point of x-axis in bare n-type silicon. In our experiments with silicon substrates we observed that the light in the environment of the experiment setup affects the measurement results and thus this shifting can be caused by the background light in the room.

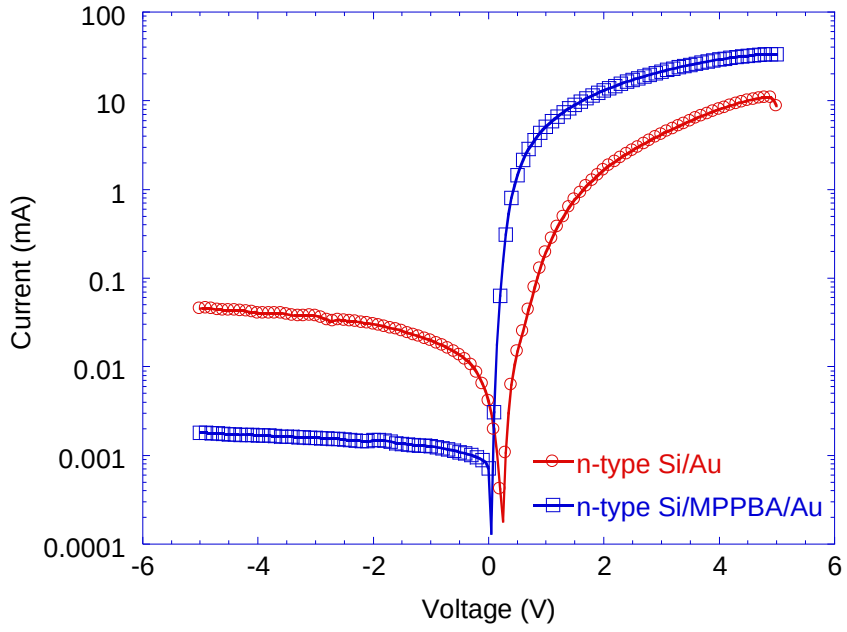

Figure 5.23. Current-Voltage behavior of bare n-type silicon and MPPBA modified n-type silicon.

The current-voltage behavior of bare p- and n-type silicon is shown in Figure 5.23. Again a shifting in x-axis caused by the light of environment is seen. MPPBA modified p-type silicon device has better rectification behavior than bare p-type device in the both reverse bias and forward bias region.

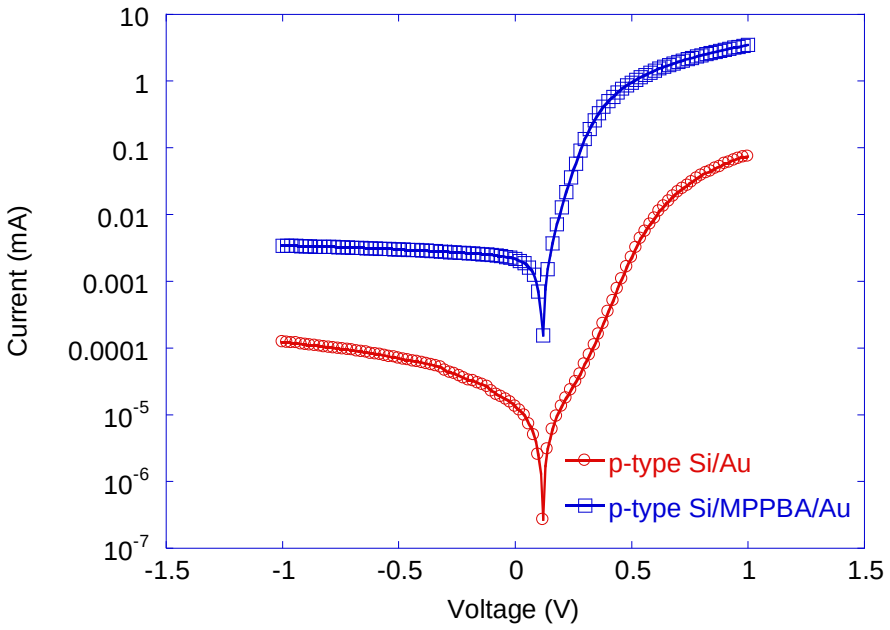

Figure 5.24. The Current-Voltage behavior of bare p-type silicon and MPPBA modified p-type silicon devices.

The calculated ideality factor and barrier height values of untreated n- and p-type devices and MPPBA modified n- and p-type devices are shown in Table 5.5. It is obvious from the barrier height values, that SAM modification of the silicon substrates alters the surface properties.

Table 5.5. The calculated ideality factor and barrier height values of bare and MPPBA modified n-type and p-type silicon devices.

	ideality factor (n)	**barrier height (Φ_B) (eV)**
Bare nSi/Au	1.00	0.670
nSi/MPPBA/Au	2.70	0.362
Bare pSi/Au	3.38	0.531
pSi/1 mM MPPBA/Au	2.48	0.594

5.2.1.2. Space Charge Limited Current Results

To evaluate the carrier mobility under steady state current in an organic semiconductor, space-charge-limited current (SCLC) measurements were done up to 10 V.

In Figure 5.25., the current-voltage behavior of ITO/NPB/Al device is shown. There is a significant increase in the forward bias region.

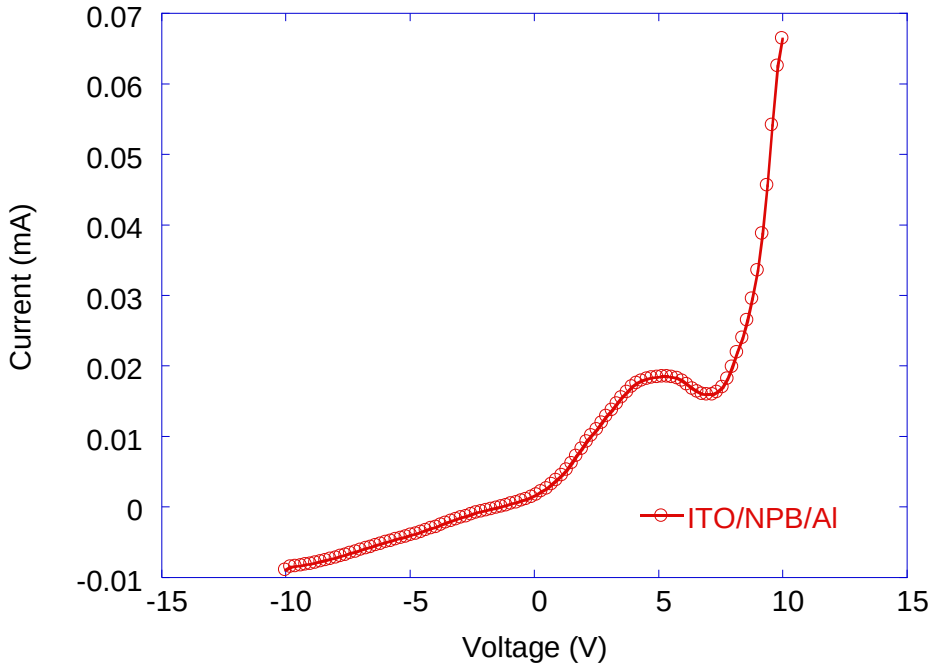

Figure 5.25 . The Current-Voltage behavior ITO/NPB/Al between -10 and 10 V region.

The current-voltage characteristic of ITO/MPPBA/NPB/Al device is shown in Figure 5.26. It has better rectification behavior than ITO/NPB/Al in forward bias region. The current value reached to 110 mA at 10V.

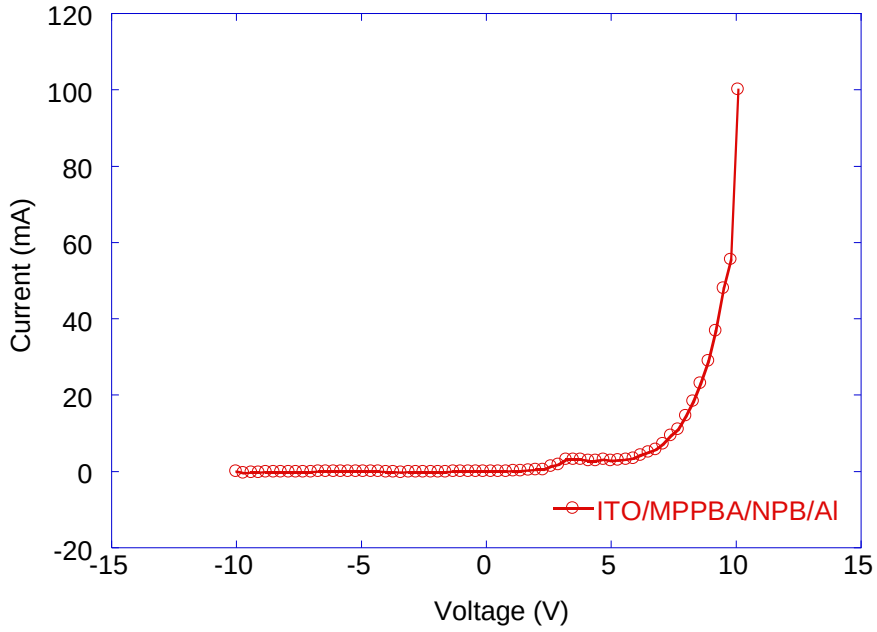

Figure 5.26. The Current-Voltage behavior ITO/MPPBA/NPB/Al between -10 and 10 V region.

The comparison of the logarithmic graphs of J/E^2 versus the square root of the applied electric field for ITO/NPB/Al and ITO/MPPBA/NPB/Al devices are shown in Figure 5.27. The effect of the SAM modification is noticeable.

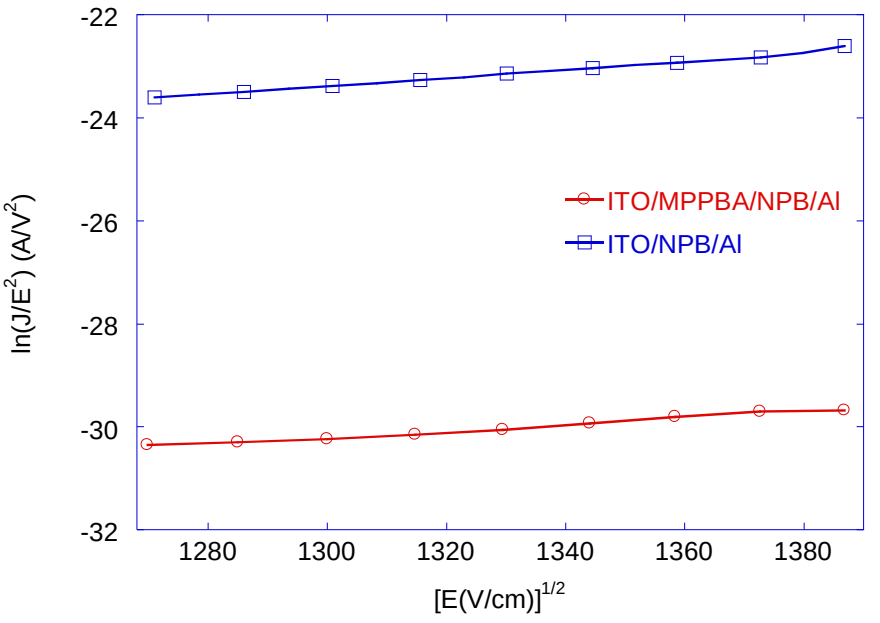

Figure 5.27. The logarithm of J/E^2 versus the square root of the applied electric field for ITO/NPB/Al and ITO/MPPBA/NPB/Al devices.

The calculated carrier mobility versus the square root of the applied electric field plots of ITO/NPB/Al and ITO/MPPBA/NPB/Al devices are shown in Figure 5.28.

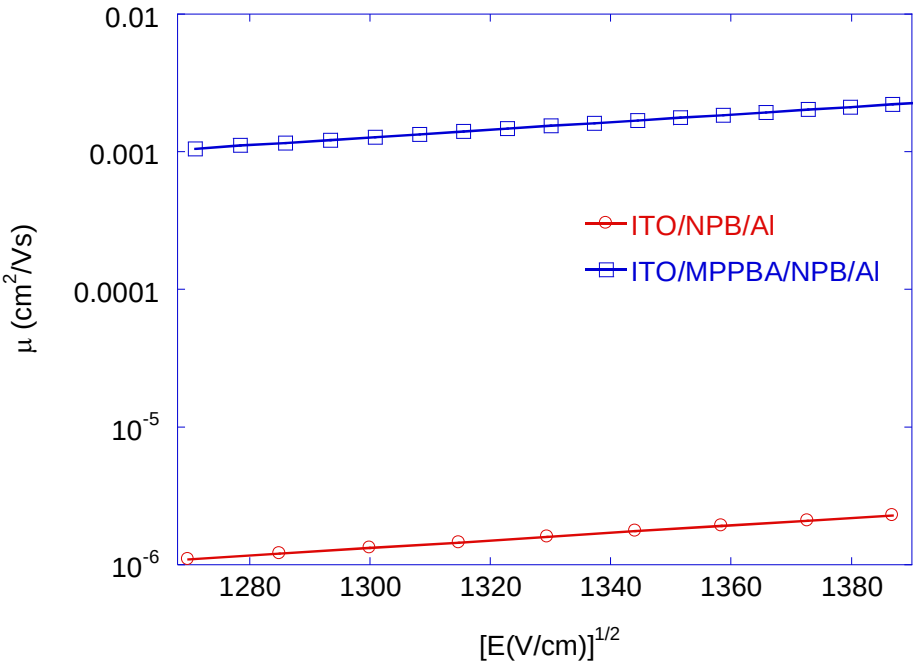

Figure 5.28. The carrier mobility of ITO/NPB/Al and ITO/MPPBA/NPB/Al devices.

The hole mobility of ITO/NPB/AL and ITO/MPPBA/NPB/Al devices were calculated as 2.21×10^{-6} and 2.22×10^{-3} cm^2/Vs at 1380 $(V/cm^2)^{1/2}$, respectively. The space charge limited current analysis shows that the charge mobility of NPB hole transport material on ITO increases with the use of carboxylic MPPBA self-assembled monolayer.

The current-voltage behavior of ITO/TPD/Al device at reverse and forward bias region is shown in Figure 5.29. At 10 V, current value of the device increases up to 0.18 mA.

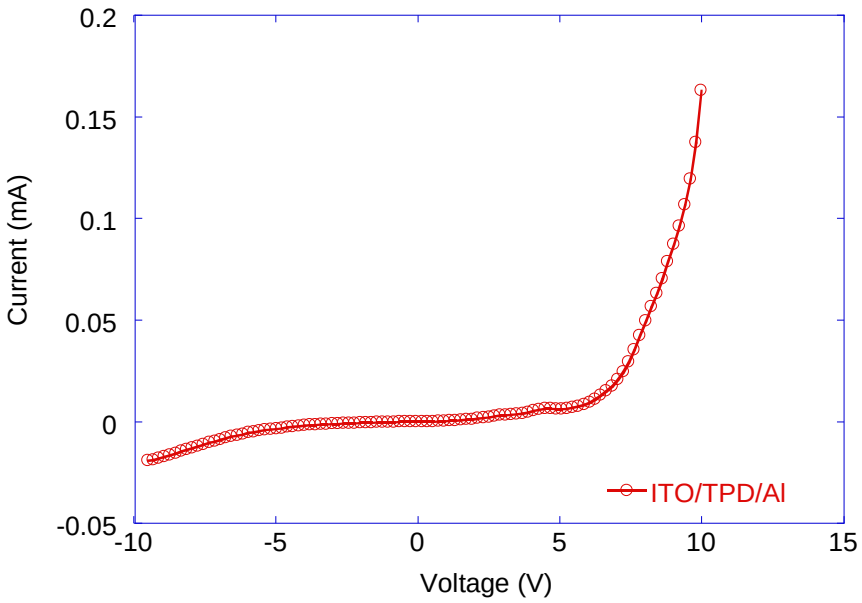

Figure 5.29. The Current-Voltage behavior ITO/TPD/Al between -10 and 10 V region.

In Figure 5.30. current-voltage characteristics of ITO/MPPBA/TPD/Al device is shown. At the forward bias region, current value of the SAM modified device reaches at 0.4 mA.

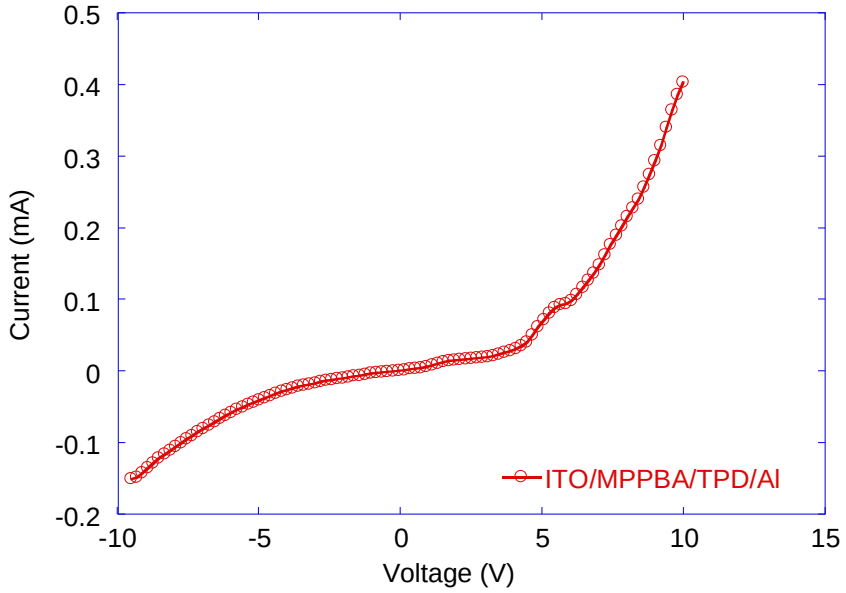

Figure 5.30. The Current-Voltage behavior ITO/MPPBA/TPD/Al between -10 and 10 V region.

The comparison of the logarithmic graphs of J/E^2 versus the square root of the applied electric field for ITO/TPD/Al and ITO/MPPBA/TPD/Al devices are shown in Figure 5.31. From the graph, it can be seen that MPPBA molecules modified the ITO surface and changed the surface characteristics.

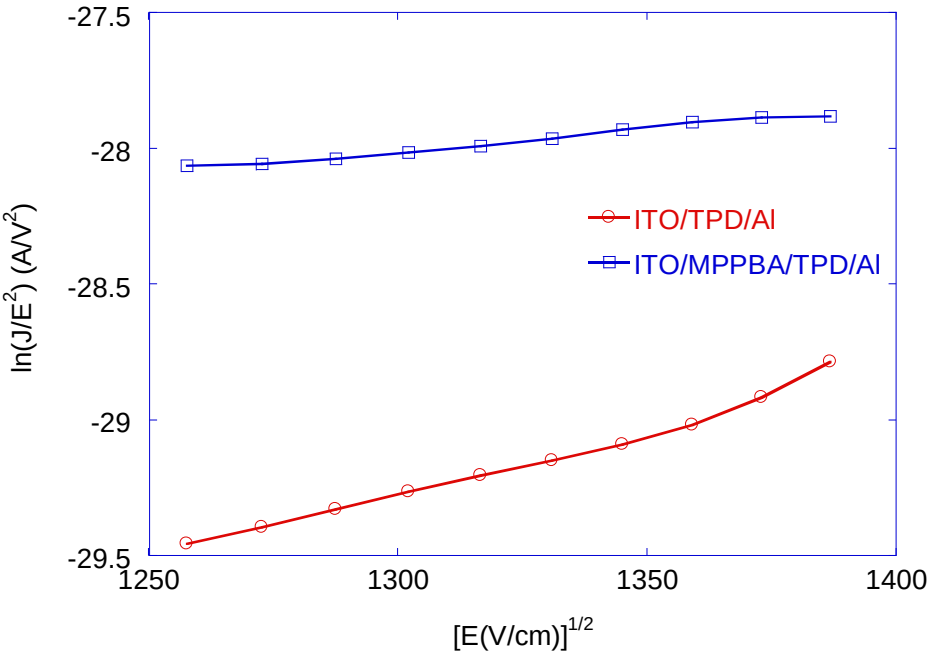

Figure 5.31. The logarithm of J/E^2 versus the square root of the applied electric field for ITO/TPD/Al and ITO/MPPBA/TPD/Al devices.

In Figure 5.32., the carrier mobility of ITO/TPD/Al and ITO/MPPBA/TPD/Al devices versus the square root of applied electric field is shown. Again for the devices made with TPD HTL material, SAM modification increases the hole mobility.

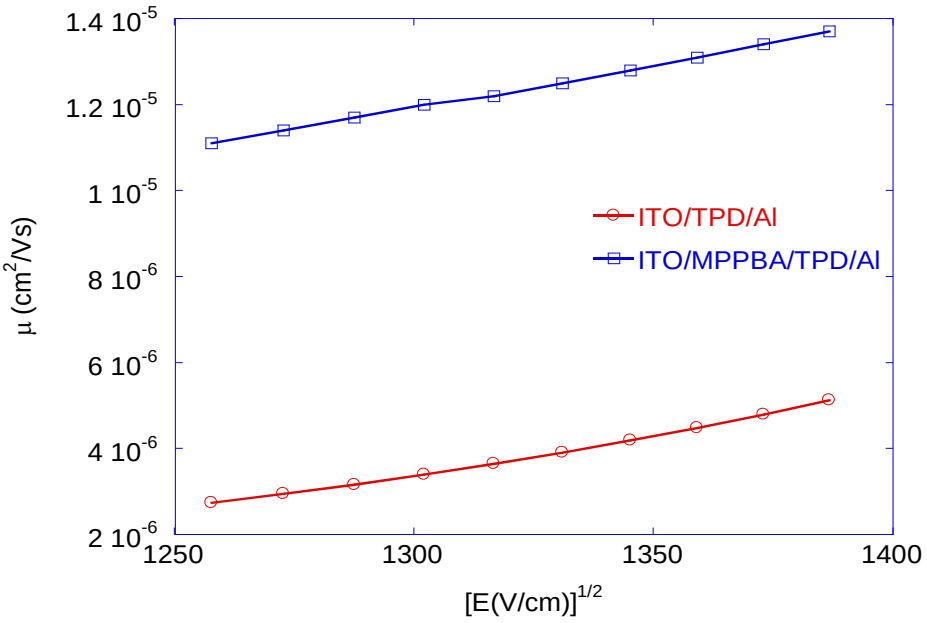

Figure 5.32. The carrier mobility of ITO/TPD/Al and ITO/MPPBA/TPD/Al devices.

The carrier mobility of ITO/TPD/Al and ITO/MPPBA/TPD/Al devices at 1380 (V/cm) $^{1/2}$ applied electric field measured as 4.94×10^{-6} and 1.35×10^{-5} cm^2/Vs, ı-V respectively. Thus, the surface modification of ITO surface with carboxylic acid based SAM increases the charge mobility.

5.2.2. Current-Voltage Characteristics of OLEDs with SAM Modified ITO

The current-voltage characteristics of ITO/TPD (50nm)/Alq_3 (60nm)/Al (120nm) and ITO/MPPBA/TPD (50nm)/Alq_3 (60nm)/Al (120nm) fabricated devices are shown in Figure 5.33. The turn-on voltage of the ITO/TPD/Alq_3/Al device was measured as 5. 5 V while the turn on voltage of the ITO/MPPBA/TPD/Alq_3/Al device was measured as 4.5 V. Therefore, MPPBA modified device's threshold voltage improved about 1 V compared to the one made with bare ITO film. The increase in the tunneling current density at the interface can be explained with inelastic tunneling mechanism over extra energy levels between HOMO and LUMO of aromatic MPPBA molecules with π-conjugated structure used as tunnel barrier at the interface.

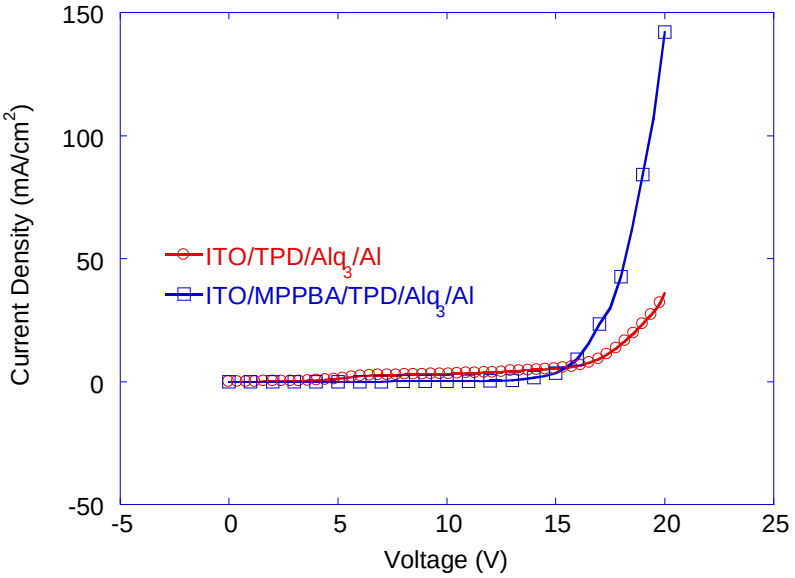

Figure 5.33. The Current density vs. voltage plot of devices fabricated with bare ITO and MPPBA modified ITO substrates using TPD as HTL.

The electroluminescence intensity spectrums of the ITO/TPD/Alq_3/Al and ITO/MPPBA/TPD/Alq_3/Al devices are shown in Figure 5.34. The maximum intensity was observed around 525 nm due to the Alq_3 emissive layer. Four times light intensity enhancement was obtained as a result of modification of ITO surface using MPPBA SAM molecule due to the increase in hole injection.

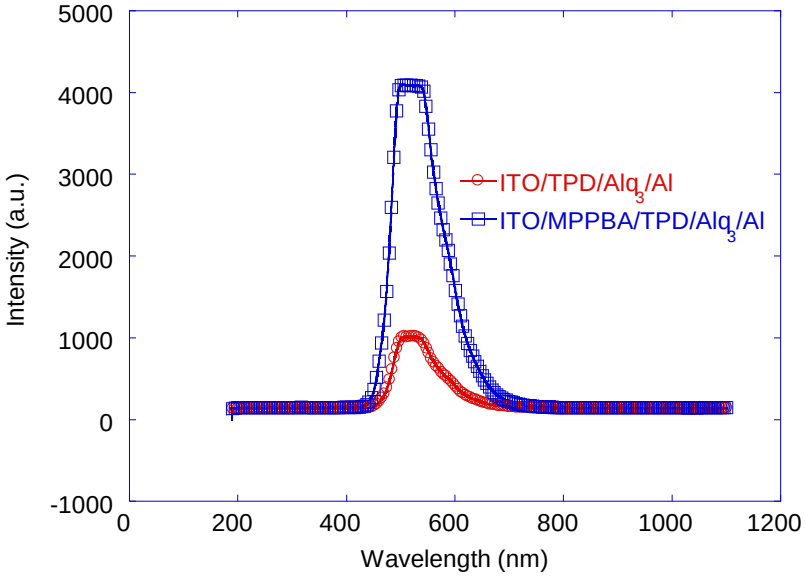

Figure 5.34. The EL intensity spectrum of devices with bare ITO and MPPBA modified ITO substrates using TPD as HTL.

The current-voltage behavior of ITO/NPB (50nm)/Alq_3 (60nm)/Al (120nm) and ITO/MPPBA/NPB (50nm)/Alq_3 (60nm)/Al (120nm) fabricated devices are shown in Figure 5.35. The turn-on voltage of the ITO/NPB/Alq_3/Al device was measured as 9.3 V while the turn on voltage of the ITO/MPPBA/NPB/Alq_3/Al device was measured as 7.3 V. Therefore, MPPBA modified device's threshold voltage improved about 2 V compared to the one made with bare ITO film.

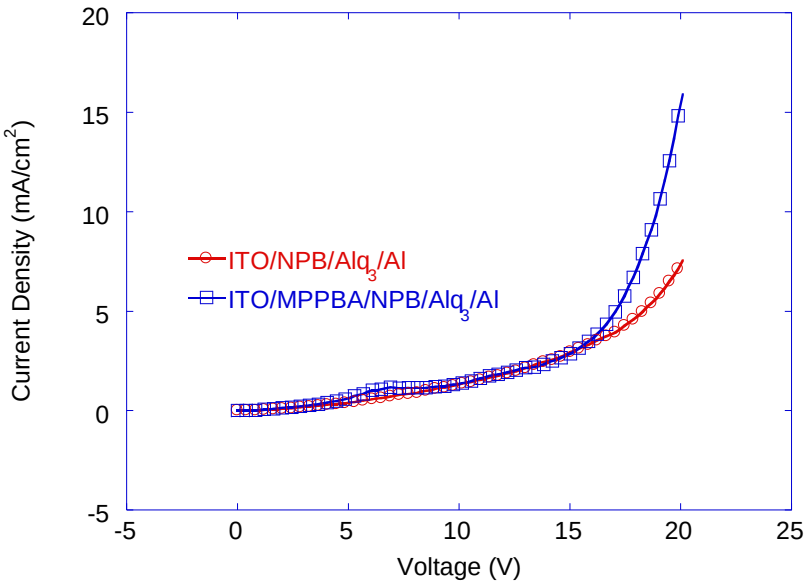

Figure 5.35. The Current density vs. voltage plot of devices fabricated with bare ITO and MPPBA modified ITO substrates using NPB as HTL.

The electroluminescence intensity spectrums of the ITO/NPB/Alq_3/Al and ITO/MPPBA/NPB/Alq_3/Al devices are shown in Figure 5.36. The maximum intensity is observed around 530 nm again due to the Alq_3 emissive layer. 2.5 times light intensity enhancement was obtained as a result of modification of ITO surface using MPPBA SAM molecule due to the increase in hole injection.

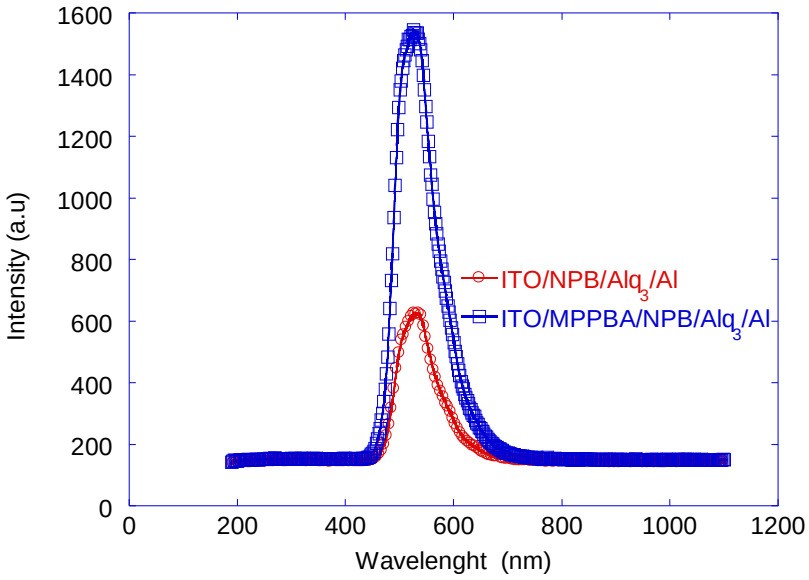

Figure 5.36. The EL intensity spectrum of devices with bare ITO and MPPBA modified ITO substrates using NPB as HTL.

CHAPTER 6

CONCLUSION

This thesis has focused on the enhancement of efficiency and turn-on voltage of OLEDs by modifying ITO surface with self-assembled monolayer molecules. In chapter one, a brief overview about OLED technology was given and the research objectives of the thesis have been discussed in details.

In chapter two, the advantages of OLEDs, history of the electroluminescence and OLED technology have been discussed. The organic semiconductors, basic OLED device structure, charge injection and recombination processes have been given in details. In addition, OLED efficiency and light outcoupling have been explained.

In chapter three, SAM phenomenon has been discussed briefly. This chapter consists of five subtitles; history of SAMs, types of SAMs, formation processes, characterization and finally SAM applications were presented. In characterization part, the basic operation theories of Quartz Crystal Microbalance (QCM), Atomic Force Microscopy (AFM), Kelvin Probe Force Microscopy (KPFM), X-ray Photoelectron Spectroscopy (XPS), Cyclic Voltammetry (CV) and Ultraviolet-visible Absorption Spectroscopy (UV-Vis) techniques have been explained.

Chapter four is the part where experimental details have been presented. In materials and chemical compounds part, the materials and the molecules that were used in fabrication of OLED devices were introduced. In the sample preparation part, substrate cleaning and preparation processes, SAM formation processes and deposition of the organic and metal materials have been explained step by step. In characterization part, technical properties of used systems and their apparatus have been given. The SAM formation process, used mask shapes and used instruments were illustrated.

In chapter five, the experimental results were given with a detailed discussion under two main subtitles with surface and electrical characterizations.

Surface characterization results obtained with QCM technique, the change in the frequency due to the SAM formation presented. The total mass change during the formation also calculated using Sauerbrey relation. In QCM experiments carried with

MPPBA solution in dynamic flow, the mass of the anchored SAM molecules on ITO coated QCM crystal was measured as 8 μgm/cm^2.

Topography and phase contrast images of fabricated thin films were performed using AFM. The results show that bare ITO has rougher surface with surface roughness of 3.71 nm. MPPBA molecules modify ITO surface leading to decrease up to 3.41 nm in roughness values. As HTL materials (NPB and TPD) have smooth surface, the rms value of the final thin films measured as 1.28 nm and 2.22 nm, respectively with the SAM modification of ITO surface. As a result, the interface matching between the anode and HTL has been provided.

Surface contact potential difference images of prepared thin films were obtained using KPFM. The surface potential difference was changed from 0.066 V to 0.286 V with MPPBA formation. Since contact surface potential proportional to the work function of that surface, the work function of the ITO surface increased with MPPBA modification, Fermi level of the ITO surface approaches to the HOMO level of the organic layer and thus the carrier injection improved with the decreasing threshold voltage.

The results obtained by X-ray photoelectron spectroscopy, Cyclic Voltammetry and UV-Vis Absorption spectroscopy ensures the existence of MPPBA molecules on the ITO surface after kept in SAM solution for 48 hours.

Electrical rectification characteristics of fabricated organic diodes were investigated to determine the Schottky barrier characteristics, current-voltage behavior of ITO/MPPBA/Al, ITO/TPD(NPB)/Al and ITO/MPPBA/TPD(NPB)/Al diodes analyzing between -1 V and +1 V. In addition, comparison of bare and MPPBA modified diodes prepared with n- and p-type silicon substrates and gold electrodes have been presented. The ideality factor and barrier height results obtained from Schottky characteristics indicate that barrier height difference between the anode and HTL was reduced by MPPBA modification of anode substrate. Space-charge-limited current (SCLC) analysis has been used to evaluate carrier mobility under steady state of current in an organic layer. The I-V measurements were carried out between (-10) V and (+10) V applied voltage. The hole mobility of ITO/NPB/AL and ITO/MPPBA/NPB/Al devices were calculated as 2.21×10^{-6} and 2.22×10^{-3} cm^2/Vs at 1380 (V/cm^2)$^{1/2}$, respectively. The carrier mobility of ITO/TPD/Al and ITO/MPPBA/TPD/Al devices at 1380 (V/cm) $^{1/2}$ applied electric field measured as 4.94×10^{-6} and 1.35×10^{-5} cm^2/Vs, I-V

respectively. Obtained carrier mobility values indicate that with the SAM modification, charge injection from anode to the organic layer improved and thus device efficiency increased.

OLED characteristics of fabricated ITO/TPD(NPB)/Alq_3/Al and ITO/MPPBA/ TPD(NPB)/Alq_3/Al organic light emitting diodes have been obtained. I-V results indicate that, the threshold voltage of the diodes with TPD HTL material decreased from 5.5 V to 4.5 V by modifying ITO surface with MPPBA molecules while the threshold voltage of the diodes with NPB HTL material decreased from 9.3 V to 7.3 V. Additionally, EL intensity results presented. SAM modified devices with TPD HTL material have four times higher intensity than devices prepared with bare ITO anode surface. In the devices with NPB HTL material 2.5 times light intensity enhancement was obtained as a result of modification of ITO surface using MPPBA SAM molecule due to the increase in hole injection.

To summarize, SAM was used to modify the ITO surface to match the work functions of anode and the organic layers at the interface. Important improvements have been achieved to increase the charge transport in OLED devices by using SAM techniques. SAM forming molecules with π –conjugated structure can be used at the interface to increase charge density due to extra energy levels between HOMO and LUMO of aromatic molecules as a result of inelastic tunneling mechanism.

REFERENCES

Abkowitz, M., I. Chen, and J.H. Sharp. 1968. Electron Spin Resonance of the Organic Semiconductor, Copper Phthalocyanine. *The Journal of Chemical Physics*. 48:4561.

Adachi, C., M.A. Baldo, M.E. Thompson, and S.R. Forrest. 2001. Nearly 100% internal phosphorescence efficiency in an organic light-emitting device. *Journal of Applied Physics*. 90:5048.

Agrawal, M., Y. Sun, S.R. Forrest, and P. Peumans. 2007. Enhanced outcoupling from organic light-emitting diodes using aperiodic dielectric mirrors. *Applied Physics Letters*. 90:241112.

Albrecht, T., and C. Quate. 1987. Atomic resolution imaging of a nonconductor by atomic force microscopy. *Journal of Applied Physics*. 62:2599-2602.

Allara, D.L., and R.G. Nuzzo. 1985. Spontaneously organized molecular assemblies. 1. Formation, dynamics, and physical properties of n-alkanoic acids adsorbed from solution on an oxidized aluminum surface. *Langmuir*. 1:45-52.

Almeleh, N., and S. Harrison. 1966. Trapping effects in the organic semiconductor triphenylene. *Journal of Physics and Chemistry of Solids*. 27:893-901.

An, Y., M. Chen, Q. Xue, and W. Liu. 2007. Preparation and self-assembly of carboxylic acid-functionalized silica. *Journal of colloid and interface science*. 311:507-513.

Asemblon. 2005. (accessed: www.asemblon.com).

Aviram, A., and M.A. Ratner. 1974. Molecular rectifiers. *Chemical physics letters*. 29:277-283.

Aziz, H., Z. Popovic, C.P. Tripp, N.-X. Hu, A.-M. Hor, and G. Xu. 1998. Degradation processes at the cathode/organic interface in organic light emitting devices with Mg:Ag cathodes. *Applied Physics Letters*. 72:2642-2644.

Balasubramanian, N., and A. Subrahmanyam. 1989. Electrical and optical properties of reactively evaporated indium tin oxide (ITO) films-dependence on substrate temperature and tin concentration. *Journal of Physics D: Applied Physics*. 22:206.

Baldo, M., D. O'Brien, M. Thompson, and S. Forrest. 1999. Excitonic singlet-triplet ratio in a semiconducting organic thin film. *Physical Review B*. 60:14422.

Baldo, M., D. O'brien, Y. You, A. Shoustikov, S. Sibley, M. Thompson, and S. Forrest. 1998. Highly efficient phosphorescent emission from organic electroluminescent devices. *Nature*. 395:151-154.

Beebe, J.M., V.B. Engelkes, J. Liu, J.J. Gooding, P.K. Eggers, Y. Jun, X. Zhu, M.N. Paddon-Row, and C.D. Frisbie. 2005. Length dependence of charge transport in nanoscopic molecular junctions incorporating a series of rigid thiol-terminated norbornylogs. *The Journal of Physical Chemistry B*. 109:5207-5215.

Beljonne, D., A. Ye, Z. Shuai, and J.L. Brédas. 2004. Chain Length Dependence of Singlet and Triplet Exciton Formation Rates in Organic Light Emitting Diodes. *Advanced Functional Materials*. 14:684-692.

Besbes, S., A. Ltaief, K. Reybier, L. Ponsonnet, N. Jaffrezic, J. Davenas, and H. Ben Ouada. 2003. Injection modifications by ITO functionalization with a self-assembled monolayer in OLEDs. *Synthetic Metals*. 138:197-200.

Bigelow, W., D. Pickett, and W. Zisman. 1946. Oleophobic monolayers* 1:: I. Films adsorbed from solution in non-polar liquids. *Journal of Colloid Science*. 1:513-538.

Binkauskiene, E., A. Lugauskas, M. Krunks, I.O. Acik, V. Jasulaitiene, and G. Saduikis. 2010. Interaction of Chrysosporium merdarium with titanium oxide surface. *Synthetic Metals*. 160:906-910.

Binning, G., C. Quate, and C. Gerber. 1986. Atomic force microscopy. *Phys. Rev. Lett*. 56:930-933.

Bishop, A.R., and R.G. Nuzzo. 1996. Self-assembled monolayers: Recent developments and applications. *Current Opinion in Colloid & Interface Science*. 1:127-136.

Blochwitz, J., T. Fritz, M. Pfeiffer, K. Leo, D. Alloway, P. Lee, and N. Armstrong. 2001. Interface electronic structure of organic semiconductors with controlled doping levels. *Organic Electronics*. 2:97-104.

Blom, P.W.M., M.J.M. Jong, and C.T.H.F. Liedenbaum. 1998. Device physics of polymer light-emitting diodes. *Polymers for Advanced Technologies*. 9:390-401.

Brandriss, S., and S. Margel. 1993. Synthesis and characterization of self-assembled hydrophobic monolayer coatings on silica colloids. *Langmuir*. 9:1232-1240.

Brown, T.M., R.H. Friend, I.S. Millard, D.J. Lacey, J.H. Burroughes, and F. Cacialli. 2001. Efficient electron injection in blue-emitting polymer light-emitting diodes with LiF/Ca/Al cathodes. *Applied Physics Letters*. 79:174-176.

Brown, T.M., J.S. Kim, R.H. Friend, F. Cacialli, R. Daik, and W.J. Feast. 1999. Built-in field electroabsorption spectroscopy of polymer light-emitting diodes incorporating a doped poly(3,4-ethylene dioxythiophene) hole injection layer. *Applied Physics Letters*. 75:1679-1681.

Brütting, W., H. Riel, T. Beierlein, and W. Riess. 2001. Influence of trapped and interfacial charges in organic multilayer light-emitting devices. *Journal of Applied Physics*. 89:1704.

Burroughes, J., D. Bradley, A. Brown, R. Marks, K. Mackay, R. Friend, P. Burns, and A. Holmes. 1990. Light-emitting diodes based on conjugated polymers. *Nature*. 347:539-541.

Burrows, P., G. Gu, S. Forrest, E. Vicenzi, and T. Zhou. 2000. Semitransparent cathodes for organic light emitting devices. *Journal of Applied Physics*. 87:3080.

Carrard, M., S. Goncalves-Conto, L. Si-Ahmed, D. Ades, and A. Siove. 1999. Improved stability of interfaces in organic light emitting diodes with high Tg materials and self-assembled monolayers. *Thin Solid Films*. 352:189-194.

Carson, G., and S. Granick. 1989. Self assembly of octadecyltrichlorosilane films on mica. *Journal of Applied Polymer Science*. 37:2767-2772.

Cavalleri, O., G. Gonella, S. Terreni, M. Vignolo, L. Floreano, A. Morgante, M. Canepa, and R. Rolandi. 2004. High resolution X-ray photoelectron spectroscopy of L-cysteine self-assembled films. *Phys. Chem. Chem. Phys.* 6:4042-4046.

Cerruti, M., C. Rhodes, M. Losego, A. Efremenko, J.P. Maria, D. Fischer, S. Franzen, and J. Genzer. 2007. Influence of indium-tin oxide surface structure on the ordering and coverage of carboxylic acid and thiol monolayers. *Journal of Physics D: Applied Physics*. 40:4212.

Chen, S., L. Li, C.L. Boozer, and S. Jiang. 2001. Controlled chemical and structural properties of mixed self-assembled monolayers by coadsorption of symmetric and asymmetric disulfides on Au (111). *The Journal of Physical Chemistry B*. 105:2975-2980.

Cheung, S., and N. Cheung. 1986. Extraction of Schottky diode parameters from forward current voltage characteristics. *Applied Physics Letters*. 49:85-87.

Chidsey, C.E.D., and D.N. Loiacono. 1990. Chemical functionality in self-assembled monolayers: structural and electrochemical properties. *Langmuir*. 6:682-691.

Chkoda, L., C. Heske, M. Sokolowski, E. Umbach, F. Steuber, and J. Staudigel. 2000. Work function of ITO substrates and band-offsets at the TPD/ITO interface determined by photoelectron spectroscopy. *Synthetic Metals*. 111:315-319.

Clark, D., and H. Thomas. 1976. Applications of ESCA to polymer chemistry. X. Core and valence energy levels of a series of polyacrylates. *Journal of Polymer Science: Polymer Chemistry Edition*. 14:1671-1700.

Crispin, X., V. Geskin, A. Crispin, J. Cornil, R. Lazzaroni, W.R. Salaneck, and J.L. Brédas. 2002. Characterization of the interface dipole at organic/metal interfaces. *Journal of the American Chemical Society*. 124:8131-8141.

Cui, X., A. Primak, X. Zarate, J. Tomfohr, O. Sankey, A. Moore, T. Moore, D. Gust, L. Nagahara, and S. Lindsay. 2002. Changes in the electronic properties of a

molecule when it is wired into a circuit. *The Journal of Physical Chemistry B*. 106:8609-8614.

Dobbertin, T., M. Kroeger, D. Heithecker, D. Schneider, D. Metzdorf, H. Neuner, E. Becker, H.H. Johannes, and W. Kowalsky. 2003. Inverted top-emitting organic light-emitting diodes using sputter-deposited anodes. *Applied Physics Letters*. 82:284.

Dubois, L.H., and R.G. Nuzzo. 1992. Synthesis, structure, and properties of model organic surfaces. *Annual Review of Physical Chemistry*. 43:437-463.

Engelkes, V.B., J.M. Beebe, and C.D. Frisbie. 2004. Length-dependent transport in molecular junctions based on SAMs of alkanethiols and alkanedithiols: Effect of metal work function and applied bias on tunneling efficiency and contact resistance. *Journal of the American Chemical Society*. 126:14287-14296.

Evans, S., S. Johnson, H. Ringsdorf, L. Williams, and H. Wolf. 1998. Photoswitching of azobenzene derivatives formed on planar and colloidal gold surfaces. *Langmuir*. 14:6436-6440.

Fan, J.C.C., and J.B. Goodenough. 1977. X-ray photoemission spectroscopy studies of Sn-doped indium-oxide films. *Journal of Applied Physics*. 48:3524-3531.

Feng, X. 2008. Development of 8-Hydroxyquinoline Metal Based Organic Light-Emitting Diodes. *In* Department of Materials Science and Engineering. Vol. Doctor of Philosophy. University of Toronto.

Finklea, H. 1996. Electroanalytical Chemistry. *by AJ Bard and I. Rubinstein, Marcel Dekker, New York*. 19:109.

Finklea, H. 2000. In Encyclopedia of Analytical Chemistry: Applications, Theory and Instrumentation. John Wiley & Sons, New York.

Finklea, H., L. Robinson, A. Blackburn, B. Richter, D. Allara, and T. Bright. 1986. Formation of an organized monolayer by solution adsorption of octadecyltrichlorosilane on gold: Electrochemical properties and structural characterization. *Langmuir*. 2:239-244.

Ganzorig, C., K.J. Kwak, K. Yagi, and M. Fujihira. 2001. Fine tuning work function of indium tin oxide by surface molecular design: Enhanced hole injection in organic electroluminescent devices. *Applied Physics Letters*. 79:272.

Gelbart, W.M., and S.A. Rice. 1969. Some Formal Results in a Theory of Molecular Rearrangements: Photoisomerism. *The Journal of Chemical Physics*. 50:4775-4786.

Giebeler, C., H. Antoniadis, D.D.C. Bradley, and Y. Shirota. 1999. Influence of the hole transport layer on the performance of organic light-emitting diodes. *Journal of Applied Physics*. 85:608.

Goodman, F.O., and N. Garcia. 1991. Roles of the attractive and repulsive forces in atomic-force microscopy. *Physical Review B*. 43:4728.

Griffiths, D.J. 2005. Introduction to quantum mechanics. Pearson Prentice Hall.

Gu, G., D. Garbuzov, P. Burrows, S. Venkatesh, S. Forrest, and M. Thompson. 1997. High-external-quantum-efficiency organic light-emitting devices. *Optics letters*. 22:396-398.

Gun, J., R. Iscovici, and J. Sagiv. 1984. On the formation and structure of self-assembling monolayers:: II. A comparative study of Langmuir--Blodgett and adsorbed films using ellipsometry and IR reflection--absorption spectroscopy. *Journal of colloid and interface science*. 101:201-213.

Gun, J., and J. Sagiv. 1986. On the formation and structure of self-assembling monolayers:: III. Time of formation, solvent retention, and release. *Journal of colloid and interface science*. 112:457-472.

Hacker, C.A., J.D. Batteas, J.C. Garno, M. Marquez, C.A. Richter, L.J. Richter, R.D. van Zee, and C.D. Zangmeister. 2004. Structural and chemical characterization of monofluoro-substituted oligo (phenylene-ethynylene) thiolate self-assembled monolayers on gold. *Langmuir*. 20:6195-6205.

Haddock, N., B. Domercq, and B. Kippelen. 2005. High mobility C< sub> 60</sub> organic field-effect transistors. *Electronics Letters*. 41:444-446.

Haitjema, H., and J. Elich. 1991. Physical properties of pyrolytically sprayed tin-doped indium oxide coatings. *Thin Solid Films*. 205:93-100.

Haldi, A. 2008. Patternable electrophosphorescent organic light-emitting diodes with solution-processed organic layers. Georgia Institute of Technology.

Hartmann, U. 1991. van der Waals interactions between sharp probes and flat sample surfaces. *Physical Review B*. 43:2404.

Hatton, R.A., S.R. Day, M.A. Chesters, and M.R. Willis. 2001. Organic electroluminescent devices: enhanced carrier injection using an organosilane self assembled monolayer (SAM) derivatized ITO electrode. *Thin Solid Films*. 394:291-296.

He, G., M. Pfeiffer, K. Leo, M. Hofmann, J. Birnstock, R. Pudzich, and J. Salbeck. 2004. High-efficiency and low-voltage p i n electrophosphorescent organic light-emitting diodes with double-emission layers. *Applied Physics Letters*. 85:3911.

He, P., S.D. Wang, W.K. Wong, C.S. Lee, and S.T. Lee. 2001. Vibrational and photoemission study of the interface between phenyl diamine and indium tin oxide. *Applied Physics Letters*. 79:1561-1563.

Higuch, M., S. Uekusa, R. Nakano, and K. Yokogawa. 1994. Postdeposition annealing influence on sputtered indium tin oxide film characteristics. *Jpn. J. Appi. Phys. Vol*. 33:302-306.

Ho, P.K.H., M. Granström, R.H. Friend, and N.C. Greenham. 1998. Ultrathin Self Assembled Layers at the ITO Interface to Control Charge Injection and Electroluminescence Efficiency in Polymer Light Emitting Diodes. *Advanced Materials*. 10:769-774.

Hosokawa, C., H. Higashi, H. Nakamura, and T. Kusumoto. 1995. Highly efficient blue electroluminescence from a distyrylarylene emitting layer with a new dopant. *Applied Physics Letters*. 67:3853-3855.

Huang, Q., S. Reineke, K. Walzer, M. Pfeiffer, and K. Leo. 2006. Quantum efficiency enhancement in top-emitting organic light-emitting diodes as a result of enhanced intrinsic quantum yield. *Applied Physics Letters*. 89:263512.

Ishii, H., H. Oji, E. Ito, N. Hayashi, D. Yoshimura, and K. Seki. 2000. Energy level alignment and band bending at model interfaces of organic electroluminescent devices. *Journal of Luminescence*. 87-89:61-65.

Ishii, H., K. Sugiyama, E. Ito, and K. Seki. 1999. Energy level alignment and interfacial electronic structures at organic/metal and organic/organic interfaces. *Advanced Materials*. 11:605-625.

Jabbour, G., B. Kippelen, N. Armstrong, and N. Peyghambarian. 1998. Aluminum based cathode structure for enhanced electron injection in electroluminescent organic devices. *Applied Physics Letters*. 73:1185.

Kaifer, A.E., and M. Gómez-Kaifer. 1999. Supramolecular electrochemistry. Wiley Online Library.

Kane, V., and P. Mulvaney. 1998. Double-layer interactions between self-assembled monolayers of -mercaptoundecanoic acid on gold surfaces. *Langmuir*. 14:3303-3311.

Kelley, T.W., P.F. Baude, C. Gerlach, D.E. Ender, D. Muyres, M.A. Haase, D.E. Vogel, and S.D. Theiss. 2004. Recent progress in organic electronics: Materials, devices, and processes. *Chem. Mater*. 16:4413-4422.

Kera, S., Y. Yabuuchi, H. Yamane, H. Setoyama, K. Okudaira, A. Kahn, and N. Ueno. 2004. Impact of an interface dipole layer on molecular level alignment at an organic-conductor interface studied by ultraviolet photoemission spectroscopy. *Physical Review B*. 70:085304.

Kim, J.S., P.K.H. Ho, N.C. Greenham, and R.H. Friend. 2000. Electroluminescence emission pattern of organic light-emitting diodes: Implications for device efficiency calculations. *Journal of Applied Physics*. 88:1073.

Krummacher, B., M. Mathai, V. Choong, S. Choulis, F. So, and A. Winnacker. 2006. General method to evaluate substrate surface modification techniques for light extraction enhancement of organic light emitting diodes. *Journal of Applied Physics*. 100:054702.

Langevin, P. 1903. The ionisation of gases. *Annales de Chimie et de Physique* 28:289-384.

Lee, J., B.J. Jung, J.I. Lee, H.Y. Chu, L.M. Do, and H.K. Shim. 2002. Modification of an ITO anode with a hole-transporting SAM for improved OLED device characteristics. *Journal of Materials Chemistry*. 12:3494-3498.

Li, D.Q., B.I. Swanson, J.M. Robinson, and M.A. Hoffbauer. 1993. Porphyrin based self-assembled monolayer thin films: synthesis and characterization. *Journal of the American Chemical Society*. 115:6975-6980.

Li, F., H. Tang, J. Anderegg, and J. Shinar. 1997a. Fabrication and electroluminescence of double-layered organic light-emitting diodes with the AlO/Al cathode. *Applied Physics Letters*. 70:1233.

Li, F., H. Tang, J. Shinar, O. Resto, and S.Z. Weisz. 1997b. Effects of aquaregia treatment of indium--tin--oxide substrates on the behavior of double layered organic light-emitting diodes. *Applied Physics Letters*. 70:2741-2743.

Madigan, C., M.H. Lu, and J. Sturm. 2000. Improvement of output coupling efficiency of organic light-emitting diodes by backside substrate modification. *Applied Physics Letters*. 76:1650-1652.

Mäkinen, A., I. Hill, R. Shashidhar, N. Nikolov, and Z. Kafafi. 2001. Hole injection barriers at polymer anode/small molecule interfaces. *Applied Physics Letters*. 79:557.

Mark, F. 2001. Optical properties of solids. Oxford, Oxford University Press, New York.

Marti, O., B. Drake, and P. Hansma. 1987. Atomic force microscopy of liquid covered surfaces: Atomic resolution images. *Applied Physics Letters*. 51:484-486.

Mathauer, K., and C.W. Frank. 1993. Binary self-assembled monolayers as prepared by successive adsorption of alkyltrichlorosilanes. *Langmuir*. 9:3446-3451.

McGinnes, J., P. Corry, and P. Proctor. 1974. Amorphous-semiconductor switching in melanins. *Science*. 183:853-855.

Meulenkamp, E.A., R. van Aar, J.J.A.M. Bastiaansen, A. van den Biggelaar, H. Börner, K. Brunner, M. BÜCHEL, A. van Dijken, N.M.M. Kiggen, and M. Kilitziraki. 2004. High efficiency polymer LEDs: triplets and novel devices. Society of Photo-Optical Instrumentation Engineers. 90-103.

Meyer, G., and N.M. Amer. 1988. Novel optical approach to atomic force microscopy. *Applied Physics Letters*. 53:1045-1047.

Milliron, D., I. Hill, C. Shen, A. Kahn, and J. Schwartz. 2000. Surface oxidation activates indium tin oxide for hole injection. *Journal of Applied Physics*. 87:572.

Montagne, F., J. Polesel-Maris, R. Pugin, and H. Heinzelmann. 2008. Poly (N-isopropylacrylamide) Thin Films Densely Grafted onto Gold Surface: Preparation, Characterization, and Dynamic AFM Study of Temperature-Induced Chain Conformational Changes. *Langmuir*. 25:983-991.

Mott, N.F., and R.W. Gurney. 1940. Electronic Processes in Ionic Crystal. *Clarendon PressOxford*.

Moussaif, N., C. Pagnoulle, J. Riga, and R. Jérôme. 2000. XPS analysis of the PC/PVDF interface modified by PMMA. Location of the PMMA at the interface. *Polymer*. 41:3391-3394.

Mu, H. 2011. Carriers injection and transport in small molecule organic light emitting diodes (OLED). Vol. Ph.D. University of Cincinnati, United States -- Ohio.

Nelson, S., Y.Y. Lin, D. Gundlach, and T. Jackson. 1998. Temperature-independent transport in high-mobility pentacene transistors. *Applied Physics Letters*. 72:1854.

Nonnenmacher, M., M. Oboyle, and H. Wickramasinghe. 1991. Kelvin probe force microscopy. *Applied Physics Letters*. 58:2921-2923.

Nüesch, F., E. Forsythe, Q. Le, Y. Gao, and L. Rothberg. 2000. Importance of indium tin oxide surface acido basicity for charge injection into organic materials based light emitting diodes. *Journal of Applied Physics*. 87:7973.

Ogawa, H., T. Chihara, and K. Taya. 1985. Selective monomethyl esterification of dicarboxylic acids by use of monocarboxylate chemisorption on alumina. *Journal of the American Chemical Society*. 107:1365-1369.

Osikowicz, W., X. Crispin, C. Tengstedt, L. Lindell, T. Kugler, and W.R. Salaneck. 2004. Transparent low-work-function indium tin oxide electrode obtained by molecular scale interface engineering. *Applied Physics Letters*. 85:1616.

Oxtoby, D.W., W.A. Freeman, and T.F. Block. 2003. Chemistry: Science of Change.

Peisert, H., M. Knupfer, F. Zhang, A. Petr, L. Dunsch, and J. Fink. 2004. The interface between phthalocyanines and PEDOT: PSS: evidence for charge transfer and doping. *Surface science*. 566:554-559.

Piromreun, P., H. Oh, Y. Shen, G.G. Malliaras, J.C. Scott, and P.J. Brock. 2000. Role of CsF on electron injection into a conjugated polymer. *Applied Physics Letters*. 77:2403-2405.

Pope, M., H.P. Kallmann, and P. Magnante. 1963. Electroluminescence in Organic Crystals. *Journal of Chemical Physics*. 38:2042-2043.

Pope, M., and C.E. Swenberg. 1999. Electronic processes in organic crystals and polymers. Oxford University Press Oxford.

Rhoderick, E.H., and R. Williams. 1988. Metal-semiconductor contacts. Clarendon Press Oxford.

Riel, H., S. Karg, T. Beierlein, B. Ruhstaller, and W. Rieß. 2003. Phosphorescent top-emitting organic light-emitting devices with improved light outcoupling. *Applied Physics Letters*. 82:466.

Sabatani, E., I. Rubinstein, R. Maoz, and J. Sagiv. 1987. Organized self-assembling monolayers on electrodes. I: Octadecyl derivatives on gold. *Journal of electroanalytical chemistry and interfacial electrochemistry*. 219:365-371.

Sagiv, J. 1980. Organized monolayers by adsorption. 1. Formation and structure of oleophobic mixed monolayers on solid surfaces. *Journal of the American Chemical Society*. 102:92-98.

Salaneck, W.R., and J.L. Brédas. 1996. The metal on polymer interface in polymer light emitting diodes. *Advanced Materials*. 8:48-52.

Sauerbrey, G. 1959. Use of quartz vibrator for weighing thin films on a microbalance. *Z. Phys*. 155:206-210.

Schlotter, N., M.D. Porter, T. Bright, and D.L. Allara. 1986. Formation and structure of a spontaneously adsorbed monolayer of arachidic on silver. *Chemical physics letters*. 132:93-98.

Schwartz, D., S. Steinberg, J. Israelachvili, and J. Zasadzinski. 1992. Growth of a self-assembled monolayer by fractal aggregation. *Physical review letters*. 69:3354-3357.

Scott, J.C. 2003. Metal-organic interface and charge injection in organic electronic devices. *Journal of Vacuum Science & Technology A: Vacuum, Surfaces, and Films*. 21:521.

Scott, J.C., P.J. Brock, J.R. Salem, S. Ramos, G.G. Malliaras, S.A. Carter, and L. Bozano. 2000. Charge transport processes in organic light-emitting devices. *Synthetic Metals*. 111:289-293.

Shinar, J. 2004. Organic light-emitting devices: a survey. *Springer Verlag*.

Shipway, A., M. Lahav, and I. Willner. 2000. Nanostructured gold colloid electrodes. *Advanced Materials*. 12:993-998.

Shirakawa, H., E.J. Louis, A.G. MacDiarmid, C.K. Chiang, and A.J. Heeger. 1977. Synthesis of electrically conducting organic polymers: halogen derivatives of

polyacetylene,(CH) x. *Journal of the Chemical Society, Chemical Communications*. 1977:578-580.

Singh, A. 2009. Electrical and Optical properties of electroluminescent materials used for Organic Light Emitting Device. *In* Materials Science and Engineering. Vol. Master of Technology. School of Physics and Material Science Thapar University, India.

Smith, L., J. Wasey, and W.L. Barnes. 2004. Light outcoupling efficiency of top-emitting organic light-emitting diodes. *Applied Physics Letters*. 84:2986-2988.

Snook, G.A. 2000. Investigation of Solid-State Reactions by Electrochemical and Quartz Crystal

Microbalance Measurements. *In* Department of Chemistry. Vol. B.Sc. Monash University, Melbourne.

Sreenivas, K., T.S. Rao, A. Mansingh, and S. Chandra. 1985. Preparation and characterization of rf sputtered indium tin oxide films. *Journal of Applied Physics*. 57:384-392.

Subramanian, V., E. Wolf, and P.V. Kamat. 2001. Semiconductor-metal composite nanostructures. To what extent do metal nanoparticles improve the photocatalytic activity of TiO2 films? *The Journal of Physical Chemistry B*. 105:11439-11446.

Sugiyama, K., H. Ishii, Y. Ouchi, and K. Seki. 2000. Dependence of indium-tin-oxide work function on surface cleaning method as studied by ultraviolet and x-ray photoemission spectroscopies. *Journal of Applied Physics*. 87:295.

Sun, X., L. Cheng, M. Liu, L. Liao, N. Wong, C. Lee, and S. Lee. 2003. Photoelectron spectroscopic study of iodine-and bromine-treated indium tin oxides and their interfaces with organic films. *Chemical physics letters*. 370:425-430.

Suzuki, H. 1996. Fabrication of electron injecting Mg:Ag alloy electrodes for organic light-emitting diodes with radio frequency magnetron sputter deposition. *Applied Physics Letters*. 69:1611-1613.

Swenberg, C., and M. Pope. 1999. Electronic Processes of Organic Crystals and Polymers. Oxford University Press, Oxford.

Szczyrbowski, J., A. Dietrich, and H. Hoffmann. 1983. Optical and electrical properties of RF sputtered indium-tin oxide films. *physica status solidi (a)*. 78:243-252.

Sze, S. 1981. Physics of semiconductor devices. 1981. Wiley, New York.

Tang, C.W., and S.A.V. Slyke. 1987. Organic electroluminescent diodes. *Applied Physics Letters*. 51:913.

Thiruvengadam, S. 2002. Characterization and Analysis of Hybrid Electronic Materials For Molecular Based Devices *In* The Department of Electrical and Computer Engineering. Louisiana State University, India.

Tillman, N., A. Ulman, J.S. Schildkraut, and T.L. Penner. 1988. Incorporation of phenoxy groups in self-assembled monolayers of trichlorosilane derivatives. Effects on film thickness, wettability, and molecular orientation. *Journal of the American Chemical Society*. 110:6136-6144.

Tlili, A., A. Abdelghani, S. Hleli, and M.A. Maaref. 2004. Electrical characterization of a thiol SAM on gold as a first step for the fabrication of an immunosensors based on a quartz crystal microbalance. *Sensors*. 4:105-114.

Tsutsui, T., M. Yahiro, H. Yokogawa, K. Kawano, and M. Yokoyama. 2001. Doubling Coupling Out Efficiency in Organic Light Emitting Devices Using a Thin Silica Aerogel Layer. *Advanced Materials*. 13:1149-1152.

Turak, A., D. Grozea, X.D. Feng, Z.H. Lu, H. Aziz, and A.M. Hor. 2002. Metal/AlQ[sub 3] interface structures. *Applied Physics Letters*. 81:766-768.

Ulman, A. 1996. Formation and structure of self-assembled monolayers. *Chemical reviews*. 96:1533-1554.

Ulman, A., S.D. Evans, Y. Shnidman, R. Sharma, J.E. Eilers, and J.C. Chang. 1991. Concentration-driven surface transition in the wetting of mixed alkanethiol monolayers on gold. *Journal of the American Chemical Society*. 113:1499-1506.

Vincett, P., W. Barlow, R. Hann, and G. Roberts. 1982. Electrical conduction and low voltage blue electroluminescence in vacuum-deposited organic films. *Thin Solid Films*. 94:171-183.

Wang, P.W., Y.J. Liu, C. Devadoss, P. Bharathi, and J.S. Moore. 1996. Electroluminescent diodes from a single component emitting layer of dendritic macromolecules. *Advanced Materials*. 8:237-241.

Wasserman, S.R., Y.T. Tao, and G.M. Whitesides. 1989. Structure and reactivity of alkylsiloxane monolayers formed by reaction of alkyltrichlorosilanes on silicon substrates. *Langmuir*. 5:1074-1087.

Weisenhorn, A.L., M. Egger, F. Ohnesorge, S. Gould, S. Heyn, H. Hansma, R. Sinsheimer, H. Gaub, and P. Hansma. 1991. Molecular-resolution images of Langmuir-Blodgett films and DNA by atomic force microscopy. *Langmuir*. 7:8-12.

White, H.S., J.D. Peterson, Q. Cui, and K.J. Stevenson. 1998. Voltammetric measurement of interfacial acid/base reactions. *The Journal of Physical Chemistry B*. 102:2930-2934.

Wold, D.J., and C.D. Frisbie. 2001. Fabrication and characterization of metal-molecule-metal junctions by conducting probe atomic force microscopy. *Journal of the American Chemical Society*. 123:5549-5556.

Wu, C., C. Wu, J. Sturm, and A. Kahn. 1997. Surface modification of indium tin oxide by plasma treatment: An effective method to improve the efficiency, brightness, and reliability of organic light emitting devices. *Applied Physics Letters*. 70:1348.

Yan, C., M. Zharnikov, A. Gölzhäuser, and M. Grunze. 2000. Preparation and characterization of self-assembled monolayers on indium tin oxide. *Langmuir*. 16:6208-6215.

Zeng, D., K. Yung, and C. Xie. 2002. XPS investigation of the chemical characteristics of Kapton films ablated by a pulsed TEA CO2 laser. *Surface and Coatings Technology*. 153:210-216.

Zou, L., V. Savvate'ev, J. Booher, C.H. Kim, and J. Shinar. 2001. Combinatorial fabrication and studies of intense efficient ultraviolet--violet organic light-emitting device arrays. *Applied Physics Letters*. 79:2282-2284.